2016

Model-based Optimization and Feedback Control of the Current Density Profile Evolution in NSTX-U

Zeki Okan Ilhan
Lehigh University

Model-based Optimization and Feedback Control of the Current Density Profile Evolution in NSTX-U

by

Zeki Okan Ilhan

Presented to the Graduate and Research Committee

of Lehigh University

in Candidacy for the Degree of

Doctor of Philosophy

in

Mechanical Engineering

Lehigh University

September, 2016

Certificate of Approval

This thesis is accepted and approved in partial fulfillment of the requirements for the Doctor of Philosophy in Mechanical Engineering.

_____

Date

_____

Professor Eugenio Schuster

Dissertation Advisor

_____

Accepted Date

Committee Members:

_____

Professor Donald O. Rockwell

_____

Professor Nader Motee

_____

Professor Arnold H. Kritz

"Dedicated to a Happier Year..."

Acknowledgements

I have worked with several colleagues, researchers and professors throughout my graduate education at Lehigh. I hereby would like to extend my acknowledgements for their invaluable contributions. Without their help, it would have been impossible for me to complete this dissertation.

First of all, I would like to extend my sincere gratitude to my advisor, Professor Eugenio Schuster, for his continuous support and patience in guiding me to conduct research in this interdisciplinary field at the boundary of controls and nuclear fusion, and for providing me opportunities to present my findings in numerous conferences and research meetings. It has been through his sincere advice and encouragement that I have been able to survive this highly complicated and emotionally difficult period of my life.

I would like to thank the scientists Dr. David A. Gates, Dr. Jonathan E. Menard, Dr. Stefan P. Gerhardt, and Dr. Egemen Kolemen from the Princeton Plasma Physics Laboratory (PPPL), for their collaboration and support. I deeply appreciate them for sharing their expertise, advice and comments about the NSTX-U control research over the years.

I would like to specifically thank Dr. Mark D. Boyer, a former member of the Plasma Control Laboratory at Lehigh, and currently a post-doctoral researcher at PPPL, for providing me his technical support during my research experience at PPPL over the summer of 2015.

I would like to thank my dissertation committee members at Lehigh University, Professor Donald O. Rockwell, Professor Nader Motee, and Professor Arnold H. Kritz, for arranging time for the committee meetings and for sharing their ideas and expertise during the preparation of my dissertation. I would like to also thank Dr. Tariq Rafiq, a Principal Scientist in the Physics Department at Lehigh University, for his technical help and guidance in the preparation of this dissertation.

Last but not least, I would like to extend my sincere thanks to the former and current members of the Plasma Control Laboratory at Lehigh University, Dr. Wenyu Shi, Dr. Mark D. Boyer, Dr. Justin E. Barton, Dr. Menno Lauret, William P. Wehner, Hexiang Wang, and Andres P. Martinez, for their friendship and technical support over the years.

Contents

List of Tables

List of Figures

Abstract

Unlike nuclear fission in present nuclear power plants, where energy is generated by splitting heavy atoms like uranium, nuclear fusion generates energy by fusing light nuclei like hydrogen isotopes under high-temperature and high-pressure conditions, at which the reactants (hydrogen isotopes) separate from their electrons and form an ionized gas called plasma, which is considered as the fourth state of matter. Contrary to fission, fusion provides more energy density, poses almost no risk of a catastrophic nuclear accident, and produces mostly short-term, low-level radioactive waste.

The main difficulty in maintaining fusion reactions is the development of a device that can confine the hot plasma for sufficiently long time while preventing it from hitting the walls of the confining device. Among several techniques, magnetic confinement appears as the most promising approach. In particular, the tokamak device is a toroidal device surrounded by large magnetic coils responsible for the magnetic fields that confine the plasma. A spherical tokamak, or a spherical torus (ST), is a variation of the conventional tokamak concept. Compared to a standard tokamak, the ST device extrapolates to a more compact, potentially lower-cost reactor with higher efficiency of confinement.

Nuclear fusion research is a highly challenging, multidisciplinary field seeking contributions from both plasma physics and multiple engineering areas. As an application

of plasma control engineering, this dissertation mainly explores methods to control the current density profile evolution within the National Spherical Torus eXperiment-Upgrade (NSTX-U), which is a substantial upgrade based on the NSTX device, which is located in Princeton Plasma Physics Laboratory (PPPL), Princeton, NJ.

Active control of the toroidal current density profile is among those plasma control milestones that the NSTX-U program must achieve to realize its next-step operational goals, which are characterized by high-performance, long-pulse, MHD-stable plasma operation with neutral beam heating. Therefore, the aim of this work is to develop model-based, feedforward and feedback controllers that can enable time regulation of the current density profile in NSTX-U by actuating the total plasma current, electron density, and the powers of the individual neutral beam injectors.

Motivated by the coupled, nonlinear, multivariable, distributed-parameter plasma dynamics, the first step towards control design is the development of a physics-based, control-oriented model for the current profile evolution in NSTX-U in response to non-inductive current drives and heating systems. Numerical simulations of the proposed control-oriented model show qualitative agreement with the high-fidelity physics code TRANSP.

The next step is to utilize the proposed control-oriented model to design an open-loop actuator trajectory optimizer. Given a desired operating state, the optimizer produces the actuator trajectories that can steer the plasma to such state. The objective of the feedforward control design is to provide a more systematic approach to advanced scenario planning in NSTX-U since the development of such scenarios is conventionally carried out experimentally by modifying the tokamaks actuator trajectories and analyzing the resulting plasma evolution.

Finally, the proposed control-oriented model is embedded in feedback control schemes based on optimal control and Model Predictive Control (MPC) approaches.

Integrators are added to the standard Linear Quadratic Gaussian (LQG) and MPC formulations to provide robustness against various modeling uncertainties and external disturbances. The effectiveness of the proposed feedback controllers in regulating the current density profile in NSTX-U is demonstrated in closed-loop nonlinear simulations. Moreover, the optimal feedback control algorithm has been implemented successfully in closed-loop control simulations within TRANSP through the recently developed Expert routine.

Chapter 1

Introduction

1.1 Motivation for Nuclear Fusion

The energy demand is continuously rising as a fast industrial development takes place in many emerging countries [11]. As shown in Fig. 1.1, the majority of the energy used on Earth nowadays is extracted from fossil fuels such as coal, oil, and natural gas. Besides being limited resources, the use of fossil fuels for energy generation is the main source of carbon dioxide emission, which gives rise to serious environmental problems such as global warming and climate change [11].

Although renewable energy sources such as wind and solar energy are more environmentally friendly technologies, they still require significant landmass utilization in order to be a feasible means of energy generation [12]. It is shown in Fig. 1.1 that with the current rate of increase of the energy use, the renewables will be able to supply only around 27% of the global energy demand by the year 2040. For these reasons, alternative sources of energy need to be found and one of the most promising candidates is nuclear fusion [11].

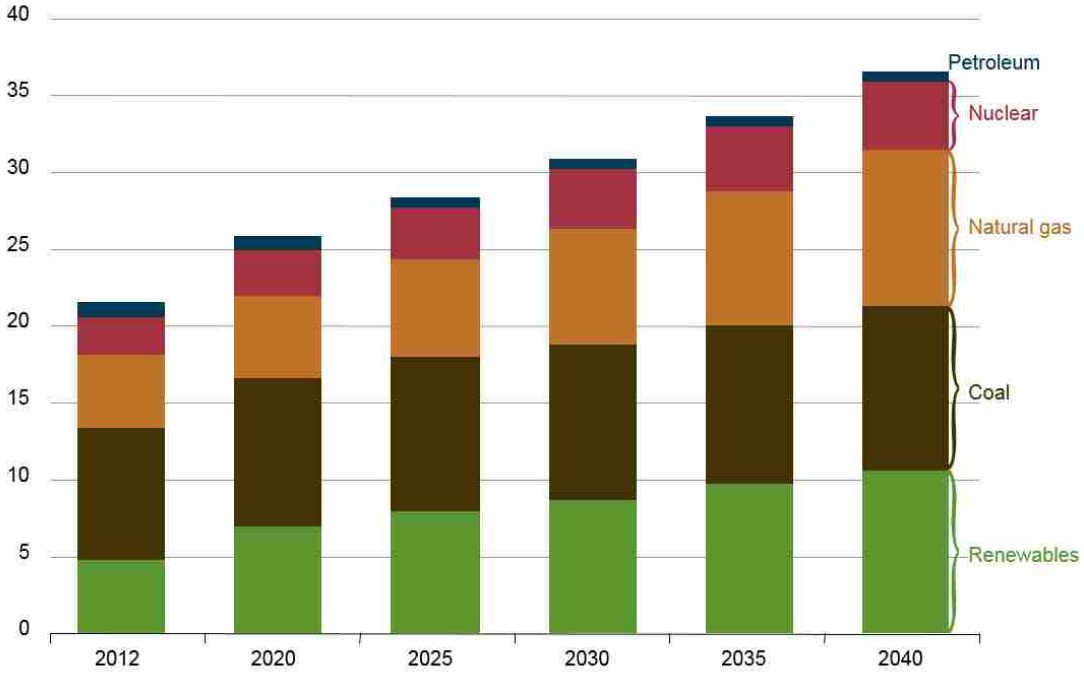

Figure 1.1: World net electricity generation by energy source, 2012-2040. (trillion kilowatthours). [4]

Conventional nuclear power plants operate based on nuclear fission, which produces energy through the splitting of heavy atoms like uranium. Unfortunately, the by-products of fission are highly radioactive, which require special storage and handling for thousands of years [12]. Fusion is the process that drives the production of energy in stars, such as the Sun [13]. In a typical fusion reaction, two light nuclei collide with each other and fuse together to form a heavier nucleus with a vast amount of energy release as a by-product [8]. One possible fusion reaction considered to generate energy is the so-called deuterium-tritium (D-T) fusion reaction (Fig. 1.2), in which the two isotopes of hydrogen (deuterium and tritium) are fused together under high pressure and temperature to form a heavier nucleus (helium) and a free energetic neutron. The D-T fusion reaction of interest can be written as

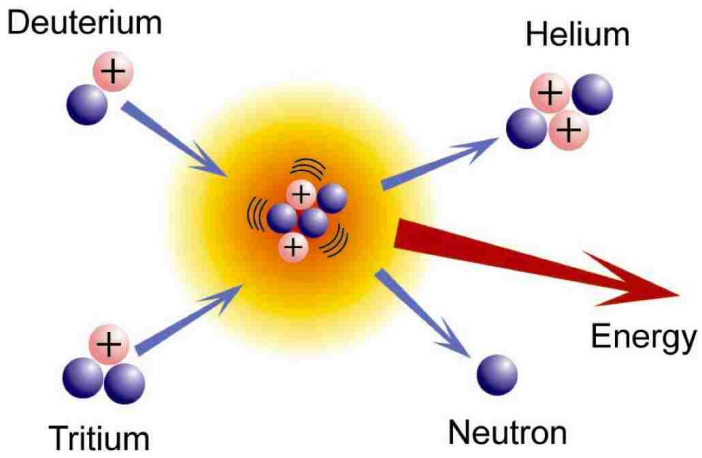

Figure 1.2: Schematic of the deuterium-tritium fusion reaction [5]. The products are helium and a free neutron. The total energy released is 17.6 MeV, out of which 3.5 MeV is carried by the helium, while 14.1 MeV is carried by the free neutron.

$$ {}^{2}_{1}\mathrm{D} + {}^{3}_{1}\mathrm{T} \rightarrow {}^{4}_{2}\mathrm{He} + {}^{1}_{0}\mathrm{n} + (17.6\ \mathrm{MeV}) \tag{1.1} $$

To maintain the above reaction, deuterium and tritium isotopes should be supplied. Deuterium can be extracted from sea water, while tritium is obtained artifically through neutron bombardment of lithium through the reaction

$$ {}^{6}_{3}\mathrm{Li} + {}^{1}_{0}\mathrm{n} \rightarrow {}^{4}_{2}\mathrm{He} + {}^{3}_{1}\mathrm{T} \tag{1.2} $$

Note that the neutron freed in (1.1) is used in (1.2) to produce tritium. Therefore, the reaction chain (1.1)-(1.2) is self-sufficient with deuterium (sea water) and lithium being the ultimate fuels, and helium generated as the ultimate product. There is sufficient lithium supply on Earth to maintain tritium breeding for thousands of years [8]. Since helium is not a radioactive gas, it can be collected to be used in many industrial or medical applications. The fueling process of a typical D-T fusion reactor is illustrated in Fig 1.3(a).

Besides having an abundant fuel supply, nuclear fusion provides more energy re-

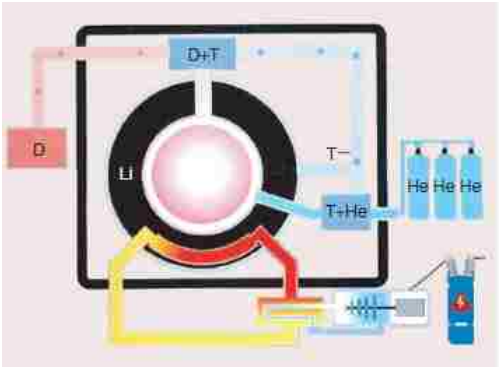

(a) Fueling process of a typical D-T fusion reactor [8].

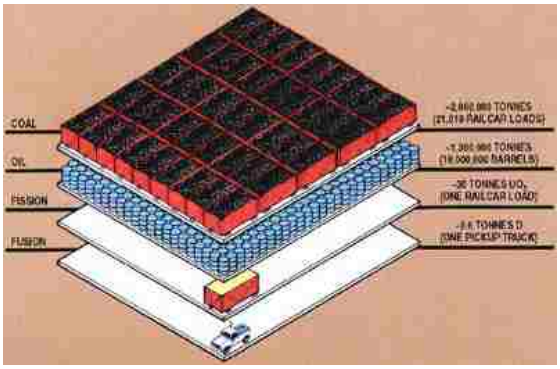

(b) Fuel amounts for various energy sources [14].

Figure 1.3: (a) Fueling process of a typical D-T fusion reactor: Fusion reaction takes place at the center of the reactor, where helium and energetic neutrons are released. High-energy neutrons hit the lithium blanket (depicted in black), where the reaction $\mathrm{Li} + \mathrm{n} \rightarrow \mathrm{T} + \mathrm{He}$ takes place to supply tritium fuel for additional fusion reactions. The lithium blanket is also used to convert the heat energy of the neutrons to electricity in a way similar to most other powerplants. Helium is stored in tanks to be used for industrial or medical applications. (b) Comparison of the fuel amounts required to generate the same energy output in coal, oil, nuclear fission, and nuclear fusion-based power plants.

leased per gram of fuel when compared to nuclear fission and all other fossil fuel alternatives (Fig. 1.3(b)). Contrary to fission, fusion poses no risk of a nuclear accident, generates no material for nuclear weapons, and produces mostly short-term, low-level, radioactive waste, which can be easily disposed of within a human lifetime [8]. All these benefits seem to make nuclear fusion a promising alternative energy source that could be used to overcome any potential energy or environmental crisis in the future.

1.2 Magnetic Confinement and Tokamak Devices

Despite all its benefits, including an abundant fuel supply, achieving controlled fusion on Earth is challenging. For nuclear fusion to happen, the hydrogen isotopes should overcome the Coulomb barrier, which normally repels them apart as they are both positively charged. The higher the temperature of the fuel is, the better the chances

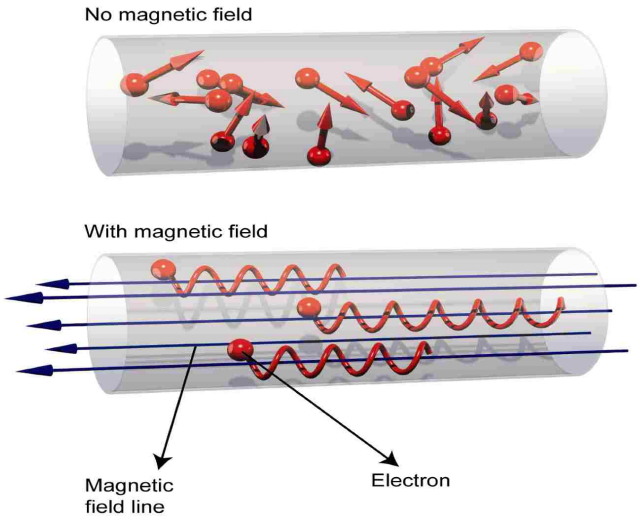

Figure 1.4: Magnetic confinement approach [6]: If there is no magnetic field imposed on a plasma, the charged particles are free to move arbitrarily and will eventually leave the confining vessel. On the other hand, a magnetic field imposes a force on the charged particles, which causes them to move along the field lines while gyrating around them.

to collide and fuse [11]. Therefore, in a typical nuclear fusion reactor, the temperature should be raised around 100 million degrees. At much lower temperatures, the reactants (hydrogen isotopes) separate from their electrons and form an ionized gas called plasma, which is considered as the fourth state of matter.

The main challenge of nuclear fusion is the development of a device that can confine the hot plasma for sufficiently long time while preventing it from hitting the walls of the confining device. In this way, more energy can be released through fusion reactions than the energy required for heating the plasma [11]. Among several confinement techniques, magnetic confinement [15] appears to be the most promising approach. In this specific confinement technique, magnetic fields are imposed to exert a force on the moving ionized particles and to confine them within a fixed volume [8]. Fig. 1.4 illustrates magnetic confinement through a comparison of the motion of the charged particles within a plasma that is unconfined and one that is confined by magnetic fields.

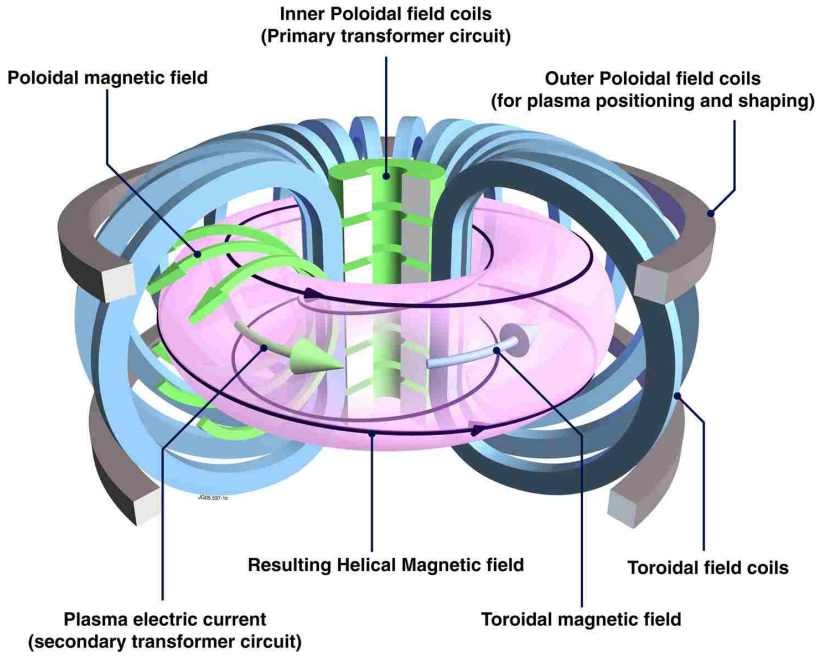

Figure 1.5: Schematic diagram of a tokamak device [7]: Toroidal field coils (shown in blue) are wrapped poloidally around the torus (i.e., going through the short way), while the poloidal field coils (shown in gray) are wrapped toroidally (i.e., going through the long way) around the torus [8]. The current applied at the center solenoid induces current inside the plasma through transformer action. The plasma current creates an additional poloidal magnetic field, resulting in helical magnetic field lines, which prevents plasma charged particles from leaving the torus.

Among several magnetic confinement devices, the tokamak [16] is one of the most promising concept to generate fusion power. The word "tokamak" is an acronym of the Russian words "TOroidalnaya KAmera ee MAgnitaya Katushka", which means "toroidal chamber with magnetic coils" [11]. A tokamak device therefore utilizes the magnetic confinement approach to nuclear fusion by exploiting the plasma's ability to conduct electrical current and interact with magnetic fields.

In a typical tokamak device, the magnetic field produced by both the large magnetic coils around the toroidal chamber and the current flowing toroidally in the plasma describes a helical path through the torus, i.e., the magnetic field lines curve around in the poloidal direction as well as in the toroidal direction. Hence, the magnetic field lines are closed on themselves, forming a torus as shown in Fig. 1.5.

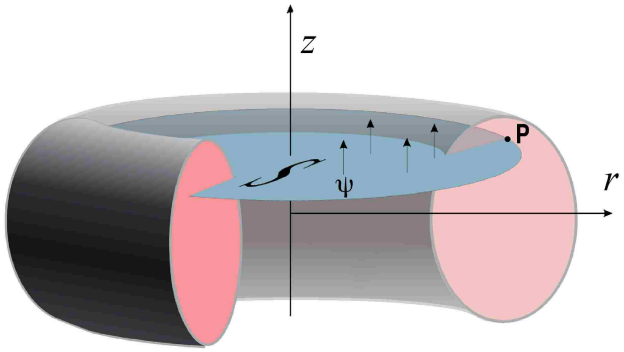

Figure 1.6: Definition of poloidal magnetic flux in a tokamak plasma [8]: The poloidal flux Ψ at a point P in the (r, z) cross section of the plasma is defined as the total flux through the horizontal circular disk passing through that point.

Following any magnetic field line a number of times around the torus a closed flux tube is mapped, a so called magnetic flux surface, which marks points of constant poloidal magnetic flux, Ψ (Fig. 1.6). Poloidal magnetic flux will be used extensively in the subsequent chapters of this dissertation as a radial index both for modeling and control purposes.

1.3 Spherical Torus vs. Tokamak

A spherical torus, or a spherical tokamak (ST), is a variation of the conventional tokamak concept, where the central hole of the torus is reduced in size. Hence, instead of a donut shape, the plasma edge looks almost like a sphere.

The main advantages of a spherical torus over the conventional tokamak geometry can be summarized as follows:

1. *Significantly higher β values* [17]. The efficiency of confinement is measured by the parameter β since it defines how much plasma kinetic pressure can be maintained by a given magnetic confining pressure [10]. Therefore, in a spherical tokamak, higher plasma pressure can be confined by applying less magnetic field,

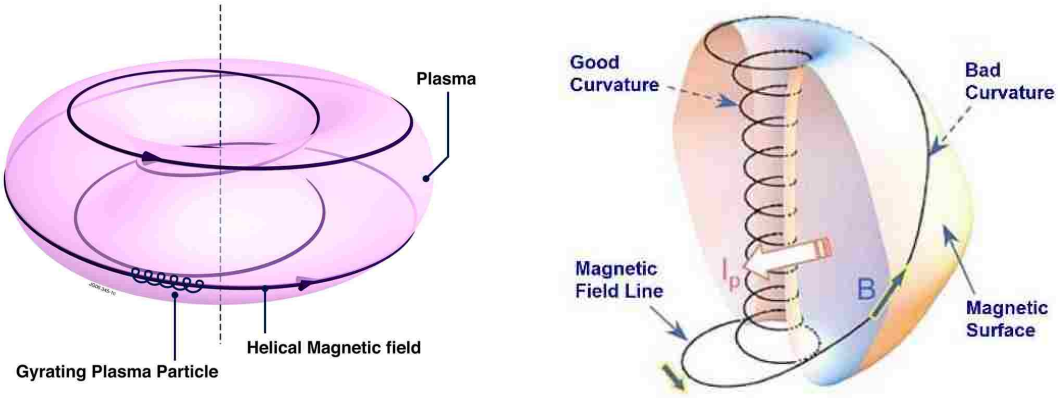

(a) Magnetic field lines in a tokamak [18]. (b) Magnetic field lines in a spherical torus [19].

Figure 1.7: Typical magnetic field line geometry in a (a) tokamak and (b) spherical torus.

giving rise to more fusion power since fusion power is proportional to the square of the plasma pressure.

2. *Increase in plasma stability* [19]. This is a consequence of the spherical geometry. As can be seen in Fig. 1.7(b), magnetic field lines in a spherical torus are highly twisted at the core section, while they are very steep at the outer, spherical surface of the plasma when compared to the magnetic field line geometry in a typical tokamak configuration (Fig. 1.7(a)). Hence, charged particles can spend more time in the favorable core section of the plasma, where magnetic field is stronger and plasma is more stable, than the unfavorable, less stable outer edge of the plasma. Plasma is more stable in the core region of the torus because the centrifugal force acting on the charged particles pushes them to enter into the dense plasma region. Conversely, at the outer part of the torus, the centrifugal force pushes the charged particles out of the plasma into a less dense vacuum region, which triggers an instability similar to Rayleigh-Taylor.

3. *Potential to produce high self-generated (bootstrap) current* [20]. Plasma in a spherical torus may create its own confining magnetic field and current through the magnetic dynomo action, which is the way celestial bodies, such as earth and sun generate their magnetic fields. In this specific regime, fast-moving, super hot plasma creates its own confining magnetic fields, which in turn pass through the flowing plasma itself and induce more current which also supplies the externally applied magnetic fields.

4. *Simpler design, easier maintenance and lower operating costs* [20]. Smaller, more compact external magnetic coils are used in a spherical tokamak when compared to a tokamak, where the external coils are complicated and expensive. Moreover, if one of the coils of a tokamak goes down, it creates an expensive and demanding repair job.

On the other hand, the main drawbacks of a spherical tokamak are the difficulty to scale up the geometry and the plasma behavior being more complex to control and predict.

1.4 The National Spherical Torus eXperiment - Upgrade (NSTX-U) Project

NSTX-U, shown in Fig. 1.8(a) and schematically depicted in Fig. 1.8(b), is one of the major spherical torus experimental facilities in the world. NSTX-U is a leading candidate for facilities designed to study plasma material interactions, nuclear component testing, or to generate fusion power [17]. The NSTX-U project will shed light on important physics problems including the electron transport scaling with field and current, fast particle physics, and sustainment of non-inductive high-β scenarios [2].

(a) NSTX-U facility [21].

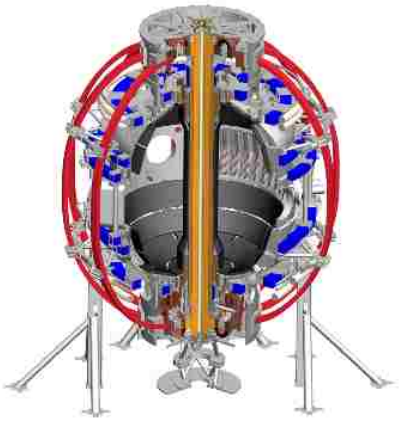

(b) Schematic of the NSTX-U [3].

Figure 1.8: (a) Inside the NSTX-U test cell in Princeton Plasma Physics Laboratory (PPPL), Princeton, NJ, USA. (b) Schematic of the NSTX-U device: Shown in blue and red are the external poloidal and toroidal magnetic field coils, respectively. The center stack is shown in yellow and the vacuum chamber is shown in dark grey.

NSTX-U is a substantial upgrade to the former NSTX device [17]. The most important components of the upgrade are [3]:

1. A larger center-stack (Fig. 1.9(a)), including the inner leg of the toroidal field (TF) coils, the ohmic heating (OH) solenoid, and some divertor coils. The new center stack is capable of doubling the toroidal field, tripling the solenoid flux, and increasing the flat-top current operation duration up to a factor of 5.

2. A second, more tangential neutral beam injector (Fig. 1.9(b)) to double the plasma heating and external current drive while also increasing the current drive efficiency and controllability.

3. Structural enhancements to withstand up to a factor of 4 increase in electromagnetic loads enabling a doubling of the plasma current.

Schematics of NSTX and NSTX-U facilities are shown in Fig. 1.10, and their respective device and plasma parameters are listed in Table 1.1 [22].

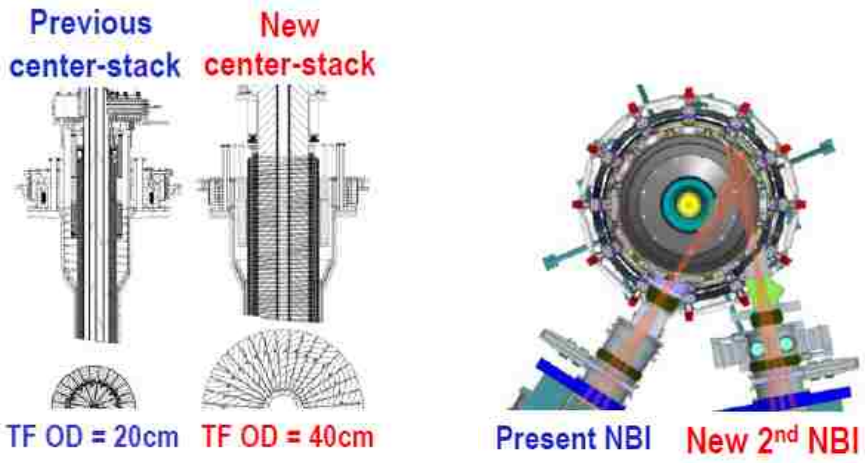

(a) (b)

Figure 1.9: Components of the NSTX-Upgrade [3]: (a) Previous vs. new center stacks (with 20 cm and 40 cm outer diameters, respectively); (b) Top view of NSTX-U showing the additional neutral beam injector with more tangential beam injection capability in addition to the existent neutral beam injector of NSTX.

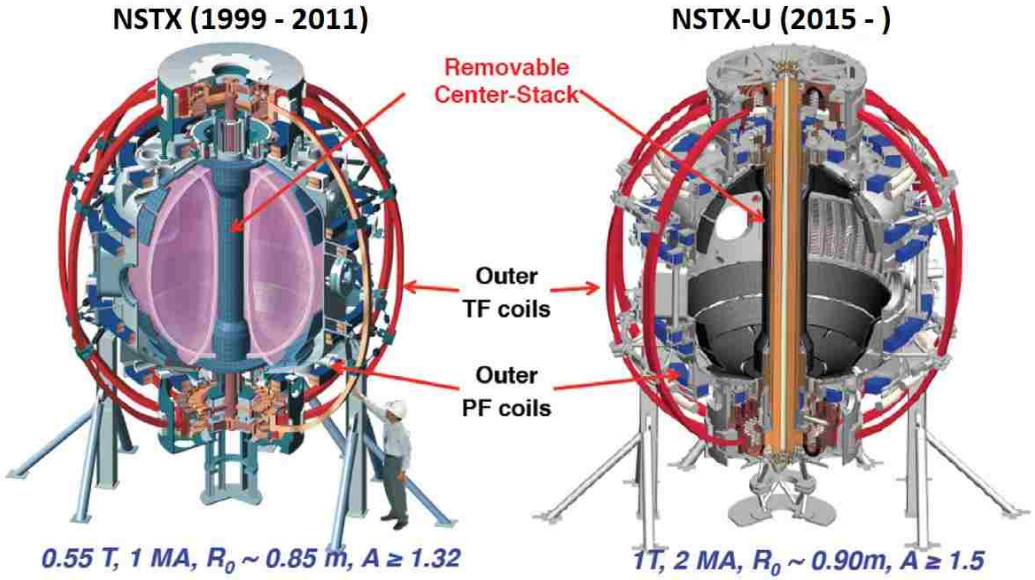

Figure 1.10: Schematics of NSTX and NSTX-U devices [3]: NSTX-U retains the basic configuration of NSTX, as much of the NSTX facility is utilized including the vacuum vessel (VV) and outer toroidal field (TF) and poloidal field (PF) coils. The new centre-stack with a four times larger TF coil cross section and three times larger ohmic flux, permits the doubling of the TF from ∼0.5 to 1 T and the plasma current from 1 to 2 MA, while expanding the plasma pulse length from ∼1 to 5 s.

PARAMETER	NSTX	NSTX-U
Major Radius R_0 [m]	0.86	0.94
Aspect Ratio R_0/a	$\geq$1.3	$\geq$1.5
Plasma Current [MA]	1	2
Plasma Temperature [°C]	5×10^6	10×10^6
Toroidal Field [T]	0.5	1
Heating Power [MW]	5-7	10-14

Table 1.1: Parameters ranging from NSTX to NSTX-U [3].

The main mission of the NSTX-U research program is to develop the physics basis for a compact ST-based Fusion Nuclear Science Facility (FNSF), which is the critical major next step in the US fusion program [3], [22]. Offering a compact design with reduced cost and tritium consumption, NSTX-U research will provide access to new physics regimes sufficiently advanced to provide information for the optimal FNSF configuration [3]. At the same time, the unique operating regimes of NSTX-U can contribute to several important issues in the physics of burning plasmas to optimize the performance of ITER [22], which will be the first fusion device to produce net energy. [23]. The NSTX-U program further aims at determining the attractiveness of the compact ST for addressing key research needs on the path toward a fusion demonstration power plant, DEMO [22], which could be used to investigate the commercial production of fusion-based-electricity beyond ITER [24].

1.5 Current Profile Control in NSTX-U

The next-step operational goals for NSTX-U include the non-inductive sustainment of high-β, high performance, equilibrium scenarios with neutral beam heating and longer pulse durations [17]. Plasma control is an essential part of the work towards the realization of these next-step operational goals in NSTX-U. Emerging control

topics for NSTX-U are [2]

1. Plasma boundary shape control.

2. Power and particles exhaust control.

3. Current and rotation profiles control.

4. Edge transport barrier control.

Setting up a suitable current density profile plays a critical role in the achievement of advanced tokamak scenarios characterized by high confinement and the non-inductive sustainment of the plasma current necessary for steady-state operation. The safety factor, q, (defined as the ratio between the number of times a magnetic field line goes toroidally (i.e., the long way) around the tokamak to the number of times it goes around poloidally (i.e., the short way)) is a key property affecting stability, performance, and steady-state operation in fusion plasmas. It can be shown that the value of q on a flux surface is inversely proportional to the plasma current enclosed by that flux surface. Hence, increasing (or decreasing) the current flow inside a flux surface reduces (or raises) q on that surface. Thus, one can speak interchangeably of the control of the current density profile and control of the q-profile. Recent progress in current profile control is described in [25,26] for the JT-60U tokamak [27], in [28,29] for the Tore Supra tokamak [30], in [31–33] for the JET tokamak [34], and in [35–43] for the DIII-D tokamak [44].

NSTX-U has been completed in 2015 and plasma operation is undergoing according to the research plans specified for the 2014-2018 fiscal years [3]. However, various adjustments are still needed before enabling plasma control experiments on the real machine. Recent work towards plasma control in NSTX-U is presented in [2], [45].

Multivariable optimal linear quadratic gaussian and PID control techniques are utilized to control the central safety factor and normalized β (β_N) based on a control-oriented model obtained from system identification simulations in [2]. Whereas, a Linear-Quadratic-Integral (LQI) optimal controller is designed based on a data-driven model to control the plasma rotation in NSTX by using neutral beam injection (NBI) and neoclassical toroidal viscosity (NTV) actuations in [45] (this work is being extended to NSTX-U). In both pieces of work, the controllers are tested in closed-loop simulations in the high-fidelity, physics-based transport code TRANSP [46] through the recently developed Expert routine [2].

The aim of this work is to develop a model-based, combined feedforward and feedback controller that can enable regulation of the current density profile (or q-profile) in NSTX-U by actuating the total plasma current and the powers of the individual neutral beam injectors. A nonlinear, control-oriented, physics-based model is proposed to describe the evolution of the poloidal magnetic flux profile, which is directly related to the q-profile. This first-principles-driven (FPD) model is tailored to the NSTX-U geometry and actuators based on the simulated data of the plasma evolution in NSTX-U obtained from the fully predictive TRANSP advanced tokamak simulation code. The model will be refined with experimental data once a meaningful plasma is obtained in NSTX-U.

A two-component control design approach is followed for the regulation of the current density profile. First, nonlinear optimization techniques are used to compute offline actuator trajectories that achieve specific plasma scenarios. Given a desired operating state, the optimizer produces the actuator trajectories that steer the plasma to such state. The objective of the feedforward control design stage is to provide a systematic approach to advanced scenario planning in NSTX-U.

Secondly, feedback control algorithms are developed to track a desired current density profile evolution by modifying online the previously computed feedforward trajectories. LQI Optimal Control and Model Predictive Control (MPC) are used to design the feedback controllers. The proposed controllers are designed based on a fully-linearized version of the NSTX-U-tailored FPD, control-oriented model, and their performance is assessed based on closed-loop nonlinear simulations. The performance of the LQI optimal controller is also validated through closed-loop TRANSP simulations.

Experimental testing of the proposed current-profile controller is not a part of this dissertation due to the fact that NSTX-U was not in operation during the last few years. Although the upgrade was completed in 2015, a meaningful plasma could not yet generated. As relevant plasmas are achieve, experimental data could be used to refine the proposed FPD model and the optimal feedforward controller could be tested. Once the motional Stark effect (MSE) magnetic field pitch angle diagnostics [47] start operating, the developed feedback controllers could be tested in the actual NSTX-U device. This dissertation work already sets the foundation that is necessary to make active current profile control in NSTX-U a reality in the near future.

1.6 Dissertation Outline

This dissertation is organized as follows:

Chapter 2

In this chapter, a physics-based, control-oriented model describing the temporal evolution of the current profile is obtained by combining the magnetic diffusion equation with empirical correlations obtained at NSTX-U for the electron density, electron

temperature, and non-inductive current drives. The resulting first-principles physics-based control-oriented model is tailored to NSTX-U based on the predictions of the TRANSP simulation code. The model's prediction capabilities are illustrated by comparing the prediction to simulated data from TRANSP for some reference runs.

Chapter 3

In this chapter, the physics-based, control-oriented model is used in a nonlinear numerical optimization algorithm based on the Sequential Quadratic Programming (SQP) approach to synthesize an open-loop actuator trajectory optimizer for the NSTX-U. The goal of the feedforward optimizer is to compute offline actuator trajectories to achieve specific plasma scenarios with the goal of supporting experimental effort on scenario development for NSTX-U.

Chapter 4

In this chapter, the proposed control-oriented model is embedded into the control design process to synthesize a linear quadratic integral (LQI) optimal controller capable of regulating the current density profile around a desired target profile while rejecting disturbances. Neutral beam injectors, electron density, and the total plasma current are used as actuators. The effectiveness of the proposed controller in regulating the current density profile in NSTX-U is demonstrated in closed-loop nonlinear simulations. The performance of the optimal controller is also validated in closed-loop control simulations carried out in TRANSP through the recently developed Expert routine.

Chapter 5

In this chapter, the proposed control-oriented model is embedded in a feedback control scheme based on a model predictive control (MPC) strategy to track a desired current density profile evolution specified indirectly by a desired rotational transform profile. An integrator is embedded into the standard MPC formulation to account for various modeling uncertainties and external disturbances. The neutral beam powers, electron density, and total plasma current are used as actuators. The effectiveness of the proposed MPC strategy in regulating the current density profile in NSTX-U is demonstrated in closed-loop simulations.

Chapter 6

In this final chapter, the contributions of this dissertation are provided and possible future work is discussed.

Chapter 2

Physics-based Control-oriented Modeling of the Current Density Profile Evolution in NSTX-U

2.1 Introduction

Active control of the toroidal current density profile is among those plasma control milestones that the NSTX-U program must achieve to realize its next-step operational goals characterized by the high-performance, MHD-stable plasma operation with neutral beam heating, and longer pulse durations [17]. As a first step towards feedback control design, a physics-based, control-oriented model is developed in this chapter. Model-based control is motivated by the coupled, nonlinear, multivariable, distributed-parameter plasma dynamics. The proposed control-oriented model captures the spatial-temporal evolution of the current density profile in response to non-inductive current drives and heating systems.

The main goal of this chapter is to convert the first-principles physics model of the poloidal magnetic flux profile evolution [48], which is related to the toroidal current density profile evolution in the spherical torus, into a form suitable for control design. This is achieved by combining the magnetic flux diffusion equation with physics-based control-oriented models for the electron density and temperature profiles, the plasma resistivity, and the non-inductive current-drives (neutral beam injection and bootstrap effect), thereby obtaining a first-principles-driven (FPD) model. Note that the resulting control-oriented model needs only to capture the dominant physics that describe how the control actuators affect the poloidal magnetic flux evolution since feedback control compensates for the modeling uncertainties.

Earlier work towards physics-based modeling of plasma dynamics can be found in [49–61]. In Barton et al. [62], a general physics-based, control-oriented modeling approach is developed with the emphasis on high performance (H-mode) scenarios in the ITER [23] and DIII-D [44] tokamaks by using DINA-CH/CRONOS [63] and TRANSP codes to obtain simulated data of the plasma evolution to tailor the FPD model to ITER and DIII-D tokamaks, respectively. The modeling work presented in this chapter follows the same modeling approach but focusing on the NSTX and NSTX-U geometry and actuators. The TRANSP advanced tokamak simulation code is utilized to obtain simulated data of the plasma evolution to tailor the FPD model to NSTX and NSTX-U. The FPD model's prediction capabilities are shown by comparing the predictions to simulation data from TRANSP for some reference runs.

The remainder of this chapter is organized as follows. First-principles modeling of the current density profile evolution is introduced in Section 2.2. Simplified, control-oriented models of various plasma parameters are described in Section 2.3. Physics-based control-oriented model of poloidal magnetic flux profile evolution is obtained in Section 2.4. The proposed FPD model is tailored to the NSTX and NSTX-U in

Sections 2.5 and 2.6, respectively. Finally, a brief conclusion and future work are provided in Section 2.7.

2.2 Current Density Profile Evolution Model

Any arbitrary quantity that is constant on each magnetic flux surface within the tokamak plasma can be used to index the flux surfaces, which are graphically depicted in Fig. 2.1. In this work, we choose the mean effective minor radius, ρ, of the flux surface, i.e., $\pi B_{\phi,0}\rho^2 = \Phi$, as the indexing variable, where Φ is the toroidal magnetic flux and $B_{\phi,0}$ is the vacuum toroidal magnetic field at the geometric major radius R_0 of the tokamak. The normalized effective minor radius is defined as $\hat{\rho} = \rho/\rho_b$, where ρ_b is the mean effective minor radius of the last closed flux surface.

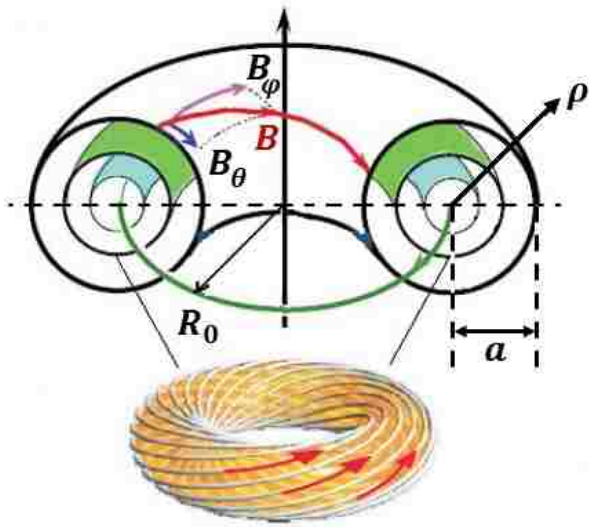

Figure 2.1: Magnetic flux surfaces in a tokamak [9]. The helical magnetic field ($\vec{B}$) in a tokamak plasma is composed of toroidal ($\vec{B}_\phi$) and poloidal ($\vec{B}_\theta$) fields. The poloidal magnetic flux is defined as $\Psi = \int \vec{B}_\theta \cdot d\vec{A}_Z$, where $\vec{A}_Z$ denotes a disk of radius R that is perpendicular to a unit vector in the vertical direction. Also shown are the geometric major radius, R_0, and the minor radius, a, of the plasma.

2.2.1 Rotational Transform and Safety Factor

The rotational transform (ι) and safety factor (q) are two simply related surface quantities that play important role in both magnetohydrodynamic (MHD) equilibrium and stability of the fusion plasmas [10].

Based on a purely geometric description, the rotational transform (ι) can be related to the twist of the magnetic field lines. To illustrate, a magnetic field line can be projected onto a given poloidal cross section as shown in Fig. 2.2. Starting at a poloidal angle of θ_0 with respect to the magnetic axis, the field line returns to a slightly different angle, $\theta_0 + \Delta\theta$, on the flux surface after one complete revolution around the torus. Note that the angle $\Delta\theta$ depends on the poloidal angle, θ_0, where the line started. Therefore, the rotational transform is defined as the average value of the angle $\Delta\theta$ after infinite number of transits [10]

$$\iota = \lim_{N\to\infty} \frac{1}{N} \sum_{i=1}^{N} \Delta\theta_i \tag{2.1}$$

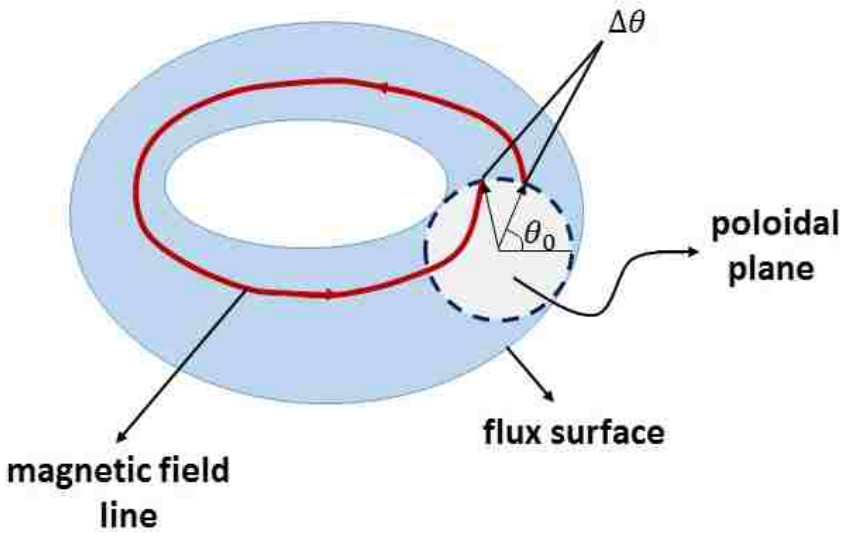

Figure 2.2: Magnetic field line projections used in the definition of the ι-profile. [10].

On the other hand, the safety factor (q) is defined as the ratio between the number of times a magnetic field line goes toroidally (i.e., the long way) around the torus to the number of times it goes around poloidally (i.e., the short way). Therefore, the safety factor q is inversely related to ι as [10]

$$q = \frac{2\pi}{\iota} \tag{2.2}$$

Equilibria can be designed with small, moderate, or large ι. Large ι usually implies a robust toroidal equilibrium, but can also indirectly give rise to MHD instabilities [10]. Therefore, active control of the ι-profile (or, q-profile) is important for the realization of the next-step operational goals of NSTX-U, which are defined briefly in Section 1.5, and with detail in [17].

2.2.2 Relation between Current Density Profile and Poloidal Flux Gradient Profile

Based on a magnetic description [16], the rotational transform (ι-profile) and the toroidal current density profile (j_ϕ) can be related through

$$\iota(\hat{\rho}, t) = \frac{R_0 \mu_0}{\hat{\rho}^2 B_\phi} \int_0^{\hat{\rho}} j_\phi(\hat{\rho}', t) \hat{\rho}' d\hat{\rho}', \tag{2.3}$$

where μ_0 is the permeability of the free space. Therefore, the toroidal current density can be specified indirectly by the rotational transform ι, which is also related to poloidal magnetic flux Ψ and is defined as $\iota(\hat{\rho}, t) = -d\Psi/d\Phi$. Using $\Phi = \pi B_{\phi,0} \rho^2$ and $\hat{\rho} = \rho/\rho_b$, the ι-profile can also be expressed as

$$\iota(\hat{\rho}, t) = -\frac{d\Psi}{d\Phi} = -\frac{2\pi d\psi}{d\Phi} = -\frac{2\pi \frac{\partial \psi}{\partial \hat{\rho}}}{\frac{\partial \Phi}{\partial \rho} \frac{\partial \rho}{\partial \hat{\rho}}} = -\frac{\partial \psi / \partial \hat{\rho}}{B_{\phi,0} \rho_b^2 \hat{\rho}}, \tag{2.4}$$

where $\psi(\hat{\rho}, t)$ is the poloidal stream function, which is closely related to the poloidal flux Ψ ($\Psi = 2\pi\psi$).

Combining (2.3) and (2.4), it can be shown that the control of the current density profile $j_\phi(\hat{\rho}, t)$ is equivalent to the control of the ι-profile, which in turn is equivalent to the control of the poloidal flux gradient profile $\partial\psi/\partial\hat{\rho}$.

2.2.3 Plasma Poloidal Magnetic Flux Diffusion Equation

The evolution of the poloidal magnetic flux is given in normalized cylindrical coordinates by the magnetic diffusion equation (MDE) [49]:

$$\frac{\partial\psi}{\partial t} = \frac{\eta(T_e)}{\mu_0\rho_b^2\hat{F}^2}\frac{1}{\hat{\rho}}\frac{\partial}{\partial\hat{\rho}}\left(\hat{\rho}D_\psi\frac{\partial\psi}{\partial\hat{\rho}}\right) + R_0\hat{H}\eta(T_e)\frac{\left\langle \bar{j}_{ni}\cdot\bar{B}\right\rangle}{B_{\phi,0}}, \tag{2.5}$$

with boundary conditions

$$\left.\frac{\partial\psi}{\partial\hat{\rho}}\right|_{\hat{\rho}=0} = 0 \qquad \left.\frac{\partial\psi}{\partial\hat{\rho}}\right|_{\hat{\rho}=1} = -\frac{\mu_0}{2\pi}\frac{R_0}{\hat{G}\Big|_{\hat{\rho}=1}\hat{H}\Big|_{\hat{\rho}=1}}I_p(t), \tag{2.6}$$

where $I_p(t)$ is the total plasma current, η is the plasma resistivity, T_e is the electron temperature, μ_0 is the vacuum permeability, $\bar{j}_{ni}$ is any source of noninductive current density, $\bar{B}$ is the magnetic field, $\langle\rangle$ denotes a flux-surface average, $D_\psi(\hat{\rho}) = \hat{F}(\hat{\rho})\hat{G}(\hat{\rho})\hat{H}(\hat{\rho})$, where $\hat{F}$, $\hat{G}$, $\hat{H}$ are geometric factors pertaining to the magnetic configuration of a particular plasma equilibrium. The geometric parameters are defined as follows

$$\hat{F} = \frac{R_0 B_{\phi,0}}{RB_\phi(R,Z)}, \qquad \hat{G} = \left\langle \frac{R_0^2}{R^2}|\nabla\rho|^2 \right\rangle, \qquad \hat{H} = \frac{\hat{F}}{\langle R_0^2/R^2\rangle}, \tag{2.7}$$

where B_ϕ is the toroidal magnetic field at the spatial location (R, Z) in the poloidal plane of the tokamak. The model (2.5)-(2.7) makes the simplifying assumption that

the magnetic geometry is fixed in time, which excludes two potential sources of flux:

1. A change in ρ_b, either by a change in shape of the last closed flux surface or in $B_{\phi,0}$.

2. A change in location of the geometric center of the interior flux surfaces relative to that of the last closed flux surface, such as changes in the Shafranov shift that occur during a plasma β or internal inductance change.

The first-principles model of the poloidal magnetic flux evolution (2.5) needs to be converted into a form suitable for control design. This is mainly accomplished by combining the poloidal flux evolution model with simplified control-oriented models of the electron density and temperature, the plasma resistivity, and the noninductive current drives [62] tailored to the NSTX-U geometry and actuators. Note that the simplified physics-based models need only to capture the dominant physics that describe how the control actuators affect the respective plasma parameters since feedback control compensates for the modeling uncertainties.

2.3 Simplified Modeling of Plasma Parameters

In this section, empirical models are developed based on physical observations and simulated data from NSTX-U for the electron density and temperature profiles, the noninductive current deposition profiles and the plasma resistivity for a general operating scenario in order to close the magnetic diffusion equation model (2.5)-(2.7) and obtain a "control-oriented" model of the poloidal flux profile evolution. All those control-oriented, physics-based models take a "separation of variables" form, i.e., spatial-temporal dependence of plasma parameters is separated. It is important to emphasize that the models developed in this section are not designed for physical un-

derstanding, rather they are meant to capture the dominant physics that describe how the control actuators affect the parameters, and hence the current profile evolution.

The control actuators for NSTX are:

1. Electron density.
2. The total plasma current, $I_p(t)$, which is itself controlled by the poloidal field coil system.
3. Auxiliary heating/current-drive (H&CD) sources, which are comprised of neutral beam injectors as introduced in Section 1.4.

2.3.1 Electron Density Modeling

The electron density profile $n_e(\hat{\rho}, t)$ is modeled as

$$n_e(\hat{\rho}, t) = n_e^{prof}(\hat{\rho}) u_n(t), \tag{2.8}$$

where $n_e^{prof}(\hat{\rho})$ is a reference profile and $u_n(t)$ regulates the time evolution of the electron density. Note that n_e^{prof} is obtained by evaluating the experimental or simulated n_e at a reference time $t_{r_{n_e}}$, i.e.,

$$n_e^{prof}(\hat{\rho}) = n_e(\hat{\rho}, t_{r_{n_e}}) \tag{2.9}$$

This model assumes the control action employed to regulate the electron density weakly affects the radial distribution of the electrons. This decision is motivated by the fact that tight control of $n_e(\hat{\rho}, t)$ in experiments is very challenging.

2.3.2 Electron Temperature Modeling

In the formulation of the electron temperature model, we assume a tight coupling between the plasma electron and ion species, i.e., $T_e(\hat{\rho},t) \approx T_i(\hat{\rho},t)$ and $n_e(\hat{\rho},t) \approx n_i(\hat{\rho},t)$, where $T_i(\hat{\rho},t)$ and $n_i(\hat{\rho},t)$ are the ion temperature and density profiles, respectively. As a result, we neglect the explicit electron-ion equilibration power in the development of the model. Under these assumptions, the plasma kinetic pressure p and stored energy density W_d are expressed as

$$\begin{aligned} p(\hat{\rho},t) &= n_e(\hat{\rho},t)T_e(\hat{\rho},t) + n_i(\hat{\rho},t)T_i(\hat{\rho},t) \\ &= 2n_e(\hat{\rho},t)T_e(\hat{\rho},t) \qquad (2.10) \\ W_d(\hat{\rho},t) &= \frac{3}{2}n_e(\hat{\rho},t)T_e(\hat{\rho},t) + \frac{3}{2}n_i(\hat{\rho},t)T_i(\hat{\rho},t) \\ &= 3n_e(\hat{\rho},t)T_e(\hat{\rho},t) \qquad (2.11) \end{aligned}$$

The electron temperature profile is modeled as

$$T_e(\hat{\rho},t) = \begin{cases} k^1_{T_e}(\hat{\rho})\left[T_e^{prof}(\hat{\rho}) - T_e^{prof}(\hat{\rho}_{tb})\right] I_p(t)^{\gamma} P_{tot}(t)^{\varepsilon} n_e(\hat{\rho},t)^{\zeta} & \\ +k^2_{T_e}(\hat{\rho}_{tb})^{\omega} T_e^{prof}(\hat{\rho}_{tb}) I_p(t)^{\lambda} P_{tot}(t)^{\nu} n_e(\hat{\rho}_{tb},t)^{\xi}, & 0 \le \hat{\rho} < \hat{\rho}_{tb} \\ k^2_{T_e}(\hat{\rho})^{\omega} T_e^{prof}(\hat{\rho}) I_p(t)^{\lambda} P_{tot}(t)^{\nu} n_e(\hat{\rho},t)^{\xi}, & \hat{\rho}_{tb} \le \hat{\rho} \le 1 \end{cases} \qquad (2.12)$$

where $\hat{\rho}_{tb}$ is the spatial location of the plasma edge energy transport barrier [64], $k^1_{T_e}$ and $k^2_{T_e}$ are constants, $T_e^{prof}(\hat{\rho})$ is a reference profile, and $P_{tot}(t)$ is the total power injected into the plasma. The constants γ, ε, and ζ describe how the temperature in the plasma core scales with the various parameters. The constants λ, ν, and ξ describe how the temperature outside of the plasma edge transport barrier scales with the various parameters. Note that T_e^{prof} is evaluated at a reference time $t_{r_{T_e}}$,

i.e.,

$$T_e^{prof}(\hat{\rho}) = T_e(\hat{\rho}, t_{r_{T_e}}) \tag{2.13}$$

and the constant ω is 1 if the temperature outside of the edge transport barrier scales with the various parameters and is 0 otherwise. The constants $k^1_{T_e}$ and $k^2_{T_e}$ are expressed as

$$k^1_{T_e}(\hat{\rho}) = \left[I_p(t_{r_{T_e}})^{\gamma} P_{tot}(t_{r_{T_e}})^{\varepsilon} n_e(\hat{\rho}, t_{r_{T_e}})^{\zeta} \mathrm{A}^{\gamma} \cdot \mathrm{W}^{\varepsilon} \cdot \mathrm{m}^{(-3)^{\zeta}} \right]^{-1}, \tag{2.14}$$

$$k^2_{T_e}(\hat{\rho}) = \left[I_p(t_{r_{T_e}})^{\lambda} P_{tot}(t_{r_{T_e}})^{\nu} n_e(\hat{\rho}, t_{r_{T_e}})^{\xi} \mathrm{A}^{\lambda} \cdot \mathrm{W}^{\nu} \cdot \mathrm{m}^{(-3)^{\xi}} \right]^{-1}, \tag{2.15}$$

where $k^1_{T_e}$ is defined on the interval $0 \leq \hat{\rho} < \hat{\rho}_{tb}$ and $k^2_{T_e}$ is defined on the interval $\hat{\rho}_{tb} \leq \hat{\rho} \leq 1$.

The total injected power $P_{tot}(t)$ is expressed as

$$P_{tot}(t) = P_{ohm}(t) + P_{aux}(t) - P_{rad}(t), \tag{2.16}$$

where $P_{ohm}(t)$ is the ohmic power, $P_{aux}(t)$ is the total auxiliary H&CD power and $P_{rad}(t)$ is the radiated power. The ohmic power is modeled as

$$P_{ohm}(t) \approx \mathcal{R}_p(t) I(t)^2, \tag{2.17}$$

where $\mathcal{R}_p(t)$ is the global plasma resistance, which is expressed as

$$\mathcal{R}_p(t) \approx 2\pi R_0 \Big/ \int_{\hat{\rho}} \left[\frac{1}{\eta(\hat{\rho}, t)} \frac{dS}{d\hat{\rho}} d\hat{\rho} \right], \tag{2.18}$$

where S denotes a magnetic surface within the plasma. The total auxiliary H&CD

power is expressed as

$$P_{aux}(t) = \sum_{i=1}^{n_{nbi}} \eta_i P_i(t), \tag{2.19}$$

where $P_i(t)$ is the individual neutral beam injector powers, n_{nbi} is the total number of neutral beam launchers, which is 3 for NSTX, and 6 for NSTX-U. The effectiveness of each neutral beam injector in increasing the total stored energy in the plasma is captured through the efficiency constant, η_i.

The radiative power density losses are modeled in [16] as

$$Q_{rad} = k_{brem} Z_{eff} n_e(\hat{\rho}, t)^2 \sqrt{T_e(\hat{\rho}, t)}, \tag{2.20}$$

where $k_{brem} = 5.5 \times 10^{-37}$ $\mathrm{Wm}^3/\sqrt{\mathrm{keV}}$ is the Bremsstrahlung radiation coefficient and Z_{eff} is the effective atomic number of the ions in the plasma, which is defined as

$$Z_{eff} = \frac{1}{n_e} \sum_{\text{all ions}} n_j Z_j^2, \tag{2.21}$$

where n_j and Z_j are the density and atomic number of the j-th ion species. In this work, we assume that Z_{eff} is a constant in space and time. The radiated power is then expressed as

$$P_{rad}(t) = \int_0^1 Q_{rad}(\hat{\rho}, t) \frac{dV}{d\hat{\rho}} d\hat{\rho}, \tag{2.22}$$

where V denotes the volume enclosed by a magnetic surface within the plasma.

2.3.3 Plasma Resistivity Modeling

The resistivity η scales with the electron temperature as

$$\eta(\hat{\rho}, t) = \frac{k_{sp}(\hat{\rho}) Z_{eff}}{T_e(\hat{\rho}, t)^{3/2}}, \tag{2.23}$$

where

$$k_{sp}(\hat{\rho}) = \frac{\eta(\hat{\rho}, t_{r_\eta}) T_e(\hat{\rho}, t_{r_\eta})^{3/2}}{Z_{eff}} \ \Omega\mathrm{m}(\mathrm{keV})^{3/2} \tag{2.24}$$

is a constant that is evaluated at a reference time t_{r_η}.

2.3.4 Noninductive Current-Drive Modeling

The total noninductive current-drive in NSTX-U is produced by the auxiliary neutral beam launchers and the bootstrap current, and is expressed as

$$\frac{\left\langle \bar{j}_{ni} \cdot \bar{B} \right\rangle}{B_{\phi,0}} = \sum_{i=1}^{n_{nbi}} \frac{\left\langle \bar{j}_i \cdot \bar{B} \right\rangle}{B_{\phi,0}} + \frac{\left\langle \bar{j}_{bs} \cdot \bar{B} \right\rangle}{B_{\phi,0}}, \tag{2.25}$$

where n_{nbi} is the number of neutral beam injectors (i.e., $n_{nbi} = 3$ for NSTX, and $n_{nbi} = 6$ for NSTX-U), $\bar{j}_i$ is the noninductive current density generated by the individual neutral beam injectors, and $\bar{j}_{bs}$ is the noninductive current density generated by the bootstrap effect [65].

2.3.4.1 Neutral Beam Injection Current-Drive

We model each auxiliary noninductive current-source as the time varying power in each actuator multiplied by a constant deposition profile in space. Therefore, the noninductive toroidal current density provided by each individual neutral beam injector is modeled as

$$\frac{\left\langle \bar{j}_i \cdot \bar{B} \right\rangle}{B_{\phi,0}}(\hat{\rho}, t) = k_{nbi_i}^{prof}(\hat{\rho}) j_{nbi_i}^{dep}(\hat{\rho}) \frac{T_e(\hat{\rho}, t)^\delta}{n_e(\hat{\rho}, t)} P_i(t), \tag{2.26}$$

where $i = [1, 2, \ldots, n_{nbi}]$, $k_{nbi_i}^{prof}(\hat{\rho})$ is a normalizing profile, $j_{nbi_i}^{dep}(\hat{\rho})$ is a reference profile for each current-drive source, and the term T_e^δ / n_e represents the current-drive efficiency. For neutral beam current-drive, δ is dependent on the energy of the injected

particles [66]. Note that $j^{dep}_{nbi_i}(\hat{\rho})$ is evaluated at a reference time $t_{r_{nbi}}$, i.e.,

$$j^{dep}_{nbi_i}(\hat{\rho}) = \frac{\langle \bar{j}_i \cdot \bar{B} \rangle}{B_{\phi,0}}(\hat{\rho}, t_{r_{nbi}}) \tag{2.27}$$

The constants $k^{prof}_{nbi_i}(\hat{\rho})$ are expressed as

$$k^{prof}_{nbi_i}(\hat{\rho}) = \frac{n_e(\hat{\rho}, t_{r_{nbi}})}{T_e(\hat{\rho}, t_{r_{nbi}})^{\delta} P_i(t_{r_{nbi}})} \frac{\mathrm{m}^{-3}}{\mathrm{keV} \cdot \mathrm{W}}. \tag{2.28}$$

and are also evaluated at a reference time $t_{r_{nbi}}$.

2.3.4.2 Bootstrap Current Drive

The bootstrap current arises from the inhomogeneity of the magnetic field strength produced by the external coils in the tokamak, which falls of like $1/R$, and is associated with particles in the plasma that cannot complete a helical orbit around the magnetic axis. These particles are therefore called trapped particles [65]. In the presence of density gradients, more trapped particles move in one toroidal direction than in the other, which generates a net current called the bootstrap current [67]. From [68], we write the bootstrap current as

$$\frac{\langle \bar{j}_{bs} \cdot \bar{B} \rangle}{B_{\phi,0}}(\hat{\rho}, t) = \frac{k_{JkeV} R_0}{\hat{F}} \left(\frac{\partial \psi}{\partial \hat{\rho}} \right)^{-1} \left[2\mathcal{L}_{31} T_e \frac{\partial n_e}{\partial \hat{\rho}} + \{ 2\mathcal{L}_{31} + \mathcal{L}_{32} + \alpha \mathcal{L}_{34} \} n_e \frac{\partial T_e}{\partial \hat{\rho}} \right], \tag{2.29}$$

where $\mathcal{L}_{31}$, $\mathcal{L}_{32}$, $\mathcal{L}_{34}$, and α depend on the magnetic configuration of a particular plasma equilibrium and $k_{JkeV} = 1.602 \times 10^{-16}$ J/keV is the conversion factor from keV to J.

2.4 Physics-based Control-oriented Model of Poloidal Magnetic Flux Profile Evolution

The first-principles-driven (FPD), physics-based, control-oriented model of the poloidal magnetic flux profile evolution can be obtained by combining the simplified physics-based models for the electron density (2.8), electron temperature (2.12), plasma resistivity (2.23), and noninductive current-drives (2.25)-(2.29) with the magnetic diffusion equation (MDE from Section 2.2.3) :

$$\frac{\partial \psi}{\partial t} = \frac{\eta(T_e)}{\mu_0 \rho_b^2 \hat{F}^2} \frac{1}{\hat{\rho}} \frac{\partial}{\partial \hat{\rho}} \left(\hat{\rho} D_\psi \frac{\partial \psi}{\partial \hat{\rho}} \right) + R_0 \hat{H} \eta(T_e) \frac{\langle \bar{j}_{ni} \cdot \bar{B} \rangle}{B_{\phi,0}}, \tag{2.30}$$

$$\left. \frac{\partial \psi}{\partial \hat{\rho}} \right|_{\hat{\rho}=0} = 0 \ , \qquad \left. \frac{\partial \psi}{\partial \hat{\rho}} \right|_{\hat{\rho}=1} = -\frac{\mu_0}{2\pi} \frac{R_0}{\hat{G}\Big|_{\hat{\rho}=1} \hat{H}\Big|_{\hat{\rho}=1}} I_p(t). \tag{2.31}$$

Therefore, the goal is to utilize the simplified models for the $T_e(\hat{\rho}, t)$, $n_e(\hat{\rho}, t)$ and $\eta(\hat{\rho}, t)$ to express $\eta(T_e)$ and $\frac{\langle \bar{j}_{ni} \cdot \bar{B} \rangle}{B_{\phi,0}}$ in (2.30) in separation of variables form, in which time and space dependency is separated so that the time functions can be arranged together to form the control inputs for the numerical simulations.

2.4.1 Plasma Resistivity in terms of the Control Inputs

Based on the experimental and TRANSP-predicted T_e profile evolutions in NSTX and NSTX-U, respectively, the constants in the electron temperature model (2.12) in Section 2.3.2 are chosen as $\gamma = \lambda = 1$, $\varepsilon = \nu = 0.5$, $\zeta = \xi = -1$, and $\omega = 1$, which scales the temperature profile in the plasma core and outside of the edge transport barrier in the same way with the plasma parameters [62]. Therefore, the T_e model

(2.12) reduces into

$$T_e(\hat{\rho},t) = k_{T_e}(\hat{\rho})\frac{T_e^{prof}(\hat{\rho})}{n_e(\hat{\rho},t)} I_p(t)\sqrt{P_{tot}(t)}. \tag{2.32}$$

Using the simplified models for the electron temperature and plasma resistivity:

$$n_e(\hat{\rho},t) = n_e^{prof}(\hat{\rho})u_n(t) \tag{2.33}$$

$$\eta(\hat{\rho},t) = \frac{k_{sp}(\hat{\rho})Z_{eff}}{T_e(\hat{\rho},t)^{3/2}}, \tag{2.34}$$

Substitute (2.32) and (2.33) into (2.34) to express $\eta(T_e)$ in separation of variables form

$$\eta(\hat{\rho},t) = \frac{k_{sp}(\hat{\rho})Z_{eff}}{k_{T_e}(\hat{\rho})^{3/2}T_e^{prof}(\hat{\rho})^{3/2}\dfrac{I_p(t)^{3/2}P_{tot}(t)^{3/4}}{n_e^{prof}(\hat{\rho})^{3/2}u_n(t)^{3/2}}}$$

$$= \frac{k_{sp}(\hat{\rho})Z_{eff}n_e^{prof}(\hat{\rho})^{3/2}u_n(t)^{3/2}}{k_{T_e}(\hat{\rho})^{3/2}T_e^{prof}(\hat{\rho})^{3/2}I_p(t)^{3/2}P_{tot}(t)^{3/4}}$$

$$\eta(T_e) = \underbrace{\frac{k_{sp}(\hat{\rho})Z_{eff}n_e^{prof}(\hat{\rho})^{3/2}}{k_{T_e}(\hat{\rho})^{3/2}T_e^{prof}(\hat{\rho})^{3/2}}}_{f_\eta(\hat{\rho})} \times \underbrace{\frac{u_n(t)^{3/2}}{I_p(t)^{3/2}P_{tot}(t)^{3/4}}}_{u_\eta(t)}, \tag{2.35}$$

where $u_\eta(t)$ is a nonlinear combination of the physical actuators. Hence, it can be interpreted as a control input for the numerical simulations.

2.4.2 Non-inductive Current-Drive in terms of the Control Inputs

Total non-inductive current-drive is produced by neutral beam injection and bootstrap current in both NSTX and NSTX-U. The auxiliary heating and current drive actuators are 3 individual neutral beam injectors (NBI) for NSTX, and 6 NBIs for NSTX-U. Therefore, the constant in the neutral beam current-drive model (2.26) is set to $\delta = 1/2$ [66]. Substituting the simplified model for the neutral beam current density (2.26) and the bootstrap current (2.29) into (2.25), the physics-based model for the total non-inductive current drive can be written as follows

$$\begin{aligned}\frac{\langle \bar{j}_{ni} \cdot \bar{B} \rangle}{B_{\phi,0}} &= \sum_{i=1}^{n_{nbi}} \frac{\langle \bar{j}_i \cdot \bar{B} \rangle}{B_{\phi,0}} + \frac{\langle \bar{j}_{bs} \cdot \bar{B} \rangle}{B_{\phi,0}} \\ &= \sum_{i=1}^{n_{nbi}} k_{nbi_i}^{prof}(\hat{\rho}) j_{nbi_i}^{dep}(\hat{\rho}) \frac{\sqrt{T_e(\hat{\rho},t)}}{n_e(\hat{\rho},t)} P_i(t) \\ &\quad + \frac{k_{JeV} R_0}{\hat{F}(\hat{\rho})} \left(\frac{\partial \psi}{\partial \hat{\rho}}\right)^{-1} \left[2\mathcal{L}_{31} T_e \frac{\partial n_e}{\partial \hat{\rho}} + \{2\mathcal{L}_{31} + \mathcal{L}_{32} + \alpha \mathcal{L}_{34}\} n_e \frac{\partial T_e}{\partial \hat{\rho}} \right] \end{aligned} \tag{2.36}$$

Substitute (2.33) and (2.32) into (2.36) to obtain $\frac{\sqrt{T_e(\hat{\rho},t)}}{n_e(\hat{\rho},t)}$, $T_e \frac{\partial n_e}{\partial \hat{\rho}}$ and $n_e \frac{\partial T_e}{\partial \hat{\rho}}$ in terms of the control inputs:

$$\begin{aligned}\frac{\sqrt{T_e(\hat{\rho},t)}}{n_e(\hat{\rho},t)} &= \frac{k_{T_e}(\hat{\rho})^{1/2} \dfrac{T_e^{prof}(\hat{\rho})^{1/2}}{n_e(\hat{\rho},t)^{1/2}} I_p(t)^{1/2} P_{tot}(t)^{1/4}}{n_e(\hat{\rho},t)} \\ &= \frac{k_{T_e}(\hat{\rho})^{1/2} T_e^{prof}(\hat{\rho})^{1/2} I_p(t)^{1/2} P_{tot}(t)^{1/4}}{n_e^{prof}(\hat{\rho})^{3/2} u_n(t)^{3/2}} \end{aligned} \tag{2.37}$$

$$\frac{\sqrt{T_e(\hat{\rho},t)}}{n_e(\hat{\rho},t)} = \frac{k_{T_e}(\hat{\rho})^{1/2} T_e^{prof}(\hat{\rho})^{1/2}}{n_e^{prof}(\hat{\rho})^{3/2}} \times \frac{I_p(t)^{1/2} P_{tot}(t)^{1/4}}{u_n(t)^{3/2}} \tag{2.38}$$

similarly,

$$T_e\frac{\partial n_e}{\partial \hat{\rho}} = k_{T_e}(\hat{\rho})\frac{T_e^{prof}(\hat{\rho})}{n_e^{prof}(\hat{\rho})u_n(t)}I_p(t)\sqrt{P_{tot}(t)}\frac{dn_e^{prof}(\hat{\rho})}{d\hat{\rho}}u_n(t)$$

$$T_e\frac{\partial n_e}{\partial \hat{\rho}} = \frac{k_{T_e}(\hat{\rho})T_e^{prof}(\hat{\rho})}{n_e^{prof}(\hat{\rho})}\frac{dn_e^{prof}(\hat{\rho})}{d\hat{\rho}} \times I_p(t)\sqrt{P_{tot}(t)} \tag{2.39}$$

and

$$n_e\frac{\partial T_e}{\partial \hat{\rho}} = n_e^{prof}(\hat{\rho})u_n(t)\frac{d}{d\hat{\rho}}\left[\frac{k_{T_e}(\hat{\rho})T_e^{prof}(\hat{\rho})}{n_e^{prof}(\hat{\rho})}\right]\frac{I_p(t)\sqrt{P_{tot}(t)}}{u_n(t)}$$

$$n_e\frac{\partial T_e}{\partial \hat{\rho}} = n_e^{prof}(\hat{\rho})\frac{d}{d\hat{\rho}}\left[\frac{k_{T_e}(\hat{\rho})T_e^{prof}(\hat{\rho})}{n_e^{prof}(\hat{\rho})}\right] \times I_p(t)\sqrt{P_{tot}(t)} \tag{2.40}$$

Now, substitute (2.38), (2.39) and (2.40) into (2.36) to rewrite the non-inductive current-drive in separation of variables form as follows

$$\frac{\langle \bar{j}_{ni}\cdot\bar{B}\rangle}{B_{\phi,0}} = \sum_{i=1}^{n_{nbi}}\left[k_{nbi_i}^{prof}(\hat{\rho})j_{nbi_i}^{dep}(\hat{\rho})\frac{k_{T_e}(\hat{\rho})^{1/2}T_e^{prof}(\hat{\rho})^{1/2}}{n_e^{prof}(\hat{\rho})^{3/2}}\right] \times \frac{I_p(t)^{1/2}P_{tot}(t)^{1/4}}{u_n(t)^{3/2}}P_i(t)$$

$$+\frac{k_{JeV}R_0}{\hat{F}(\hat{\rho})}\left(\frac{\partial\psi}{\partial\hat{\rho}}\right)^{-1}\Bigg[2\mathcal{L}_{31}\frac{k_{T_e}(\hat{\rho})T_e^{prof}(\hat{\rho})}{n_e^{prof}(\hat{\rho})}\frac{dn_e^{prof}(\hat{\rho})}{d\hat{\rho}} \ .....$$

$$+\left\{2\mathcal{L}_{31}+\mathcal{L}_{32}+\alpha\mathcal{L}_{34}\right\}n_e^{prof}(\hat{\rho})\frac{d}{d\hat{\rho}}\left\{\frac{k_{T_e}(\hat{\rho})T_e^{prof}(\hat{\rho})}{n_e^{prof}(\hat{\rho})}\right\}\Bigg] \times I_p(t)\sqrt{P_{tot}(t)}, \tag{2.41}$$

where the time functions represent additional control inputs for the FPD model.

2.4.3 Magnetic Diffusion Equation in Control-Oriented Form

Equations (2.35) and (2.41) allow us to rewrite the magnetic diffusion equation (2.30)-(2.31) in terms of the control inputs as

$$\frac{\partial \psi}{\partial t} = f_\eta(\hat{\rho}) u_\eta(t) \frac{1}{\hat{\rho}} \frac{\partial}{\partial \hat{\rho}} \left(\hat{\rho} D_\psi(\hat{\rho}) \frac{\partial \psi}{\partial \hat{\rho}} \right) + \sum_{i=1}^{6} f_i(\hat{\rho}) u_i(t) + f_{bs}(\hat{\rho}) u_{bs}(t) \left(\frac{\partial \psi}{\partial \hat{\rho}} \right)^{-1}, \quad (2.42)$$

$$\left. \frac{\partial \psi}{\partial \hat{\rho}} \right|_{\hat{\rho}=0} = 0 \ , \qquad \left. \frac{\partial \psi}{\partial \hat{\rho}} \right|_{\hat{\rho}=1} = -f_b I_p(t), \quad (2.43)$$

where the time functions on the RHS of (2.42)-(2.43) can be defined as control inputs, which are nonlinear combinations of the physical actuators as

$$u_\eta(t) = \frac{u_n(t)^{3/2}}{I_p(t)^{3/2} P_{tot}(t)^{3/4}}, \quad (2.44)$$

$$u_i(t) = \frac{P_i(t)}{I_p(t) \sqrt{P_{tot}(t)}}, \quad (i = 1, 2, ..., n_{nbi}) \quad (2.45)$$

$$u_{bs}(t) = \frac{u_n(t)^{3/2}}{I_p(t)^{1/2} P_{tot}(t)^{1/4}}, \quad (2.46)$$

and the spatial functions appearing on the RHS of (2.42)-(2.43) can be expressed in terms of the various model profiles and constants as

$$f_\eta(\hat{\rho}) = \frac{k_{sp}(\hat{\rho}) Z_{eff} n_e^{prof}(\hat{\rho})^{3/2}}{\mu_0 \rho_b^2 \hat{F}(\hat{\rho})^2 k_{T_e}(\hat{\rho})^{3/2} T_e^{prof}(\hat{\rho})^{3/2}} \quad (2.47)$$

$$f_i(\hat{\rho}) = R_0 \hat{H}(\hat{\rho}) k_{nbi_i}^{prof}(\hat{\rho}) j_{nbi_i}^{dep}(\hat{\rho}) \frac{k_{T_e}(\hat{\rho})^{1/2} T_e^{prof}(\hat{\rho})^{1/2}}{n_e^{prof}(\hat{\rho})^{3/2}} \quad (i = 1, 2, ..., n_{nbi}) \quad (2.48)$$

$$f_{bs}(\hat{\rho}) = R_0 \hat{H}(\hat{\rho}) \frac{k_{JeV} R_0}{\hat{F}(\hat{\rho})} \Bigg[2\mathcal{L}_{31} \frac{dn_e^{prof}(\hat{\rho})}{d\hat{\rho}} \frac{k_{sp}(\hat{\rho}) Z_{eff} n_e^{prof}(\hat{\rho})^{1/2}}{k_{T_e}(\hat{\rho})^{1/2} T_e^{prof}(\hat{\rho})^{1/2}} \; ....$$

$$+ \left\{ 2\mathcal{L}_{31} + \mathcal{L}_{32} + \alpha \mathcal{L}_{34} \right\} \frac{d}{d\hat{\rho}} \left\{ \frac{k_{T_e}(\hat{\rho}) T_e^{prof}(\hat{\rho})}{n_e^{prof}(\hat{\rho})} \right\} \frac{k_{sp}(\hat{\rho}) Z_{eff} n_e^{prof}(\hat{\rho})^{5/2}}{k_{T_e}(\hat{\rho})^{3/2} T_e^{prof}(\hat{\rho})^{3/2}} \Bigg] \quad (2.49)$$

$$D_{\psi}(\hat{\rho}) = \hat{F}(\hat{\rho}) \hat{G}(\hat{\rho}) \hat{H}(\hat{\rho}) \quad (2.50)$$

$$f_b = \frac{\mu_0}{2\pi} \frac{R_0}{\hat{G}\Big|_{\hat{\rho}=1} \hat{H}\Big|_{\hat{\rho}=1}} \quad (2.51)$$

Note from (2.42) and (2.43) that, the magnetic diffusion equation admits actuation not only through interior (u_i and u_{bs}) and boundary (I_p) controls, but also through u_η, which is considered as diffusivity control in this work. TRANSP simulated and/or experimental data can now be utilized to identify the model reference profiles and various constants in the simplified physics-based models (2.8)-(2.29) to tailor the FPD model (2.42)-(2.43) to a scenario of interest in NSTX and NSTX-U.

2.5 Model Tailored for the NSTX

2.5.1 Reference Run 133964Z01

2.5.1.1 Identification of Reference Profiles and Constants

The reference run 133964D02 is used to benchmark the q-profile predictions of the FPD model. This specific run has MSE [69] constrained reconstruction input to TRANSP, hence is reliable for the purposes of this work. Note that run "133964Z01" is

analyzed in this section, which is a rerun of the original run "133964D02" in TRANSP with the new capability added in 2010. This way, it is possible to view power and current separately for each individual beam line.

Note also that there are 3 individual neutral beam injectors in NSTX, therefore, $n_{nbi} = 3$ in (2.25). The geometric factors related to the magnetic configuration of the plasma equilibrium and the reference and normalizing profiles for the various models are shown in Fig. 2.3. Neutral beam deposition constants and the corresponding reference current density profiles are shown in Fig. 2.4 for each of the 3 neutral beam lines.

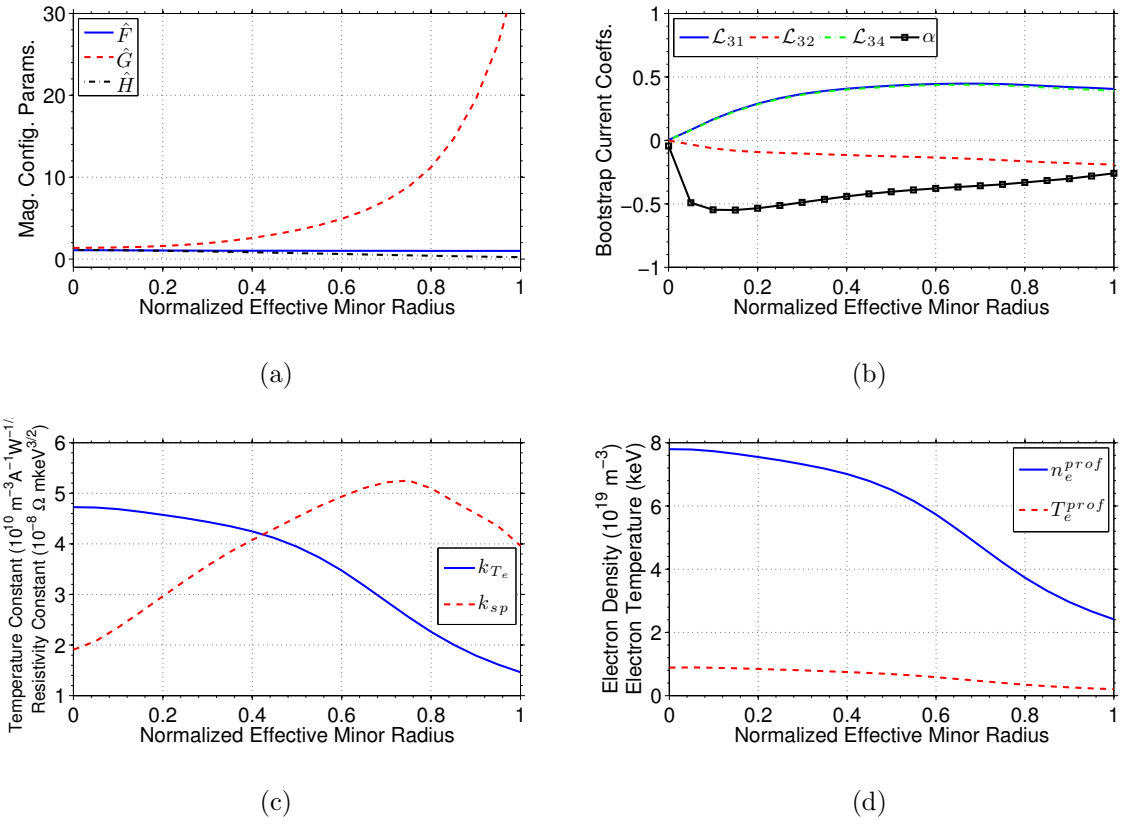

Figure 2.3: Model parameters tailored to NSTX: (a) magnetic equilibrium configuration parameters $\hat{F}(\hat{\rho})$, $\hat{G}(\hat{\rho})$, and $\hat{H}(\hat{\rho})$, (b) bootstrap current coefficients $\mathcal{L}_{31}(\hat{\rho})$, $\mathcal{L}_{32}(\hat{\rho})$, $\mathcal{L}_{34}(\hat{\rho})$ and $\alpha(\hat{\rho})$, (c) electron temperature coefficient k_{T_e} and plasma resistivity coefficient k_{sp}, (d) reference electron density profile, $n_e^{prof}(\hat{\rho})$ and reference electron temperature profile, $T_e^{prof}(\hat{\rho})$.

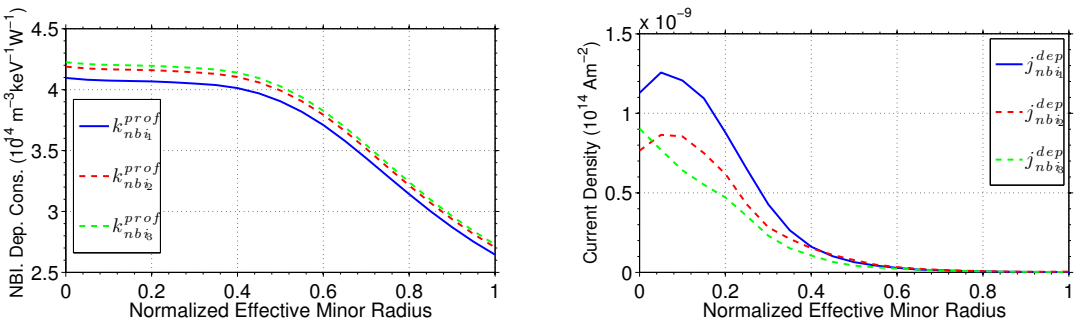

(a) (b)

Figure 2.4: (a) Neutral beam model coefficients: $k^{prof}_{nbi_1}(\hat{\rho})$, $k^{prof}_{nbi_2}(\hat{\rho})$, $k^{prof}_{nbi_3}(\hat{\rho})$ for the individual beam lines and (b) reference neutral beam current deposition profiles: $j^{dep}_{nbi_1}(\hat{\rho})$, $j^{dep}_{nbi_2}(\hat{\rho})$, $j^{dep}_{nbi_3}(\hat{\rho})$ for the individual beam lines.

2.5.1.2 Qualitative Agreement of Various Plasma Profiles in between the FPD Model and TRANSP Output

The evolution of the plasma parameters predicted by the FPD model is compared with the TRANSP-simulated plasma parameters in NSTX run 133964Z01. The physical inputs (total plasma current, power of the neutral beam lines and electron density regulation) applied during the simulation are shown in Fig. 2.5. TRANSP outputs for the electron density and temperature profiles are compared with the FPD model predictions at different times in Fig. 2.6. Fig. 2.7 shows the TRANSP-simulated and FPD model-predicted neutral beam and bootstrap current density profiles. Finally, evolution of the poloidal flux (ψ) as obtained from TRANSP and predicted by FPD model are compared at different time instants and at various spatial locations in the plasma in Figs. 2.8 and 2.9, respectively. Similar analysis is provided for the safety factor (q-profile) in Figs. 2.10 and 2.11.

As can be seen from Figs. 2.6-2.11, predictions by the FPD control-oriented model show reasonable agreement with TRANSP simulations for the purpose of control design.

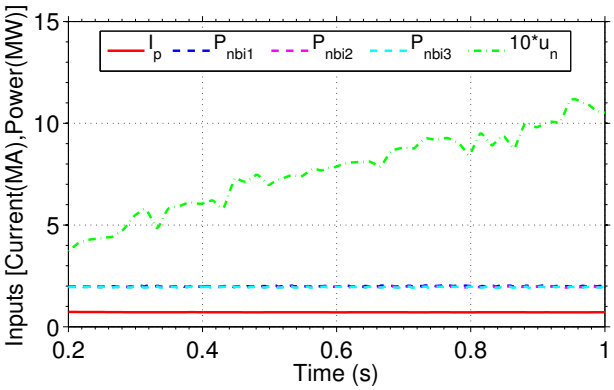

Figure 2.5: Physical inputs applied during the FPD model simulation (current in MA, power in MW, and u_n is dimensionless).

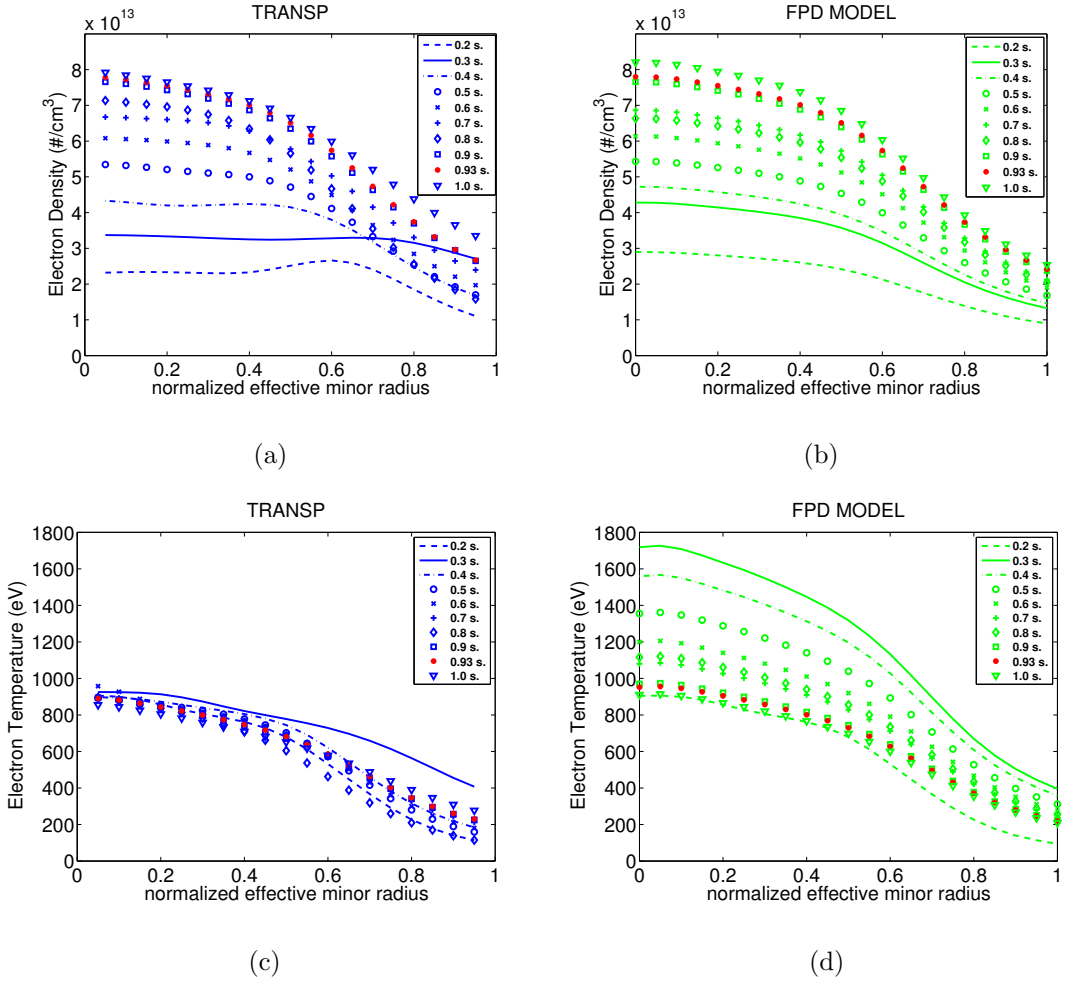

Figure 2.6: Comparison of the T_e and n_e profiles: TRANSP [(a),(c)], FPD model [(b),(d)] Note: Red dots correspond to the profile at the model reference time, t_r

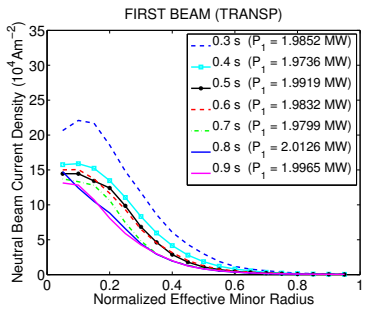

(a) 1^{st} Beamline (TRANSP)

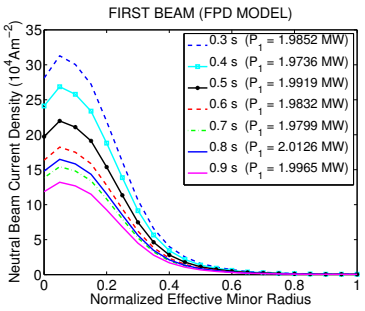

(b) 1^{st} Beamline (FPD Model)

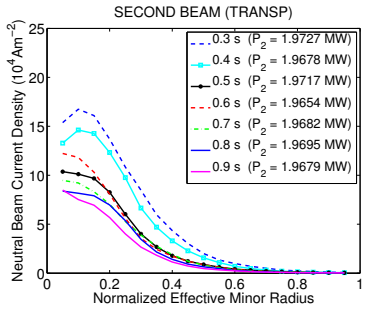

(c) 2^{nd} Beamline (TRANSP)

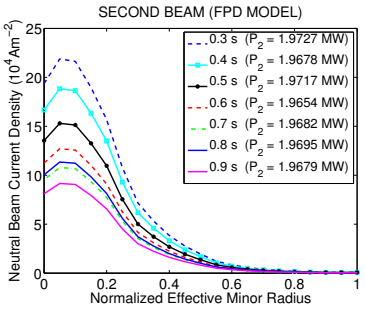

(d) 2^{nd} Beamline (FPD Model)

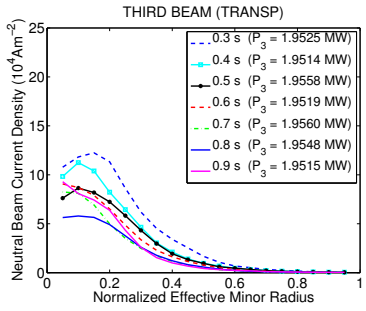

(e) 3^{rd} Beamline (TRANSP)

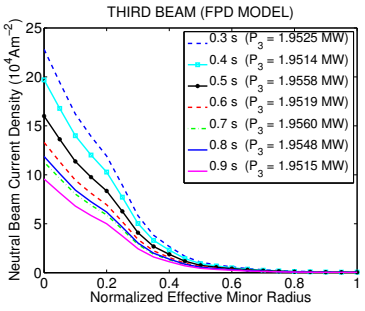

(f) 3^{rd} Beamline (FPD Model)

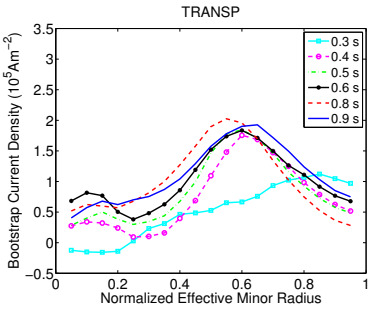

(g) Bootstrap (TRANSP)

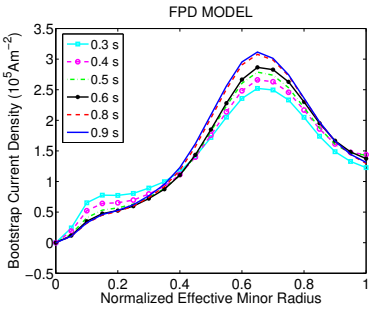

(h) Bootstrap (FPD Model)

Figure 2.7: Neutral beam current density profile comparisons: TRANSP [(a),(c),(e)] and FPD model [(b),(d),(f)]. Bootstrap current density profile comparisons: TRANSP (g) and FPD model (h).

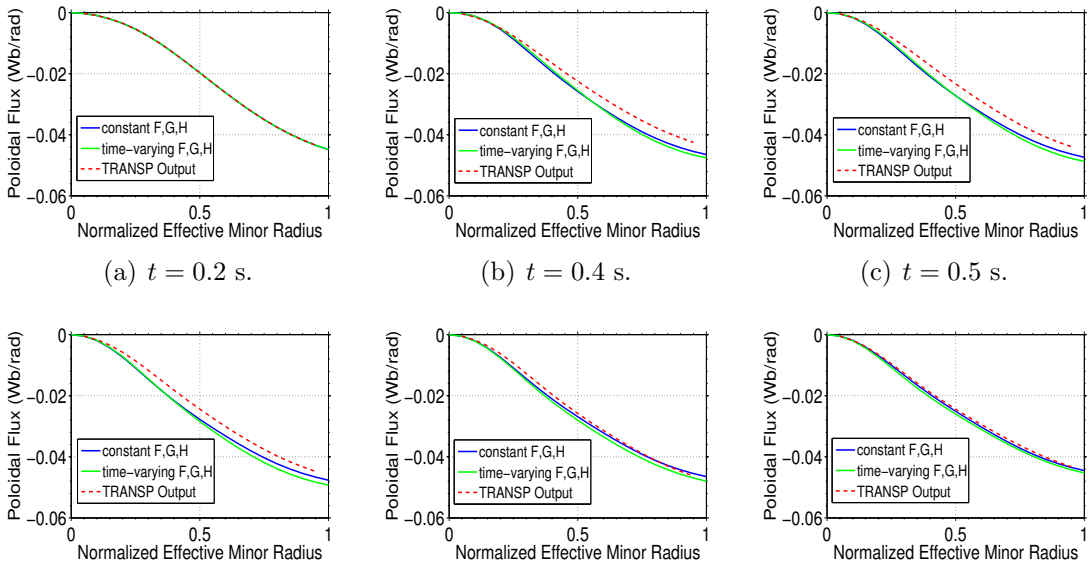

(a) $t = 0.2$ s. (b) $t = 0.4$ s. (c) $t = 0.5$ s.

(d) $t = 0.6$ s. (e) $t = 0.8$ s. (f) $t = 1.0$ s.

Figure 2.8: Poloidal flux profile $\psi(\hat{\rho})$ at various time instants. Note: Solid green lines correspond to the FPD model with time-varying magnetic geometry.

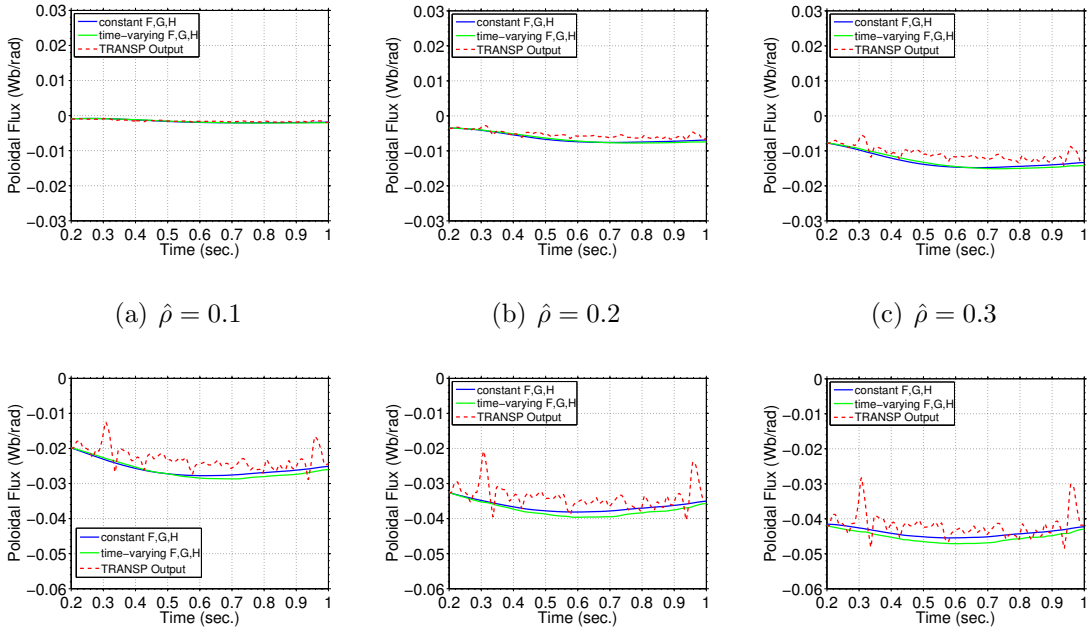

(a) $\hat{\rho} = 0.1$ (b) $\hat{\rho} = 0.2$ (c) $\hat{\rho} = 0.3$

(d) $\hat{\rho} = 0.5$ (e) $\hat{\rho} = 0.7$ (f) $\hat{\rho} = 0.9$

Figure 2.9: Time trace of poloidal flux $\psi(t)$ at various spatial locations. Note: Solid green lines correspond to the FPD model with time-varying magnetic geometry.

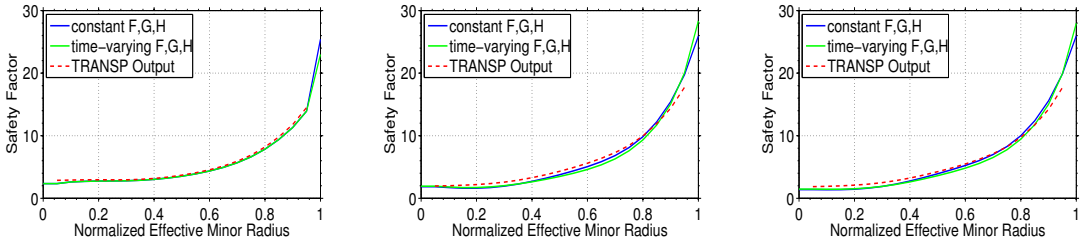

(a) $t = 0.2$ s. (b) $t = 0.4$ s. (c) $t = 0.5$ s.

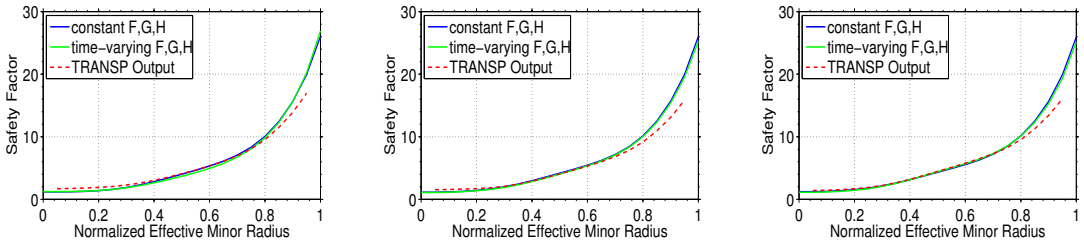

(d) $t = 0.6$ s. (e) $t = 0.8$ s. (f) $t = 1.0$ s.

Figure 2.10: Safety factor profile $q(\hat{\rho})$ at various time instants. Note: Solid green lines correspond to the FPD model with time-varying magnetic geometry.

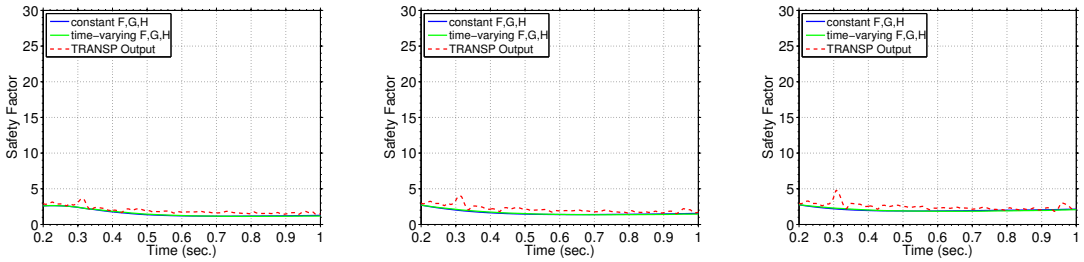

(a) $\hat{\rho} = 0.1$ (b) $\hat{\rho} = 0.2$ (c) $\hat{\rho} = 0.3$

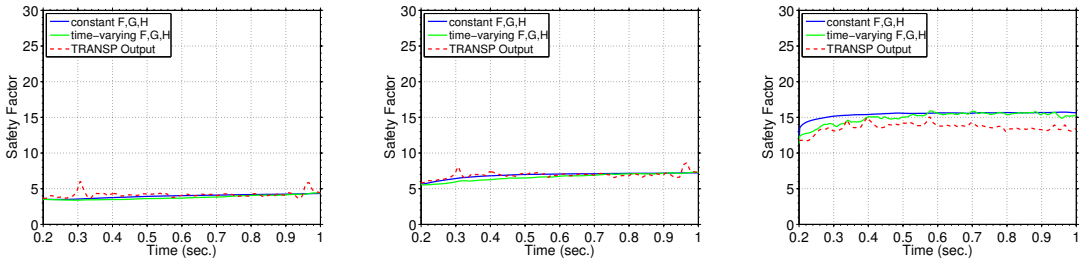

(d) $\hat{\rho} = 0.5$ (e) $\hat{\rho} = 0.7$ (f) $\hat{\rho} = 0.9$

Figure 2.11: Time trace of safety factor $q(t)$ at various spatial locations. Note: Solid green lines correspond to the FPD model with time-varying magnetic geometry.

2.6 Model Tailored for the NSTX-U

2.6.1 Reference Run 142301M21

2.6.1.1 Identification of Reference Profiles and Constants

The reference run 142301M21 is used to benchmark the q-profile predictions of the FPD model. NSTX-U run 142301M21 is a TRANSP run with the NSTX-U shape and actuators, using the scaled profiles from NSTX.

Note that for this case study, the power and current of the individual auxiliary H&CD actuators on NSTX-U, which are the 6 neutral beam launchers, are added to provide a total neutral beam power and a total neutral beam current density profile for simplicity, i.e., $n_{nbi} = 1$ in (2.25). The geometric factors related to the magnetic configuration of the plasma equilibrium and the reference and normalizing profiles for the various models are shown in Figs. 2.12-2.13. The neutral beam model coefficient and the corresponding reference neutral beam current density profile are shown in Fig. 2.14 for the combined neutral beam lines.

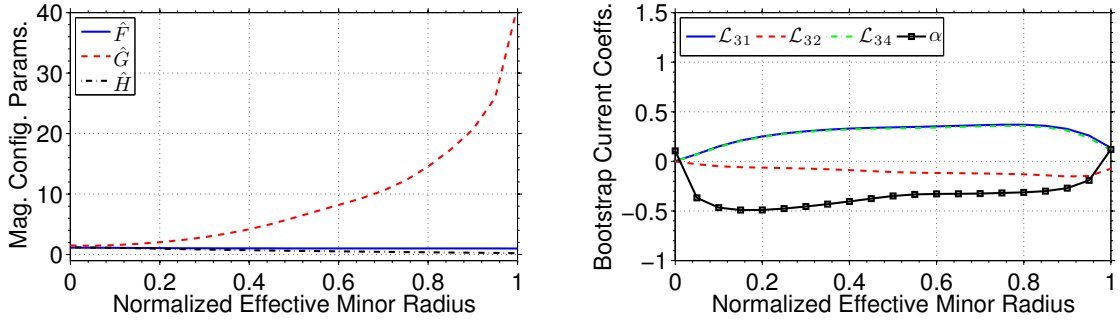

(a) (b)

Figure 2.12: Model parameters tailored to NSTX-U run 142301M21: (a) magnetic equilibrium configuration parameters $\hat{F}(\hat{\rho})$, $\hat{G}(\hat{\rho})$, and $\hat{H}(\hat{\rho})$, (b) bootstrap current coefficients $\mathcal{L}_{31}(\hat{\rho})$, $\mathcal{L}_{32}(\hat{\rho})$, $\mathcal{L}_{34}(\hat{\rho})$ and $\alpha(\hat{\rho})$.

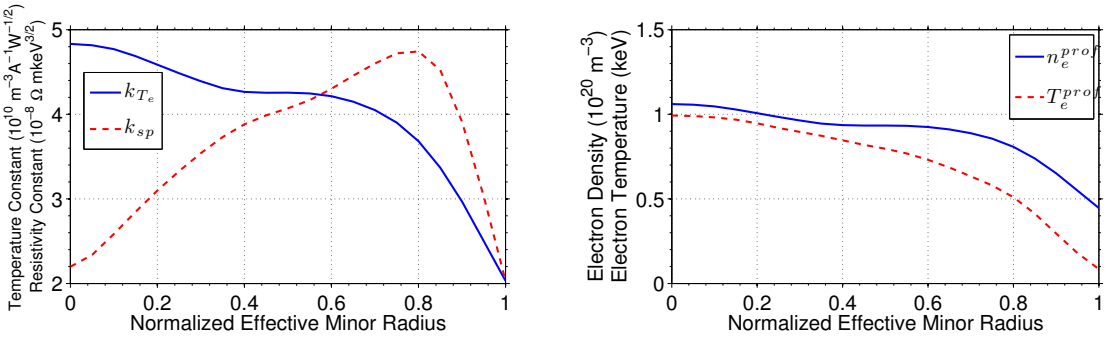

Figure 2.13: Model parameters tailored to NSTX-U run 142301M21: (a) electron temperature coefficient k_{T_e} and plasma resistivity coefficient k_{sp}, (b) reference electron density profile, $n_e^{prof}(\hat{\rho})$ and reference electron temperature profile, $T_e^{prof}(\hat{\rho})$.

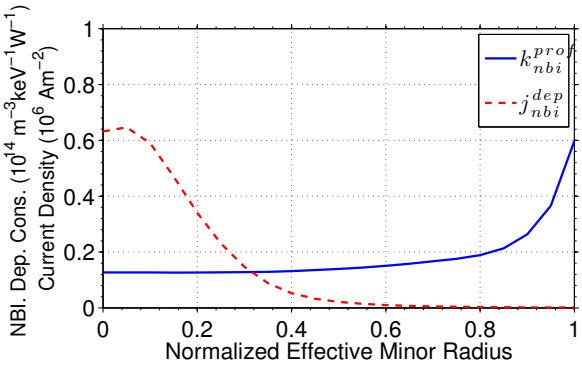

Figure 2.14: Neutral beam model coefficient, $k_{nbi}^{prof}(\hat{\rho})$, and reference neutral beam current density profile, $j_{nbi}^{dep}(\hat{\rho})$ for the combined neutral beam lines for NSTX-U run 142301M21.

2.6.1.2 Qualitative Agreement of Various Plasma Profiles in between the FPD Model and TRANSP Output

The evolution of the plasma parameters predicted by the FPD model is compared with the TRANSP-simulated plasma parameters in NSTX-U run 142301M21. The physical inputs (total plasma current, power of the neutral beam lines and electron density regulation) applied during the simulation are shown in Fig. 2.15. TRANSP outputs

for the electron density and temperature profiles are compared with the FPD model predictions at different times in Fig. 2.16. Fig. 2.17 shows the TRANSP-simulated and FPD model-predicted neutral beam and bootstrap current density profiles.

Finally, evolution of the poloidal flux (ψ) as obtained from TRANSP and predicted by FPD model are compared at different time instants and at various spatial locations in the plasma in Figs. 2.18 and 2.19, respectively. Similarly, evolution of the safety factor (q) profiles, as obtained from TRANSP and predicted by FPD model are compared at different time instants and at various spatial locations within the plasma in Figs. 2.20 and 2.21, respectively.

As can be seen from Figs. 2.16-2.21, predictions by the FPD control-oriented model show reasonable agreement with TRANSP simulations for the purpose of control design.

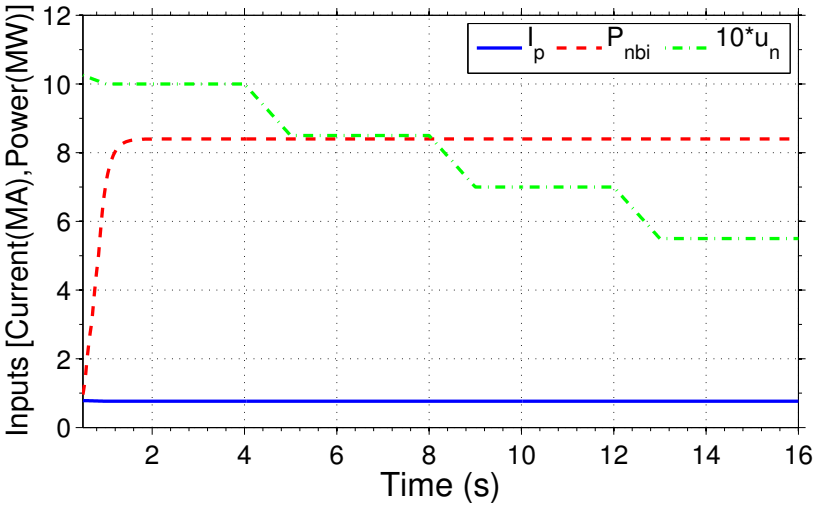

Figure 2.15: Physical inputs applied during the FPD model simulation (current in MA, power in MW, and u_n is dimensionless).

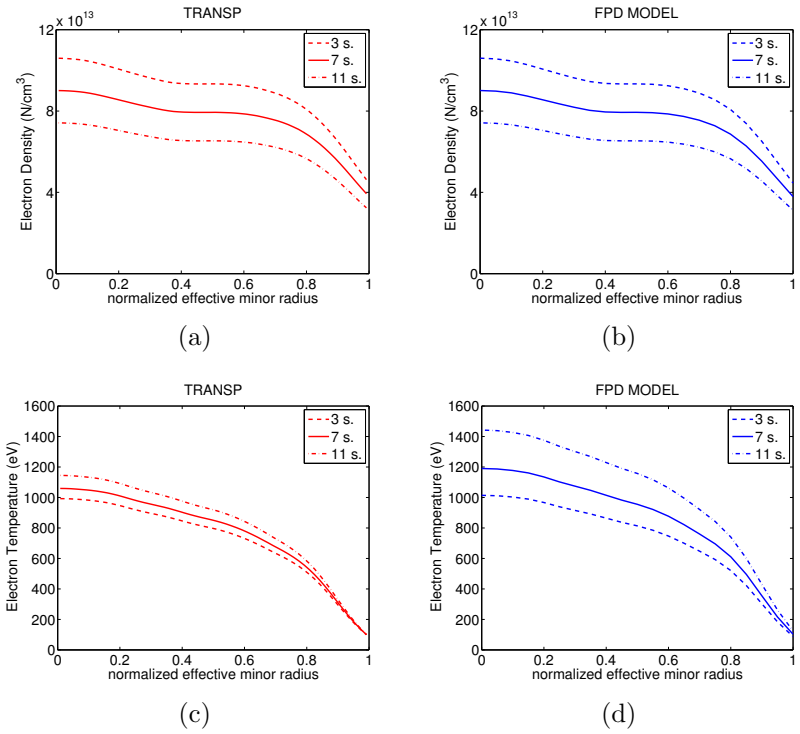

Figure 2.16: Comparison of the T_e and n_e profiles: TRANSP [(a),(c)], FPD model [(b),(d)]

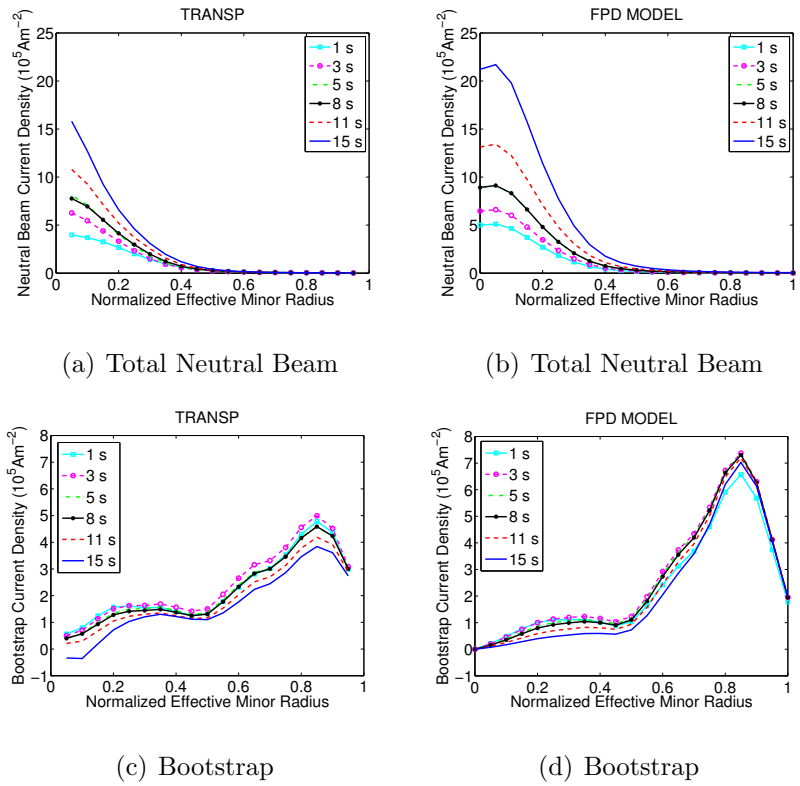

Figure 2.17: Noninductive current density profile evolution comparison: TRANSP [(a),(c)], control-oriented model [(b),(d)].

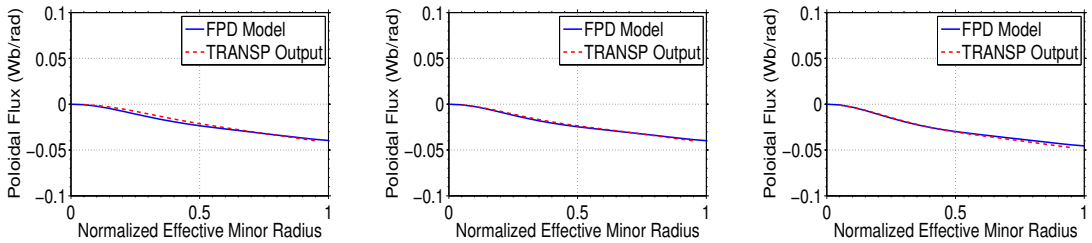

(a) $t = 1$ s. (b) $t = 3$ s. (c) $t = 6$ s.

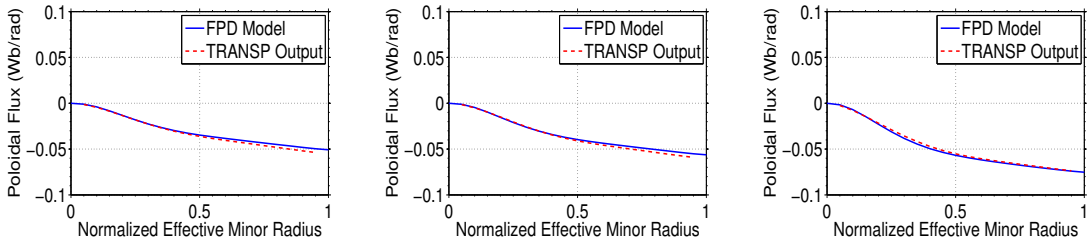

(d) $t = 9$ s. (e) $t = 12$ s. (f) $t = 15$ s.

Figure 2.18: Poloidal flux profile $\psi(\hat{\rho})$ at various time instants. Note: FPD model (solid) and TRANSP output (dash) in each subfigure.

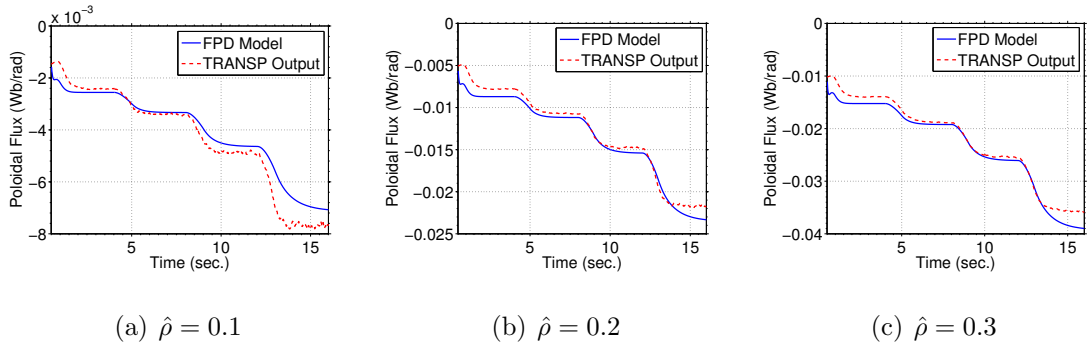

(a) $\hat{\rho} = 0.1$ (b) $\hat{\rho} = 0.2$ (c) $\hat{\rho} = 0.3$

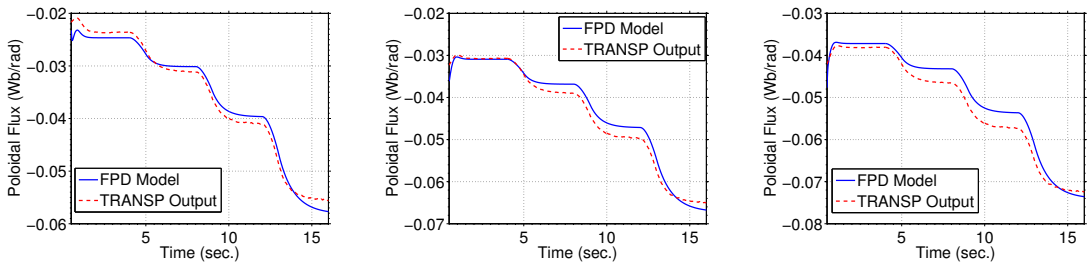

(d) $\hat{\rho} = 0.5$ (e) $\hat{\rho} = 0.7$ (f) $\hat{\rho} = 0.9$

Figure 2.19: Time trace of poloidal flux $\psi(t)$ at various spatial locations. Note: FPD model (solid) and TRANSP output (dash) in each subfigure.

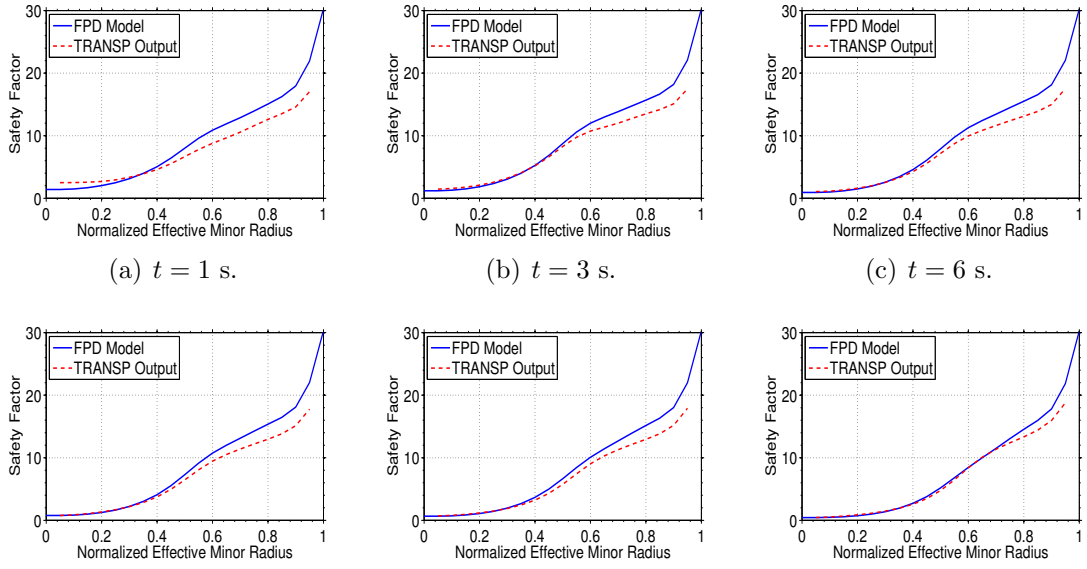

(a) $t = 1$ s. (b) $t = 3$ s. (c) $t = 6$ s.

(d) $t = 9$ s. (e) $t = 12$ s. (f) $t = 15$ s.

Figure 2.20: Safety factor profile $q(\hat{\rho})$ at various time instants. Note: FPD model (solid) and TRANSP output (dash) in each subfigure.

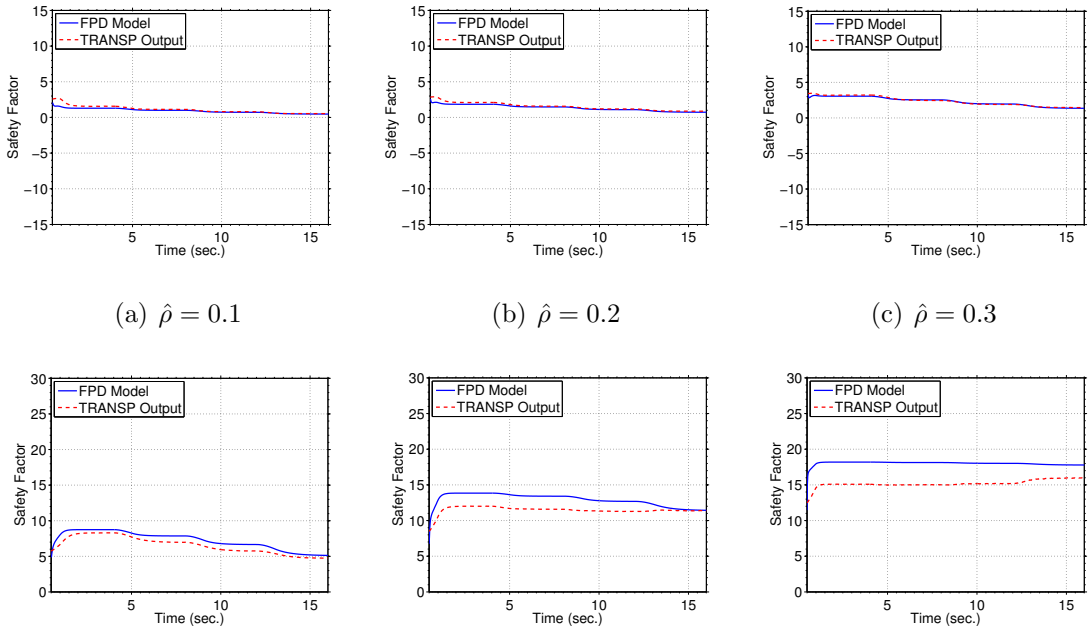

(a) $\hat{\rho} = 0.1$ (b) $\hat{\rho} = 0.2$ (c) $\hat{\rho} = 0.3$

(d) $\hat{\rho} = 0.5$ (e) $\hat{\rho} = 0.7$ (f) $\hat{\rho} = 0.9$

Figure 2.21: Time trace of safety factor $q(t)$ at various spatial locations. Note: FPD model (solid) and TRANSP output (dash) in each subfigure.

2.6.2 Reference Run 121123Z42

2.6.2.1 Identification of Reference Profiles and Constants

The reference run 121123Z42 is a rerun of the original run 121123R42 in TRANSP with the new capability so as to view power and current separately for each individual beam line. NSTX-U run 121123Z42 is still a TRANSP run with the NSTX-U shape and actuators, using the scaled profiles from NSTX.

Note that for this case study, the power and current of the individual auxiliary H&CD actuators on NSTX-U, which are the 6 neutral beam launchers, are modeled separately, i.e., $n_{nbi} = 6$ in (2.25). The geometric factors related to the magnetic configuration of the plasma equilibrium and bootstrap current coefficients are shown in Fig. 2.22. Reference electron density and temperature profiles are depicted in Fig. 2.23-(a). On the other hand, reference neutral beam current density profiles are shown in Fig. 2.23-(b).

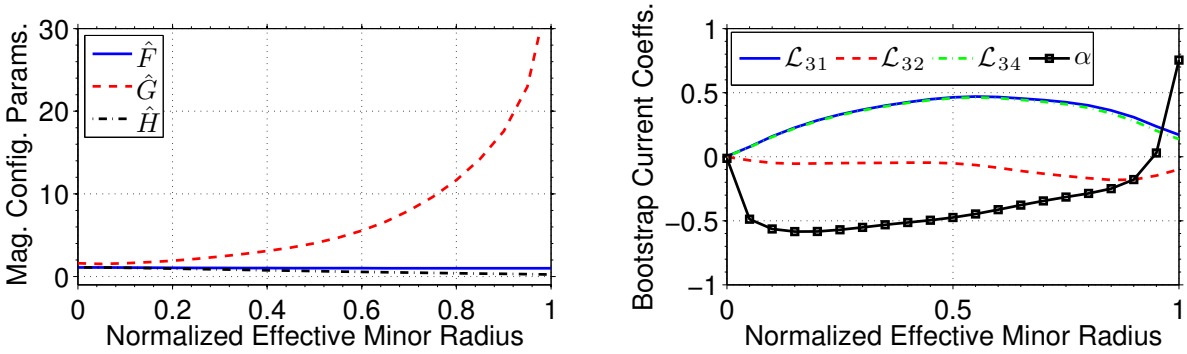

(a) (b)

Figure 2.22: Model parameters tailored to NSTX-U run 121123Z42: (a) magnetic equilibrium configuration parameters $\hat{F}(\hat{\rho})$, $\hat{G}(\hat{\rho})$, and $\hat{H}(\hat{\rho})$, (b) bootstrap current coefficients $\mathcal{L}_{31}(\hat{\rho})$, $\mathcal{L}_{32}(\hat{\rho})$, $\mathcal{L}_{34}(\hat{\rho})$ and $\alpha(\hat{\rho})$.

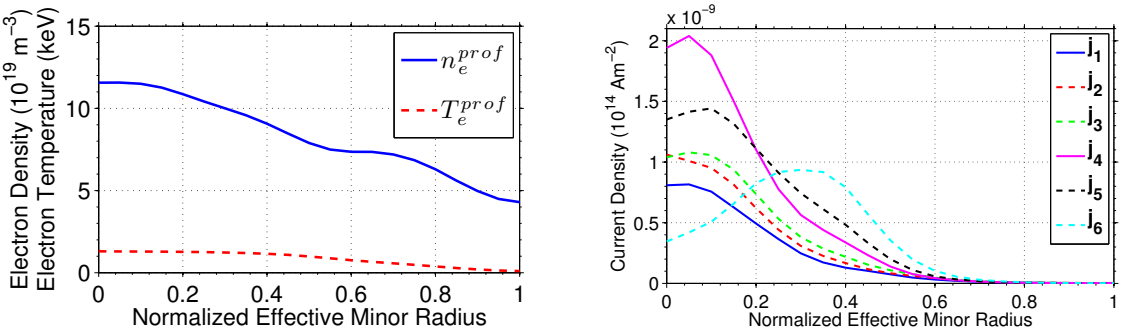

(a) (b)

Figure 2.23: Model parameters tailored to NSTX-U run 121123Z42: (a) reference electron density profile, $n_e^{prof}(\hat{\rho})$, and reference electron temperature profile, $T_e^{prof}(\hat{\rho})$. (b) Reference neutral beam current density profiles.

2.6.2.2 Qualitative Agreement of Various Plasma Profiles in between the FPD Model and TRANSP Output

The physical inputs applied during the simulation are shown in Fig. 2.24. Evolutions of the poloidal flux (ψ) and safety factor (q) profiles as obtained from TRANSP and predicted by FPD model are compared at different time instants in Figs. 2.25 and 2.26, respectively. Figs. 2.25 and 2.26 show reasonable agreement between predictions by the FPD control-oriented model and TRANSP simulations.

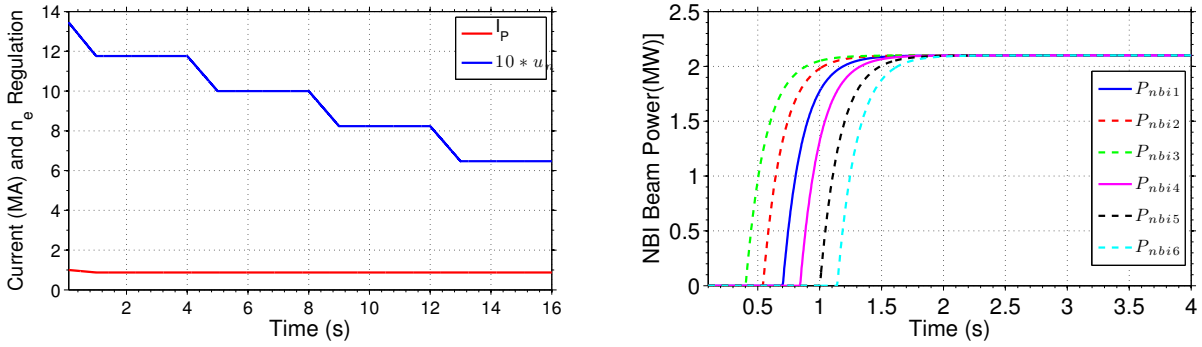

(a) (b)

Figure 2.24: Physical inputs applied during the FPD model simulation: (a) Total plasma current in MA, and electron density regulation, u_n. (b) Powers of the individual neutral beam injectors (constant after 4 s. until 16 s.).

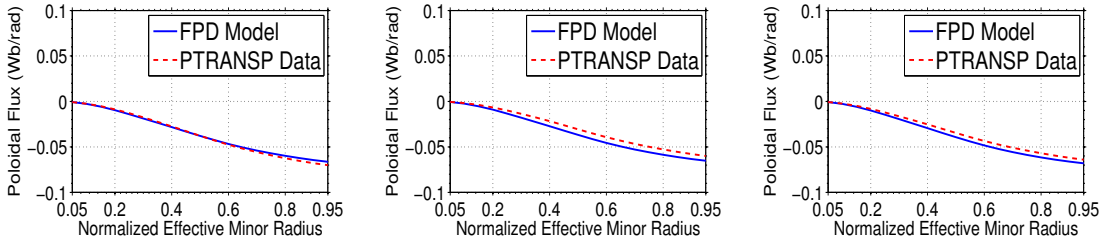

(a) $t = 1$ s. (b) $t = 3$ s. (c) $t = 6$ s.

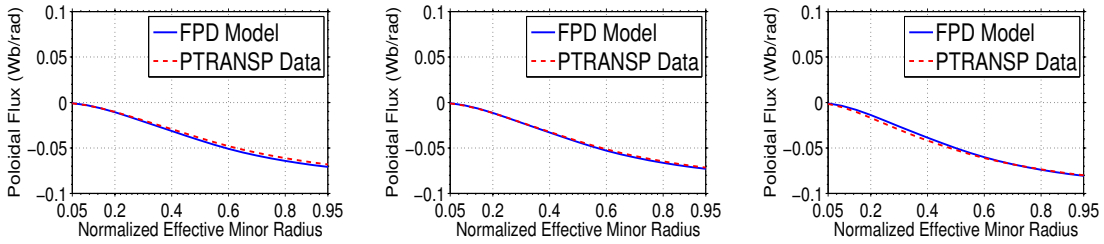

(d) $t = 9$ s. (e) $t = 12$ s. (f) $t = 15$ s.

Figure 2.25: Poloidal flux profile $\psi(\hat{\rho})$ at various time instants. Note: FPD model (solid) and TRANSP output (dash) in each subfigure.

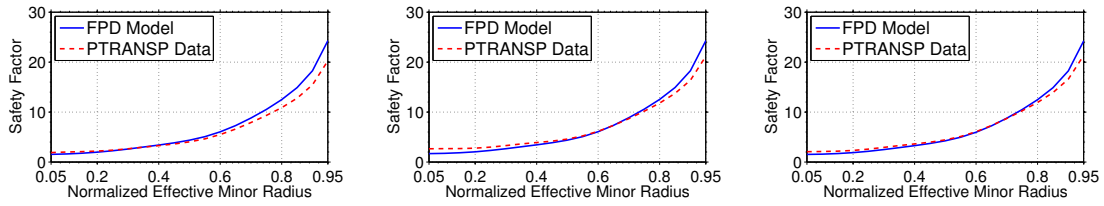

(a) $t = 1$ s. (b) $t = 3$ s. (c) $t = 6$ s.

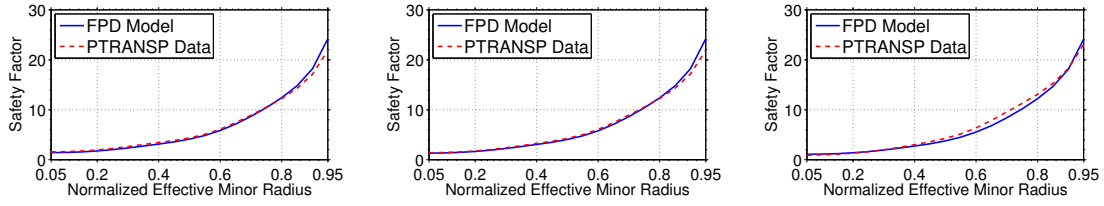

(d) $t = 9$ s. (e) $t = 12$ s. (f) $t = 15$ s.

Figure 2.26: Safety factor profile $q(\hat{\rho})$ at various time instants. Note: FPD model (solid) and TRANSP output (dash) in each subfigure.

2.6.3 Reference Run 121123Z80

2.6.3.1 Identification of Reference Profiles and Constants

The reference run 121123Z80 is a rerun of the original run 121123RN80 in TRANSP with the new capability so as to view power and current separately for each individual beam line. NSTX-U run 121123Z80 is still a TRANSP run with the NSTX-U shape and actuators, using the scaled profiles from NSTX. In this case study, the FPD model generated in Section 2.6.2 based on the NSTX-U TRANSP run 121123Z42 is simulated using the actuators of the NSTX-U TRANSP run 121123Z80 to test the FPD model's capability to reproduce the dynamics of different runs. The actuators extracted from the new run (121123Z80) are plotted in Fig. 2.27.

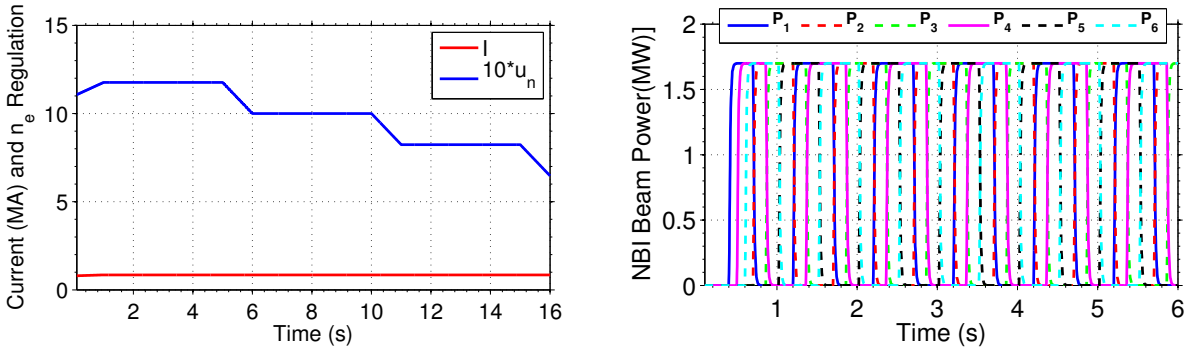

(a) (b)

Figure 2.27: Physical inputs applied during the FPD model simulation: (a) Total plasma current, and electron density regulation, u_n, (b) powers of the individual neutral beam injectors (same trend continues after 6 s. until 16 s.).

2.6.3.2 Qualitative Agreement of Various Plasma Profiles in between the FPD Model and TRANSP Output

Evolution of the poloidal flux (ψ) and safety factor (q) profiles, as obtained from TRANSP and predicted by FPD model are compared at different time instants in Figs. 2.28 and 2.29, respectively. Figs. 2.28 and 2.29 show reasonable agreement between predictions by the FPD control-oriented model and TRANSP simulations.

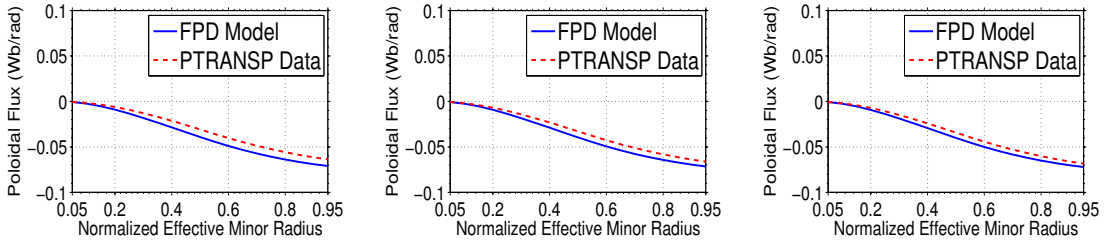

(a) $t = 1$ s. (b) $t = 3$ s. (c) $t = 6$ s.

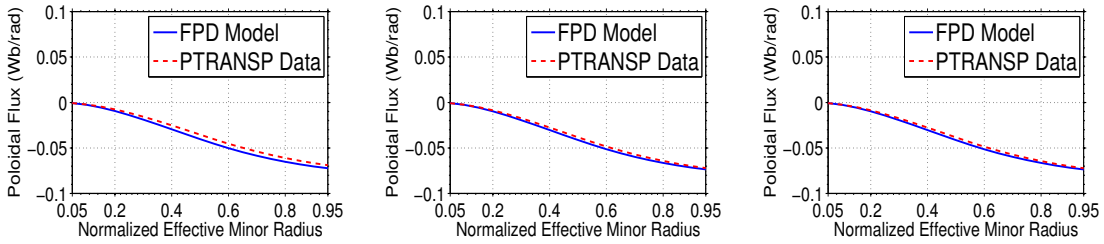

(d) $t = 9$ s. (e) $t = 12$ s. (f) $t = 15$ s.

Figure 2.28: Poloidal flux profile $\psi(\hat{\rho})$ at various time instants. Note: FPD model (solid) and TRANSP output (dash) in each subfigure.

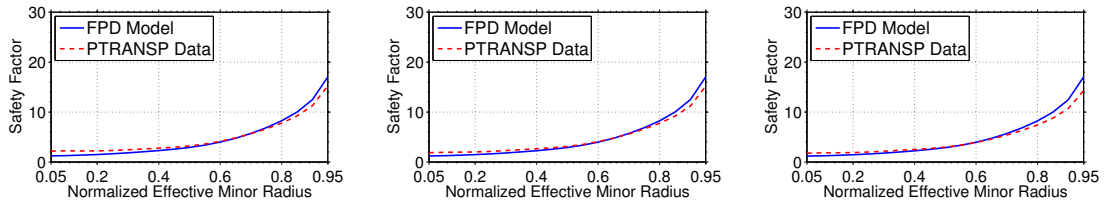

(a) $t = 1$ s. (b) $t = 3$ s. (c) $t = 6$ s.

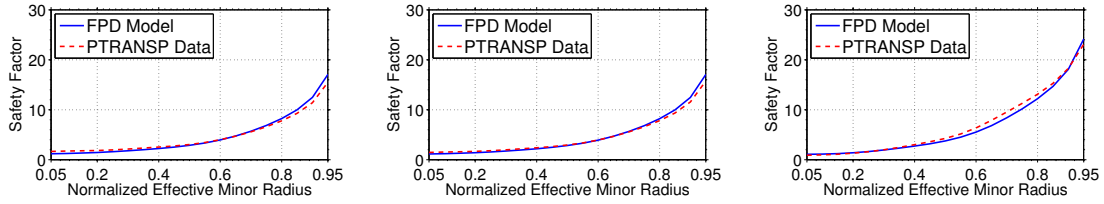

(d) $t = 9$ s. (e) $t = 12$ s. (f) $t = 15$ s.

Figure 2.29: Safety factor profile $q(\hat{\rho})$ at various time instants. Note: FPD model (solid) and TRANSP output (dash) in each subfigure.

2.7 Conclusion

In this section, the nonlinear magnetic-diffusion PDE has been coupled with empirical models for the electron density, electron temperature, plasma resistivity and non-inductive current drive (neutral beams and bootstrap) to produce a first-principles-driven (FPD) control-oriented model of the current profile response in both NSTX and NSTX-U.

The proposed control-oriented model takes into account the effects of the neutral beam injectors independently, rather than lumping them into a single input to exploit the full capabilities of the machine's heating and current drive system. The modeling of the magnetic geometry allows for a time-varying approach, which could potentially increase the model accuracy and provide a mechanism for integration with plasma shape control.

Simulation studies show that the predictions of the FPD control-oriented model are in reasonable agreement with TRANSP simulations for the purpose of control design. Further analysis is still needed to explain some observed mismatches. Therefore, a next-step goal should be to refine the FPD model using actual experimental data once NSTX-U begins producing meaningful plasmas so that prediction accuracy could be improved for more reliable design and testing of various control algorithms.

Chapter 3

Feedforward Actuator Trajectory Optimization for Scenario Planning in NSTX-U

3.1 Introduction

In this chapter, a nonlinear optimization technique is introduced to compute offline actuator trajectories to achieve specific plasma scenarios. Given a desired operating state, the optimizer produces the feedforward actuator trajectories that steer the plasma to such state. The development of such scenarios is conventionally carried out experimentally by modifying the tokamak's actuator trajectories and analyzing the resulting plasma evolution. The objective of the feedforward control design is to provide a systematic approach to advanced scenario planning in NSTX-U. The feedforward control law, which is the first component of the overall current-profile control approach proposed in this work, is later complemented by feedback control laws as those proposed in Chapters 4 and 5.

Earlier work towards actuator trajectory optimization can be found in [70], [71] and [1] for the DIII-D tokamak, and in [72] for the TCV tokamak [73]. In [1], a nonlinear optimization technique is proposed for advanced scenario planning in DIII-D based on a first-principles-driven model (Section 2). The work presented in this chapter extends this optimization technique to NSTX-U.

This chapter is organized as follows. A cost functional that defines the objective of the optimization problem is introduced in Section 3.2. Mathematical formulations of the plasma state and actuator constraints are provided in Section 3.3. By combining the cost functional and the constraints, the statement of the nonlinear optimization problem is provided in Section 3.4 along with the Sequential Quadratic Programming solution algorithm. Results of the numerical simulations that utilize the proposed nonlinear optimization algorithm are shown in Section 3.5. Finally, a brief conclusion and a future work statement are provided in Section 3.6.

3.2 Definition of the Cost Functional for a Target Plasma State

The objective of the optimization algorithm is to design actuator trajectories that can steer the plasma from an initial state to a target state defined by a target q-profile such that the achieved state is stationary in time, subject to the plasma dynamics described by the nonlinear, control-oriented PDE model and actuator constraints, such as the maximum available amount of plasma current and NBI power.

Note that stationarity of the plasma is characterized by the loop-voltage profile, $U_p(\hat{\rho}, t)$, which can be related to the temporal derivative of the poloidal magnetic flux

$$U_p(\hat{\rho}, t) = -\frac{\partial \Psi}{\partial t} = -2\pi \frac{\partial \psi}{\partial t} \tag{3.1}$$

Since poloidal flux profile evolves with the slowest time constant in the plasma, when it reaches a stationary condition (i.e., $U_p(\hat{\rho}, t) = \text{constant}$) all other plasma profiles should have reached a stationary condition. Therefore, a stationary plasma is achieved when

$$g_{ss}(\hat{\rho}, t) = \frac{\partial U_p}{\partial \hat{\rho}} = 0 \tag{3.2}$$

The following cost functional [1] can then be defined to formulate the actuator trajectory optimization problem

$$J(t_f) = k_q J_q(t_f) + k_{ss} J_{ss}(t_f) \tag{3.3}$$

where k_{ss} and k_q are the weight factors representing the relative importance of the plasma state characteristics and

$$J_q(t_f) = \int_0^1 W_q(\hat{\rho}) \left[\bar{q}(\hat{\rho}) - q(\hat{\rho}, t_f)\right]^2 d\hat{\rho}, \tag{3.4}$$

$$J_{ss}(t_f) = \int_0^1 W_{ss}(\hat{\rho}) \left[g_{ss}(\hat{\rho}, t_f)\right]^2 d\hat{\rho}. \tag{3.5}$$

$W_q(\hat{\rho})$ and $W_{ss}(\hat{\rho})$ on the RHS of (3.4) and (3.5) are positive weight functions that define which portions of the respective profiles are more important relative to the others. Note that $J_q(t_f)$ in (3.4) is a measure of closeness of the q-profile achieved at the final time, t_f to the target profile, $\bar{q}(\hat{\rho})$. On the other hand, $J_{ss}(t_f)$ in (3.5) defines the stationarity of the q-profile reached at time t_f [1].

3.3 Formulation of Various Constraints

3.3.1 Plasma State Constraints

The main constraint of the actuator trajectory optimization problem is imposed by the plasma state dynamics given by the MDE (2.42)-(2.43) in Chapter 2.

A control-oriented plasma state equation can be obtained by discretizing the infinite dimensional MDE (2.42)-(2.43) in space using finite difference approximations, while leaving the time domain continuous (see Section 4.3.1 for derivation). As a result, the spatial domain ($\hat{\rho} \in [0\ \ 1]$) is represented by l discrete radial nodes. Since equation (2.42) is a nonlinear PDE, the discrete form of it yields a set of nonlinear ODEs, which can be represented compactly as

$$\dot{\theta}(t) = z(\theta(t), u(t)), \tag{3.6}$$

where $\theta = [\theta_2, \theta_3, ..., \theta_{l-1}]^T \in \mathbb{R}^n$ is the value of the poloidal flux gradient profile, $\theta(\hat{\rho}, t) = \partial\psi/\partial\hat{\rho}$ at the $n = l-2$ interior nodes and $u = [u_n, P_1, P_2, ..., P_6, I_p]^T \in \mathbb{R}^8$ is the physical actuators of the NSTX-U, and $z \in \mathbb{R}^n$ is a nonlinear vector function of the states, physical actuators, and the model parameters (see (4.21) in Section 4.3.1 for details).

Note that equation (3.6) governs the dynamic behavior of the plasma state, i.e., the poloidal flux gradient profile, $\theta(\hat{\rho}, t) = \partial\psi/\partial\hat{\rho}$, which can be related to the current density profile through the rotational transform (ι), or safety factor (q) as shown in Sections 2.2.1 and 2.2.2. Therefore, equation (3.6) is referred to as plasma state equation throughout the rest of this dissertation.

3.3.2 Actuator Trajectory Parameterization

Parametric description of the actuator trajectories may be useful for advanced scenario planning in NSTX-U because certain operating conditions could be guaranteed by forcing actuators to pass through some fixed values at certain times. Adjustment of the free parameters of each actuator trajectory could then be possible by solving the proposed nonlinear optimization problem defined by the cost functional (3.3) subject to the various plasma state and actuator constraints introduced in this section.

Therefore, the idea is to specify each physical actuator trajectory, u_i, by a number of discrete parameters at discrete points in time, i.e.,

$$u_i(t_i) = \left[u_i^1\,, u_i^2\,, u_i^3\,, \ldots,\, u_i^{n_i}\right], \tag{3.7}$$

where t_i defines the discrete time array

$$t_i = \left[t_0 = t^1\,, t^2\,, t^3\,, \ldots,\, t^{n_i} = t_f\right] \in \mathbb{R}^{n_i}, \tag{3.8}$$

with n_i being the dimension of the parameter space of the i-th actuator. Hence, the value of the actuator, u_i at an intermediate time point $t \in \left[t^k,\, t^{k+1}\right]$ could be found through a linear interpolation between the neighboring parameters, i.e.,

$$\begin{aligned} u_i(t) &= u_i(t^k) + \frac{u_i(t^{k+1}) - u_i(t^k)}{t^{k+1} - t^k}(t - t^k) \\ &= u_i^k + \frac{u_i^{k+1} - u_i^k}{t^{k+1} - t^k}(t - t^k). \end{aligned} \tag{3.9}$$

Note that by combining all parameters to represent all actuator trajectories into a

single vector

$$\tilde{x} = \left[u_1^1, \ldots, u_1^{n_1}, \ldots, u_i^1, \ldots, u_i^{n_i}, \ldots, u_8^1, \ldots, u_8^{n_8}\right] \in \mathbb{R}^{n_t}, \tag{3.10}$$

where $n_t = \sum_{i=1}^{8} n_i$, the physical control actuator trajectories can be expressed compactly as

$$u(t) = M(t)\tilde{x}, \tag{3.11}$$

where $u(t) \in \mathbb{R}^8$, and $M(t) \in \mathbb{R}^{8 \times n_t}$ is a piecewise linear function of time. Note that some parameters of the vector (3.10) may be held fixed to reach an operating condition as a part of scenario planning. Therefore, the free parameters in the vector (3.10) could be grouped together to form a vector of to-be-optimized parameters which can be expressed as $x \in \mathbb{R}^{n_t^{opt}}$ where $n_t^{opt} \leq n_t$, and in this case (3.11) reduces into

$$u(t) = N(t)x, \tag{3.12}$$

where $N(t) \in \mathbb{R}^{8 \times n_t^{opt}}$ is also a piecewise linear function of time. Note that all fixed parameters of the array $\tilde{x}$ in (3.11) are now included in $N(t)$, while unknown parameters are separated in the vector, x.

3.3.3 Actuator Constraints

The following actuator magnitude constraints are imposed on the actuator trajectory optimization problem in NSTX-U

$$I_{p_{min}} \leq I_p(t) \leq I_{p_{max}}, \tag{3.13}$$

$$P_{min} \leq P_i(t) \leq P_{max}, \quad i = 1, \ldots, 6 \tag{3.14}$$

where $(\cdot)_{min}$ and $(\cdot)_{max}$ stand for the minimum and maximum limits, respectively.

Since the plasma current, $I_p(t)$, and neutral beam powers, $P_i(t)$ could be parametrized similar to (3.12), it is possible to rewrite the constraints (3.13)-(3.14) as a single matrix inequality in terms of the to-be-optimized parameters x as

$$A_u(t)x \leq b_u. \tag{3.15}$$

3.4 Statement of the Optimization Problem and Solution Algorithm

3.4.1 Nonlinear Optimization Problem Statement

Note that the cost functional $J(t_f) = k_q J_q(t_f) + k_{ss} J_{ss}(t_f)$ depends on $q(\hat{\rho}, t_f)$ and $g_{ss}(\hat{\rho}, t_f)$, through J_q and J_{ss}, respectively (see equations (3.3)-(3.5)). Since $q(\hat{\rho}, t_f)$ depends on the poloidal flux gradient profile, $\theta(\hat{\rho}, t_f) = \frac{\partial \psi}{\partial \hat{\rho}}(\hat{\rho}, t_f)$ through (2.2)-(2.4), and $g_{ss}(\hat{\rho}, t_f)$ depends on $\dot{\theta}(\hat{\rho}, t_f)$ through (3.1)-(3.2) as

$$g_{ss}(\hat{\rho}, t_f) = \frac{\partial U_p}{\partial \hat{\rho}} = \frac{\partial}{\partial \hat{\rho}} \left(-2\pi \frac{\partial \psi}{\partial t} \right) = -2\pi \frac{\partial}{\partial t} \left(\frac{\partial \psi}{\partial \hat{\rho}} \right) = -2\pi \dot{\theta}(\hat{\rho}, t_f), \tag{3.16}$$

the cost functional J then depends on $\theta(\hat{\rho}, t_f)$ and $\dot{\theta}(\hat{\rho}, t_f)$.

By combining the cost functional (3.3) with the constraints due to the plasma dynamics (3.6), actuator trajectory parametrization (3.12), and the actuator magnitude limits (3.15), a nonlinear constrained optimization problem could be defined in terms of the unknown (i.e., to-be-optimized) actuator parameters, x.

The mathematical description of the optimization problem then becomes

$$\min_{x} \quad J(t_f) = J(\dot{\theta}(t_f), \theta(t_f)), \tag{3.17}$$

subject to

$$\dot{\theta} = z(\theta, u), \tag{3.18}$$

$$u(t) = N(t)x, \tag{3.19}$$

$$A_u(t)x \leq b_u. \tag{3.20}$$

The above optimization problem can be solved by using a method called sequential quadratic programming (SQP) [74]. The SQP method is based on determining a local minimizer of the nonlinear program (NLP) (3.17)-(3.20) through iterative solutions of a sequence of quadratic programs (QP). Each iteration starts with a current estimate of a local minimizer of the NLP and a QP which minimizes a quadratic approximation of the original system Hamiltonian subject to a linear approximation of the system constraints around the current estimate. The solution of each QP then provides a step toward the solution of the original NLP [1].

3.4.2 Sequential Quadratic Programming Algorithm [1]

In this section, an overview of the SQP solution method is provided for a general NLP defined by

$$\min_{v} \quad \mathcal{J}(z, v) \quad \text{such that} \quad f(z, v) = 0. \tag{3.21}$$

To simplify the explanation of the SQP technique, we only consider equality constraints of the form shown in (3.21). This however is not a limitation of the presented technique because of the fact that inequality constraints of the form $f(z, v) \leq 0$ can

be converted into equality constraints in the form of (3.21) by introducing a slack vector ε such that $f(z,v)+\varepsilon=0$. First of all, the system Hamiltonian is defined as

$$\mathcal{H}(z,v,\lambda)=\mathcal{J}(z,v)+\lambda^T f(z,v), \tag{3.22}$$

where λ is a to-be-determined Lagrange multiplier. An incremental change in the Hamiltonian with respect to changes in the parameters is given to first order by

$$d\mathcal{H}=\mathcal{H}_z dz+\mathcal{H}_v dv+\mathcal{H}_\lambda d\lambda, \tag{3.23}$$

where $(\cdot)_i=\frac{\partial(\cdot)}{\partial i}$ for $i\in\{z,v,\lambda\}$. At a local minimum (z^*,v^*,λ^*), $d\mathcal{H}$ must be zero for all increments dz, dv, $d\lambda$. Therefore, the first-order optimality conditions for the NLP (3.21) are given by the nonlinear equations

$$\begin{aligned}
\mathcal{H}_z(z^*,v^*,\lambda^*) &= \mathcal{J}_z(z^*,v^*)+(\lambda^*)^T f_z(z^*,v^*)=0,\\
\mathcal{H}_v(z^*,v^*,\lambda^*) &= \mathcal{J}_v(z^*,v^*)+(\lambda^*)^T f_v(z^*,v^*)=0,\\
\mathcal{H}_\lambda(z^*,v^*,\lambda^*) &= f(z^*,v^*)=0.
\end{aligned} \tag{3.24}$$

One approach to solving the NLP (3.21) is to assume that there is an iteration

$$\left(z^{(k+1)},v^{(k+1)},\lambda^{(k+1)}\right)=\left(z^{(k)},v^{(k)},\lambda^{(k)}\right)+\left(\zeta^{(k)},\xi^{(k)},\sigma^{(k)}\right) \tag{3.25}$$

that is converging to the solution (z^*,v^*,λ^*) of (3.24), where $(\zeta^{(k)},\xi^{(k)},\sigma^{(k)})$ are search directions. If the current estimate $(z^{(k)},v^{(k)},\lambda^{(k)})$ is close to (z^*,v^*,λ^*), it is possible

to linearize (3.24) around $(z^{(k)}, v^{(k)}, \lambda^{(k)})$, i.e.,

$$\begin{aligned}
0 &= \mathcal{H}_z(z^{(k)}, v^{(k)}, \lambda^{(k)}) + \mathcal{H}_{zz}(z^{(k)}, v^{(k)}, \lambda^{(k)})\zeta^{(k)} \\
&\quad + \mathcal{H}_{zv}(z^{(k)}, v^{(k)}, \lambda^{(k)})\xi^{(k)} + \mathcal{H}_{z\lambda}(z^{(k)}, v^{(k)}, \lambda^{(k)})\sigma^{(k)}, \\
0 &= \mathcal{H}_v(z^{(k)}, v^{(k)}, \lambda^{(k)}) + \mathcal{H}_{vz}(z^{(k)}, v^{(k)}, \lambda^{(k)})\zeta^{(k)} \\
&\quad + \mathcal{H}_{vv}(z^{(k)}, v^{(k)}, \lambda^{(k)})\xi^{(k)} + \mathcal{H}_{v\lambda}(z^{(k)}, v^{(k)}, \lambda^{(k)})\sigma^{(k)}, \\
0 &= \mathcal{H}_\lambda(z^{(k)}, v^{(k)}, \lambda^{(k)}) + \mathcal{H}_{\lambda z}(z^{(k)}, v^{(k)}, \lambda^{(k)})\zeta^{(k)} \\
&\quad + \mathcal{H}_{\lambda v}(z^{(k)}, v^{(k)}, \lambda^{(k)})\xi^{(k)} + \mathcal{H}_{\lambda\lambda}(z^{(k)}, v^{(k)}, \lambda^{(k)})\sigma^{(k)},
\end{aligned} \tag{3.26}$$

where $(\cdot)_{ij} = \frac{\partial^2(\cdot)}{\partial i \partial j}$ for $i \in \{z, v, \lambda\}$ and $j \in \{z, v, \lambda\}$. From (3.24), note that $\mathcal{H}_{z\lambda} = \mathcal{H}_{\lambda z} = f_z$, $\mathcal{H}_{v\lambda} = \mathcal{H}_{\lambda v} = f_v$, and $\mathcal{H}_{\lambda\lambda} = 0$, therefore, (3.26) can be rewritten as

$$\begin{bmatrix} \mathcal{H}_{zz} & \mathcal{H}_{zv} & f_z \\ \mathcal{H}_{vz} & \mathcal{H}_{vv} & f_v \\ f_z & f_v & 0 \end{bmatrix}\Bigg|_{(z^{(k)}, v^{(k)}, \lambda^{(k)})} \begin{bmatrix} \zeta^{(k)} \\ \xi^{(k)} \\ \sigma^{(k)} \end{bmatrix} = - \begin{bmatrix} H_z \\ H_v \\ f \end{bmatrix}\Bigg|_{(z^{(k)}, v^{(k)}, \lambda^{(k)})} \tag{3.27}$$

The search directions $(\zeta^{(k)}, \xi^{(k)}, \sigma^{(k)})$ can then be obtained by solving (3.27). It can be shown that the first-order optimality condition of the QP

$$\min_{\xi^{(k)}} \quad \mathcal{L}(\zeta^{(k)}, \xi^{(k)})\big|_{(z^{(k)}, v^{(k)}, \lambda^{(k)})}, \tag{3.28}$$

such that

$$f(z^{(k)}, v^{(k)}) + \begin{bmatrix} f_z & f_v \end{bmatrix}\Big|_{(z^{(k)}, v^{(k)})} \begin{bmatrix} \zeta^{(k)} \\ \xi^{(k)} \end{bmatrix} = 0, \tag{3.29}$$

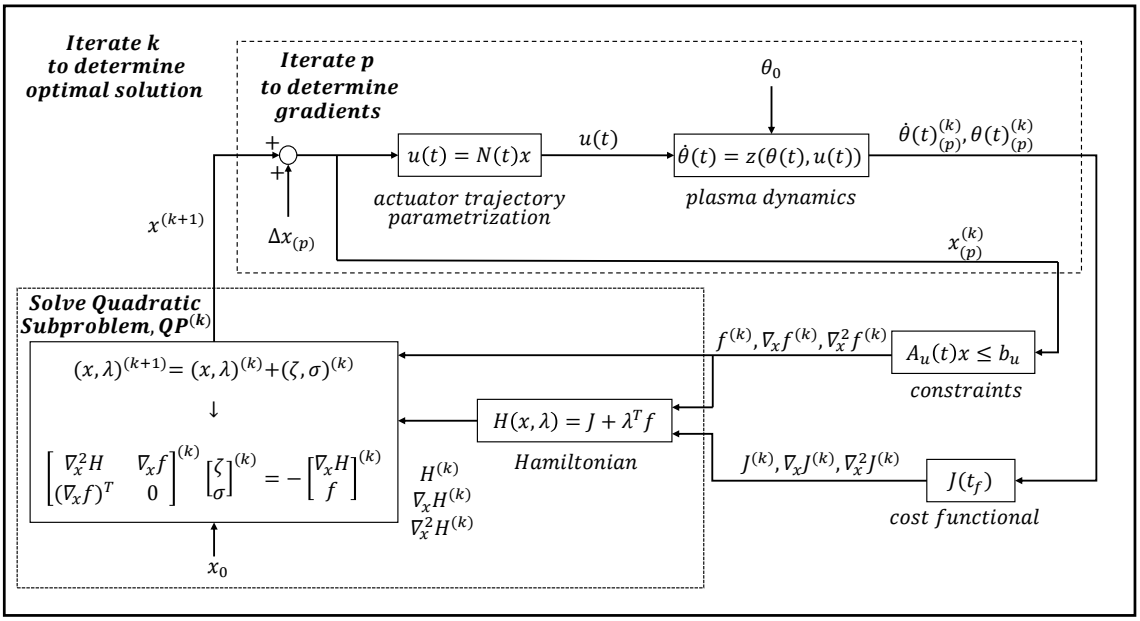

Figure 3.1: A block diagram representation of the SQP algorithm for the solution of the nonlinear actuator trajectory optimization problem in NSTX-U.

where

$$\mathcal{L} = \mathcal{H} + \begin{bmatrix} \mathcal{H}_z & \mathcal{H}_v \end{bmatrix} \begin{bmatrix} \zeta^{(k)} \\ \xi^{(k)} \end{bmatrix} + \frac{1}{2} \begin{bmatrix} \zeta^{(k)} & \xi^{(k)} \end{bmatrix} \begin{bmatrix} \mathcal{H}_{zz} & \mathcal{H}_{zv} \\ \mathcal{H}_{vz} & \mathcal{H}_{vv} \end{bmatrix} \begin{bmatrix} \zeta^{(k)} \\ \xi^{(k)} \end{bmatrix},$$

with Lagrange multiplier $\sigma^{(k)}$, is given by (3.27). Search directions for the NLP (3.21) can then be obtained from the sequence of quadratic programs (3.28)-(3.29), which represent a quadratic approximation of $\mathcal{H}$ subject to a linear approximation of f around the current estimate $(z^{(k)}, v^{(k)}, \lambda^{(k)})$.

A block diagram that summarizes the SQP computational approach for actuator trajectory optimization in NSTX-U is depicted in Figure 3.1. Note that the upper block represents the NLP (3.17)-(3.20), while the lower block stands for the sequence of quadratic programs to be solved.

3.5 Numerical Testing of the Actuator Trajectory Optimization in NSTX-U

In this section, the nonlinear actuator trajectory optimization problem (3.17)-(3.20) is solved in MATLAB by using the SQP algorithm for 3 different scenario goals specified in the following 3 subsections. To reduce the computational time, only 4 out of the 6 neutral beam injectors (P_2, P_3, P_4, P_5) and total plasma current (I_p) are considered as the control actuators to be optimized. In each case, the target plasma state is characterized by a target q-profile obtained through the numerical simulation of the nonlinear MDE (2.42)-(2.43) in MATLAB for arbitrary inputs.

3.5.1 Weighting Only the *q*-Profile

One can achieve different scenarios by adjusting the relative importance of the weights k_q and k_{ss} in the cost functional (3.3). One possible application is to weight only the q-profile. For this application, $k_q = 1$ and $k_{ss} = 0$ in the cost functional (3.3). Therefore, the goal is to hit a target q-profile at the end of the optimization interval, t_f=1.0 s. The optimization is carried out during the time interval $t \in [0.05\ \ 1.00]$ s., and actuators are parametrized by using $n_i = 6$ discrete parameters at the time points $t_i = [0.050,\ 0.100,\ 0.325,\ 0.550,\ 0.775,\ 1.000]$ s.

The time evolution of the optimized feedforward actuator trajectories are shown in Fig. 3.2. The target and achieved safety factors (q) are compared at various radial locations in Fig 3.3(a), and at different instants in Fig. 3.3(b)-(d).

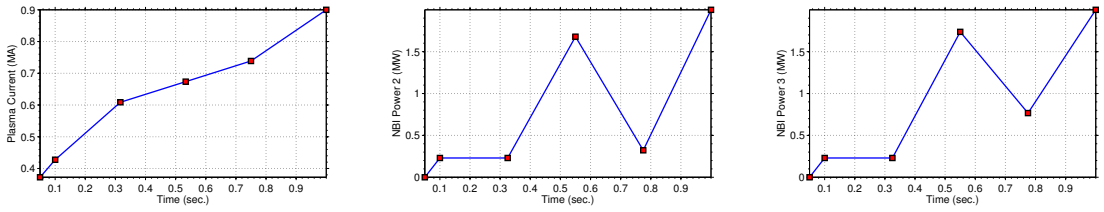

(a) Optimal $I_p(t)$ (b) Optimal NBI power, $P_2(t)$ (c) Optimal NBI power, $P_3(t)$

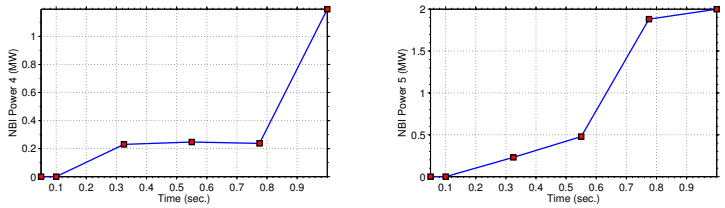

(d) Optimal NBI power, $P_4(t)$ (e) Optimal NBI power, $P_5(t)$

Figure 3.2: Time evolution of the optimized feedforward actuator trajectories

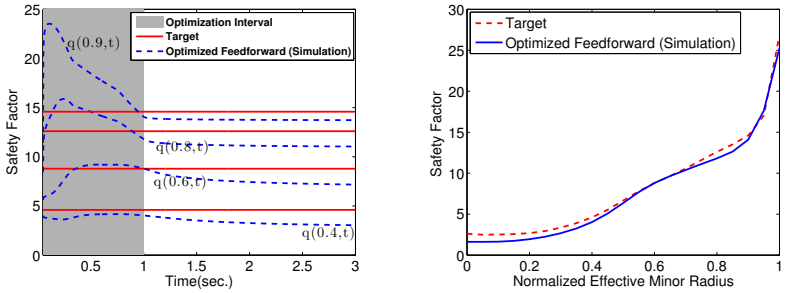

(a) $q(\hat{\rho}, t)$ (b) $t = t_f = 1.0$ s.

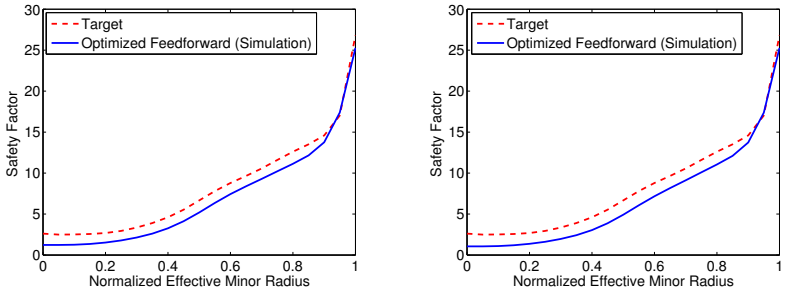

(c) $t = 2.0$ s. (d) $t = 3.0$ s.

Figure 3.3: Numerical testing of optimized actuator trajectories: (a) Time evolution of the safety factor at various radial locations (from top to bottom: $q(0.9, t)$, $q(0.8, t)$, $q(0.6, t)$ and $q(0.4, t)$). (b)-(d): Comparison of the target and achieved q-profiles at various times.

3.5.2 Weighting Only the Steadiness

Another application is to weight only the stationarity of the q-profile. For this application, $k_q = 0$ and $k_{ss} = 1$ in the cost functional (3.3). Therefore, the goal is to optimize the actuator trajectories so as to maintain a steady q-profile throughout the rest of the simulation. The optimization is carried out during the time interval $t \in [0.05\ \ 0.5]$ s. Actuators are parametrized by using $n_i = 6$ discrete parameters at the time points $t_i = [0.05,\ 0.1,\ 0.2,\ 0.3,\ 0.4,\ 0.5]$ s.

The time evolution of the optimized feedforward actuator trajectories are shown in Fig. 3.4. The target and achieved safety factors (q) are compared at various radial locations in Fig 3.5(a), and at different instants in Fig. 3.5(b)-(d).

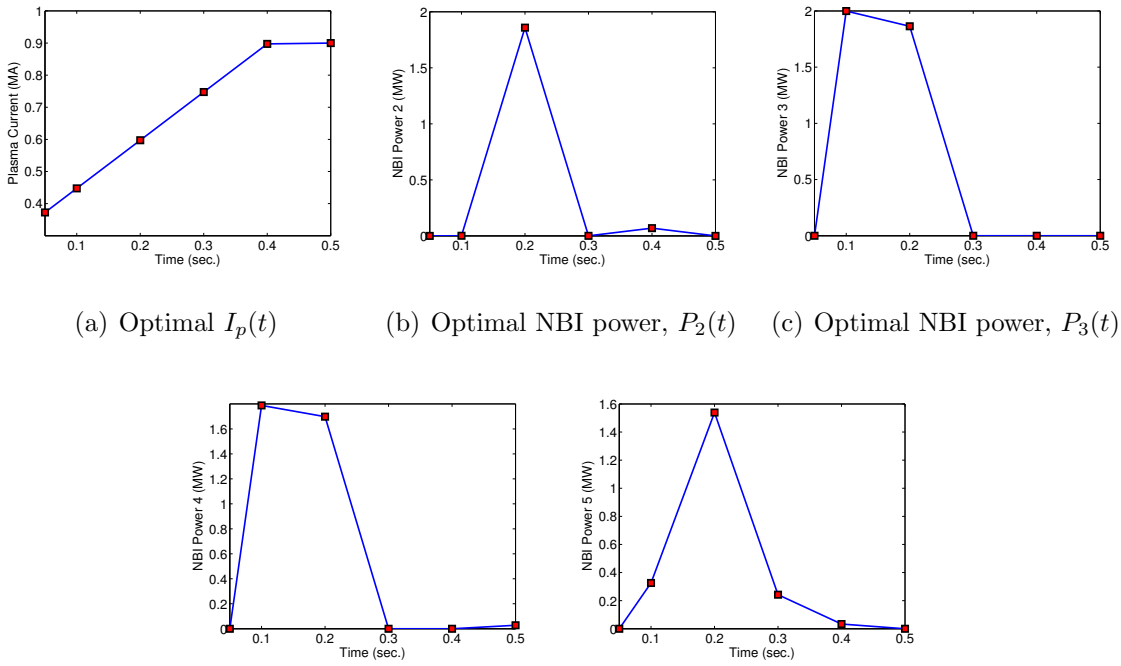

(a) Optimal $I_p(t)$ (b) Optimal NBI power, $P_2(t)$ (c) Optimal NBI power, $P_3(t)$

(d) Optimal NBI power, $P_4(t)$ (e) Optimal NBI power, $P_5(t)$

Figure 3.4: Time evolution of the optimized feedforward actuator trajectories

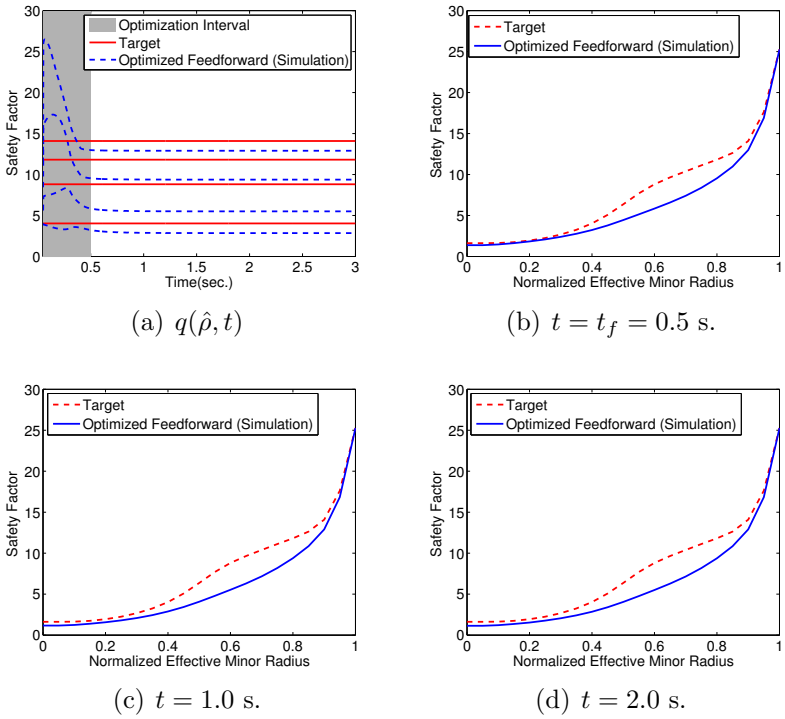

(a) $q(\hat{\rho}, t)$ (b) $t = t_f = 0.5$ s.

(c) $t = 1.0$ s. (d) $t = 2.0$ s.

Figure 3.5: Numerical testing of optimized actuator trajectories: (a) Time evolution of the safety factor at various radial locations (from top to bottom: $q(0.9, t)$, $q(0.8, t)$, $q(0.6, t)$ and $q(0.4, t)$). (b)-(d): Comparison of the target and achieved q-profiles at various times.

3.5.3 Weighting the q-Profile and Steadiness

As a final application, one could equally weight the q-profile and its stationarity by setting $k_q = k_{ss} = 1$ in the cost functional (3.3). Therefore, the goal is to hit a target profile at the end of the optimization interval and maintain it throughout the rest of the simulation. The optimization is carried out during the time interval $t \in [0.05 \;\; 0.5]$ s., and actuators are parametrized by using $n_i = 6$ discrete parameters at the time points $t_i = [0.05,\ 0.1,\ 0.2,\ 0.3,\ 0.4,\ 0.5]$ s.

The time evolution of the optimized feedforward actuator trajectories are shown in Fig. 3.6. The target and achieved safety factors (q) are compared at various radial locations in Fig. 3.7(a), and at different instants in Fig. 3.7(b)-(d).

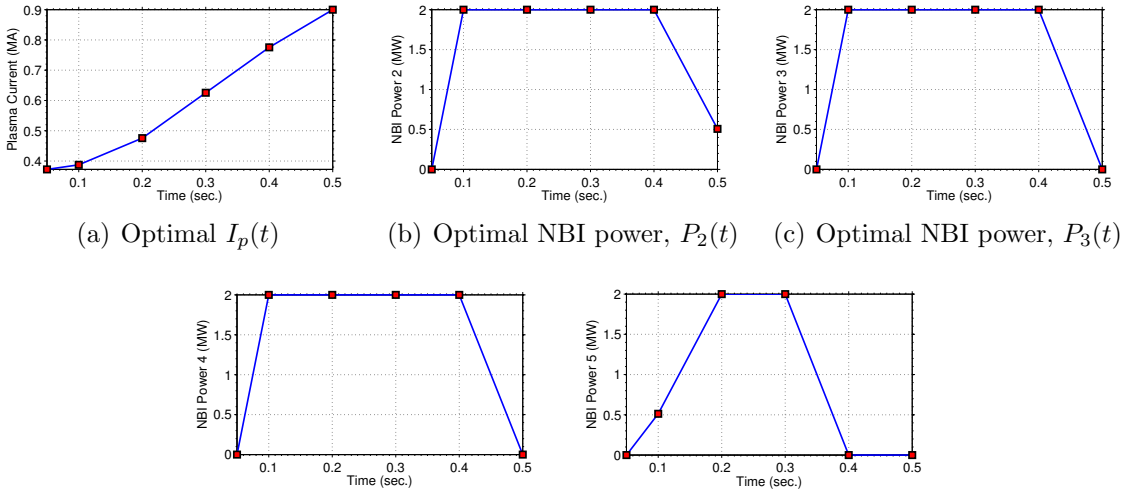

(a) Optimal $I_p(t)$ (b) Optimal NBI power, $P_2(t)$ (c) Optimal NBI power, $P_3(t)$

(d) Optimal NBI power, $P_4(t)$ (e) Optimal NBI power, $P_5(t)$

Figure 3.6: Time evolution of the optimized feedforward actuator trajectories

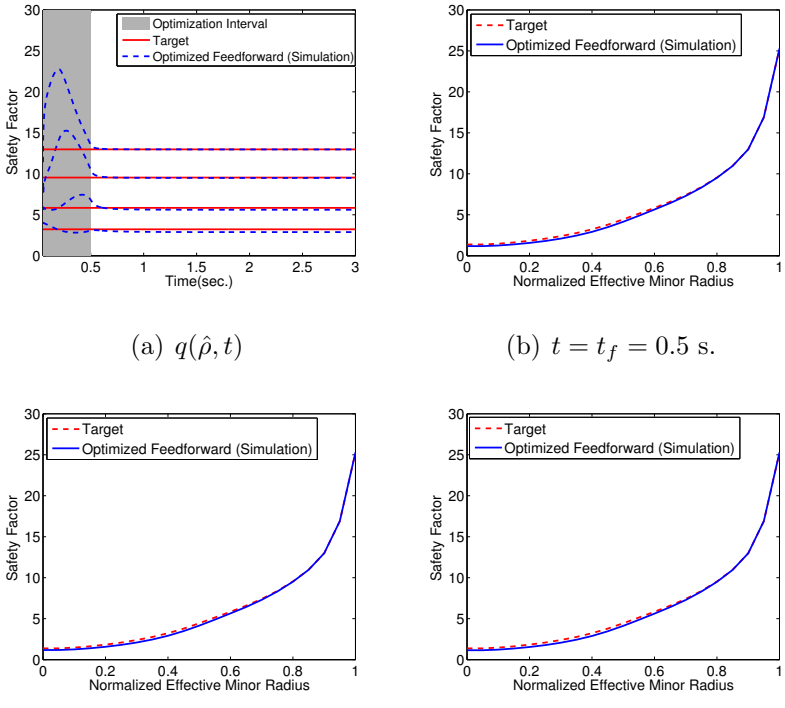

(a) $q(\hat{\rho}, t)$ (b) $t = t_f = 0.5$ s.

(c) $t = 1.0$ s. (d) $t = 2.0$ s.

Figure 3.7: Numerical testing of optimized actuator trajectories: (a) Time evolution of the safety factor at various radial locations (from top to bottom: $q(0.9, t)$, $q(0.8, t)$, $q(0.6, t)$ and $q(0.4, t)$). (b)-(d): Comparison of the target and achieved q-profiles at various times.

3.6 Conclusion

In this chapter, the FPD model has been embedded in a nonlinear optimization algorithm to produce optimal actuator trajectories that steer the plasma states to a target scenario characterized by both the shape and the steadiness of the q-profile. The model-based optimization algorithm provides a systematic approach to scenario planning in NSTX-U. The optimization problem is formulated using a cost functional that measures both the matching between actual and target q profiles and the steadiness of the actual q profile. The solution of this optimization problem is constrained by the plasma dynamics, the actuator saturation limits, and the actuator trajectory parametrization.

Future work includes the design of feedforward controllers based on augmented cost functions. These cost functions, which will further constrain the optimization problem in order to obtain more physically sound actuator trajectories, will be complemented by the refinement and augmentation of the FPD model as meaningful experimental data from NSTX-U becomes available. The optimized actuator trajectories will then be tested in open-loop TRANSP simulations and eventually through feedforward optimization experiments in NSTX-U.

Moreover, future work also includes the possibility of constraining the optimization problem by more sophisticated physics-oriented models. For instance, the same optimization algorithm could be wrapped around TRANSP instead of around the control-oriented transport model as proposed in this work. However, the increase of prediction accuracy would be paid by the increase of the computational time required to solve the optimization problem.

Chapter 4

Model-based Optimal Control of the Current Density Profile Evolution in NSTX-U

4.1 Introduction

Active control of the toroidal current density profile is among those plasma control milestones that the NSTX-U program must achieve to realize its next-step operational goals, which are characterized by high-performance, long-pulse, MHD-stable plasma operation with neutral beam heating. As a first step towards the realization of this goal, a first-principles-driven, control-oriented model has been proposed in Chapter 2 to predict the spatial-temporal evolution of the current density profile by combining the poloidal magnetic flux diffusion equation with empirical correlations obtained at NSTX-U for the electron density, electron temperature, and non-inductive current drives. As a second step, the proposed FPD model has been used in Chapter 3 to obtain optimal feedforward trajectories.

In this chapter, an optimal feedback control law is proposed to complement the optimal feedforward trajectories in order to gain robustness against model uncertainties and external disturbances. The proposed control-oriented model is embedded in a feedback control scheme based on a linear quadratic (LQ) optimal control strategy to track a desired current density profile evolution specified indirectly by a desired safety factor profile (q profile) or a desired rotational transform profile (ι profile). An integrator is embedded into the standard LQ optimal formulation to account for unmodeled dynamics and disturbances. The neutral beam powers, electron density, and total plasma current are used as actuators. The effectiveness of the proposed feedback control strategy in regulating the current density profile in NSTX-U is demonstrated via closed-loop nonlinear simulations.

This chapter is organized as follows. In Section 4.2, the NSTX-U tailored, control-oriented form of the MDE (2.42) is rewritten in terms of the poloidal magnetic flux gradient profile, $\theta(\hat{\rho}, t) = \partial\psi/\partial\hat{\rho}$. This transformation makes it easier to convert the to-be-controlled variable $\theta(\hat{\rho}, t)$ into the toroidal current density profile through the safety factor (q) or rotational transform (ι) profiles. The resulting infinite-dimensional, control-oriented PDE governing the evolution of the poloidal magnetic flux gradient profile is first reduced into a finite-dimensional form and then linearized to provide a Linear-Time-Variant (LTV) state-space model in Section 4.3. Based on the proposed state-space model, a Linear-Quadratc-Integral (LQI) optimal controller is designed in Section 4.4 for tracking a desired safety factor profile, and hence a desired current density profile in NSTX-U. The effectiveness of the optimal tracking controller is tested in nonlinear simulations based on the developed control-oriented transport model in Section 4.5 and on TRANSP [46] in Section 4.6 through the recently developed Expert routine [2]. Finally, a brief conclusion is provided in Section 4.7.

4.2 Poloidal Magnetic Flux Gradient Profile Evolution Model

The MDE (2.5) is combined with simplified, NSTX-U-tailored models of electron density, electron temperature, plasma resistivity and noninductive current drives in Chapter 2. This allows us to separate space and time functions and rewrite the MDE in control-oriented form as in Section 2.4.3

$$\frac{\partial \psi}{\partial t} = f_\eta(\hat{\rho}) u_\eta(t) \frac{1}{\hat{\rho}} \frac{\partial}{\partial \hat{\rho}} \left(\hat{\rho} D_\psi(\hat{\rho}) \frac{\partial \psi}{\partial \hat{\rho}} \right) + \sum_{i=1}^{6} f_i(\hat{\rho}) u_i(t) + f_{bs}(\hat{\rho}) u_{bs}(t) \left(\frac{\partial \psi}{\partial \hat{\rho}} \right)^{-1}, \quad (4.1)$$

with the boundary conditions

$$\left. \frac{\partial \psi}{\partial \hat{\rho}} \right|_{\hat{\rho}=0} = 0 \ , \qquad \left. \frac{\partial \psi}{\partial \hat{\rho}} \right|_{\hat{\rho}=1} = -f_b I_p(t), \quad (4.2)$$

where the spatial functions f_η, f_i, f_{bs}, and f_b are dependent on the model reference profiles and constants (see Section 2.4.3), whereas the time functions

$$\bar{u} = [u_\eta,\, u_1,\, u_2,\, u_3,\, u_4,\, u_5,\, u_6,\, u_{bs},\, I_p]^T \in \mathbb{R}^{9\times 1} \quad (4.3)$$

are the control inputs, which are nonlinear combinations of the physical actuators,

$$u = [u_n,\, P_1,\, P_2,\, P_3,\, P_4,\, P_5,\, P_6,\, I_p]^T \in \mathbb{R}^{8\times 1}. \quad (4.4)$$

The nonlinear input transformations can then be written compactly as $\bar{u} = p(u)$, where $p \in \mathbb{R}^{9\times 8}$ is a nonlinear vector function defined as

$$p_1(u) = u_\eta(t) = \frac{u_n(t)^{3/2}}{I_p(t)^{3/2} P_{tot}(t)^{3/4}}, \tag{4.5}$$

$$p_{i+1}(u) = u_i(t) = \frac{P_i(t)}{I_p(t)\sqrt{P_{tot}(t)}}, \quad i=1,..,6 \tag{4.6}$$

$$p_8(u) = u_{bs}(t) = \frac{u_n(t)^{3/2}}{I_p(t)^{1/2} P_{tot}(t)^{1/4}}, \tag{4.7}$$

$$p_9(u) = I_p(t) = I_p(t), \tag{4.8}$$

where $P_{tot}(t)$ is the total power injected into the plasma (equation (2.16) in Section 2.3.2). Note that the q-profile is related to the poloidal flux gradient profile through (2.2), (2.3), and (2.4) as

$$q(\hat{\rho}, t) = -\frac{B_{\phi,0}\rho_b^2 \hat{\rho}}{\partial\psi/\partial\hat{\rho}} \tag{4.9}$$

Therefore, if we are able to control the poloidal flux gradient profile, which we define as

$$\theta(\hat{\rho}, t) = \partial\psi/\partial\hat{\rho}, \tag{4.10}$$

we will be able to control the q-profile, and hence the current density profile, assuming the system is controllable. Therefore, it is possible to define $\theta(\hat{\rho}, t)$ as the *to-be-controlled variable*. Equation (4.1) can be expanded according to the chain rule as

$$\begin{aligned}\frac{\partial\psi}{\partial t} =& f_\eta(\hat{\rho}) u_\eta(t) \frac{1}{\hat{\rho}} \left(\hat{\rho} \frac{\partial D_\psi(\hat{\rho})}{\partial\hat{\rho}} \frac{\partial\psi}{\partial\hat{\rho}} + D_\psi(\hat{\rho}) \frac{\partial\psi}{\partial\hat{\rho}} + \hat{\rho} D_\psi(\hat{\rho}) \frac{\partial^2\psi}{\partial\hat{\rho}^2} \right) + \sum_{i=1}^{6} f_i(\hat{\rho}) u_i(t) \\ &+ f_{bs}(\hat{\rho}) u_{bs}(t) \left(\frac{\partial\psi}{\partial\hat{\rho}} \right)^{-1}. \end{aligned} \tag{4.11}$$

Substituting (4.10) into (4.11), one can obtain

$$\frac{\partial \psi}{\partial t} = f_\eta u_\eta \frac{1}{\hat{\rho}} \left(\hat{\rho} D'_\psi \theta + D_\psi \theta + \hat{\rho} D_\psi \theta' \right) + \sum_{i=1}^{6} f_i u_i + f_{bs} u_{bs} \theta^{-1}, \tag{4.12}$$

where $(.)' = \partial / \partial \hat{\rho}$ for simplicity. Also, note that the time and space dependencies are dropped to reduce the representation. By differentiating (4.12) with respect to $\hat{\rho}$, the PDE governing the evolution of the *to-be-controlled variable* $\theta(\hat{\rho}, t)$ becomes

$$\frac{\partial}{\partial \hat{\rho}} \left[\frac{\partial \psi}{\partial t} \right] = \frac{\partial}{\partial \hat{\rho}} \left[f_\eta u_\eta \left(D'_\psi \theta + \frac{D_\psi}{\hat{\rho}} \theta + D_\psi \theta' \right) + \sum_{i=1}^{6} f_i u_i + f_{bs} u_{bs} \theta^{-1} \right]$$

$$\frac{\partial \theta}{\partial t} = \frac{\partial}{\partial \hat{\rho}} \left[f_\eta u_\eta D'_\psi \theta + f_\eta u_\eta \frac{D_\psi}{\hat{\rho}} \theta + f_\eta u_\eta D_\psi \theta' + \sum_{i=1}^{6} f_i u_i + f_{bs} u_{bs} \theta^{-1} \right] \tag{4.13}$$

Expanding the brackets:

$$\begin{aligned} \frac{\partial \theta}{\partial t} = & (f'_\eta D'_\psi u_\eta + f_\eta D''_\psi u_\eta) \theta + f_\eta D'_\psi u_\eta \theta' + \frac{1}{\hat{\rho}} (D'_\psi f_\eta + D_\psi f'_\eta) u_\eta \theta + \frac{1}{\hat{\rho}} (D_\psi f_\eta u_\eta) \theta' \\ & - \frac{1}{\hat{\rho}^2} D_\psi f_\eta u_\eta \theta + (D'_\psi f_\eta u_\eta + D_\psi f'_\eta u_\eta) \theta' + D_\psi f_\eta u_\eta \theta'' + \sum_{i=1}^{6} f'_i u_i \\ & + f'_{bs} \frac{1}{\theta} u_{bs} - f_{bs} \frac{\theta'}{\theta^2} u_{bs} \end{aligned} \tag{4.14}$$

Combining the similar terms together, equation (4.14) can be rewritten compactly as

$$\frac{\partial \theta}{\partial t} = h_0 u_\eta \theta'' + h_1 u_\eta \theta' + h_2 u_\eta \theta + f'_{bs} \frac{1}{\theta} u_{bs} - f_{bs} \frac{\theta'}{\theta^2} u_{bs} + \sum_{i=1}^{6} f'_i u_i \ , \tag{4.15}$$

subject to the boundary conditions

$$\theta \big|_{\hat{\rho}=0} = 0, \qquad \theta \big|_{\hat{\rho}=1} = -f_b I_p(t), \tag{4.16}$$

where

$$h_0(\hat{\rho}) = D_\psi(\hat{\rho}) f_\eta(\hat{\rho}) \tag{4.17}$$

$$h_1(\hat{\rho}) = \left(D'_\psi(\hat{\rho}) + \frac{1}{\hat{\rho}} D_\psi(\hat{\rho}) + D'_\psi(\hat{\rho}) \right) f_\eta(\hat{\rho}) + D_\psi(\hat{\rho}) f'_\eta(\hat{\rho}) \tag{4.18}$$

$$h_2(\hat{\rho}) = \left(D''_\psi(\hat{\rho}) + \frac{1}{\hat{\rho}} D'_\psi(\hat{\rho}) - \frac{1}{\hat{\rho}^2} D_\psi(\hat{\rho}) \right) f_\eta(\hat{\rho}) + \left(D'_\psi(\hat{\rho}) + \frac{1}{\hat{\rho}} D_\psi(\hat{\rho}) \right) f'_\eta(\hat{\rho}) \tag{4.19}$$

4.3 Model Order Reduction and Linearization

4.3.1 Model Order Reduction via Truncated Taylor Series Expansion

To construct a reduced-order model suitable for feedback control, the governing PDE (4.15) is discretized in space into l nodes using the truncated Taylor series approach while leaving the time domain continuous. Since equation (4.15) is a non-linear PDE, the discrete form of it yields a set of nonlinear ODEs, which can be represented compactly as

$$\dot{\theta}(t) = g(\theta(t), \bar{u}(t)), \tag{4.20}$$

or, using the fact that $\bar{u} = p(u)$,

$$\dot{\theta}(t) = z(\theta(t), u(t)), \tag{4.21}$$

where $\theta = [\theta_2, \theta_3, ..., \theta_i, ..., \theta_{l-1}]^T \in \mathbb{R}^{n \times 1}$ is the value of $\theta(\hat{\rho}, t)$ at the $n = l - 2$ interior nodes, $g, z \in \mathbb{R}^{(l-2) \times 1}$ are nonlinear functions of the states, inputs and

the model parameters, $\bar{u} = [u_\eta, u_1, u_2, ..., u_6, u_{bs}, I_p]^T \in \mathbb{R}^{9\times 1}$ is the control input, and $u = [u_n,\ P_1,\ P_2,\ P_3,\ P_4,\ P_5,\ P_6,\ I_p]^T \in \mathbb{R}^{8\times 1}$ is the physical actuators.

4.3.1.1 Discretization for the leftmost interior node (i = 2)

Using the central finite difference formula of $O(h^2)$, the governing PDE (4.15) takes the following discrete form:

$$\begin{aligned}\dot{\theta}_2 =& h_0 u_\eta \frac{\theta_1 - 2\theta_2 + \theta_3}{(\Delta\rho)^2} + h_1 u_\eta \frac{\theta_3 - \theta_1}{2(\Delta\rho)} + h_2 u_\eta \theta_2 + f_{bs}^{'} \frac{1}{\theta_2} u_{bs} \\ & - f_{bs} \frac{1}{\theta_2^2} \frac{\theta_3 - \theta_1}{2(\Delta\rho)} u_{bs} + f_1^{'} u_1 + f_2^{'} u_2 + f_3^{'} u_3 + f_4^{'} u_4 + f_5^{'} u_5 + f_6^{'} u_6, \end{aligned} \tag{4.22}$$

where $\Delta\rho = 1/(l-1)$ is the radial stepsize. Using the left boundary condition, $\theta_1 = 0$, and factoring out the similar terms,

$$\begin{aligned}\dot{\theta}_2 =& g_1(\theta, \bar{u}) \\ =& \left(-\frac{2h_0}{(\Delta\rho)^2} + h_2 \right) u_\eta \theta_2 + f_{bs}^{'} u_{bs} \frac{1}{\theta_2} + \left(\frac{h_0 u_\eta}{(\Delta\rho)^2} + \frac{h_1 u_\eta}{2\Delta\rho} - \frac{f_{bs} u_{bs}}{2\theta_2^2 (\Delta\rho)} \right) \theta_3 \\ & + f_1^{'} u_1 + f_2^{'} u_2 + f_3^{'} u_3 + f_4^{'} u_4 + f_5^{'} u_5 + f_6^{'} u_6 \end{aligned} \tag{4.23}$$

4.3.1.2 Discretization for the inner nodes (3 ≤ i ≤ l − 2)

Using the central finite difference approximations of $O(h^2)$,

$$\begin{aligned}\dot{\theta}_i =& h_0 u_\eta \frac{\theta_{i-1} - 2\theta_i + \theta_{i+1}}{(\Delta\rho)^2} + h_1 u_\eta \frac{\theta_{i+1} - \theta_{i-1}}{2(\Delta\rho)} + h_2 u_\eta \theta_i + f_{bs}^{'} \frac{1}{\theta_i} u_{bs} \\ & - f_{bs} \frac{1}{\theta_i^2} \frac{\theta_{i+1} - \theta_{i-1}}{2(\Delta\rho)} u_{bs} + f_1^{'} u_1 + f_2^{'} u_2 + f_3^{'} u_3 + f_4^{'} u_4 + f_5^{'} u_5 + f_6^{'} u_6 \end{aligned} \tag{4.24}$$

factoring out the similar terms,

$$\begin{aligned}\dot{\theta}_i =& g_{i-1}(\theta, \bar{u}) \\ =& \left(\frac{h_0 u_\eta}{(\Delta\rho)^2} - \frac{h_1 u_\eta}{2(\Delta\rho)} + \frac{f_{bs} u_{bs}}{2(\Delta\rho)\theta_i^2}\right)\theta_{i-1} + \left(\frac{-2h_0}{(\Delta\rho)^2} + h_2\right) u_\eta \theta_i \\ &+ \left(\frac{h_0 u_\eta}{(\Delta\rho)^2} + \frac{h_1 u_\eta}{2(\Delta\rho)} - \frac{f_{bs} u_{bs}}{2\theta_i^2(\Delta\rho)}\right)\theta_{i+1} + f_{bs}^{'} u_{bs} \frac{1}{\theta_i} \\ &+ f_1^{'} u_1 + f_2^{'} u_2 + f_3^{'} u_3 + f_4^{'} u_4 + f_5^{'} u_5 + f_6^{'} u_6 \end{aligned} \tag{4.25}$$

4.3.1.3 Discretization for the rightmost interior node (i = l − 1)

Using the central finite difference approximations of $O(h^2)$,

$$\begin{aligned}\dot{\theta}_{l-1} =& h_0 u_\eta \frac{\theta_{l-2} - 2\theta_{l-1} + \theta_l}{(\Delta\rho)^2} + h_1 u_\eta \frac{\theta_l - \theta_{l-2}}{2(\Delta\rho)} + h_2 u_\eta \theta_{l-1} + f_{bs}^{'} \frac{1}{\theta_{l-1}} u_{bs} \\ &- f_{bs} \frac{1}{\theta_{l-1}^2} \frac{\theta_l - \theta_{l-2}}{2(\Delta\rho)} u_{bs} + f_1^{'} u_1 + f_2^{'} u_2 + f_3^{'} u_3 + f_4^{'} u_4 + f_5^{'} u_5 + f_6^{'} u_6 \end{aligned} \tag{4.26}$$

and substituting the left boundary condition, $\theta_l = -f_b I_p$, and factoring out the similar terms,

$$\begin{aligned}\dot{\theta}_{l-1} =& g_{l-2}(\theta, \bar{u}) \\ =& \left(-\frac{2h_0}{(\Delta\rho)^2} + h_2\right) u_\eta \theta_{l-1} + f_{bs}^{'} u_{bs} \frac{1}{\theta_{l-1}} + \left(\frac{h_0 u_\eta}{(\Delta\rho)^2} - \frac{h_1 u_\eta}{2\Delta\rho} + \frac{f_{bs} u_{bs}}{2\theta_{l-1}^2(\Delta\rho)}\right)\theta_{l-2} \\ &+ \left(\frac{-h_0 u_\eta}{(\Delta\rho)^2} - \frac{h_1 u_\eta}{2(\Delta\rho)} + \frac{f_{bs} u_{bs}}{2(\Delta\rho)\theta_{l-1}^2}\right) f_b I_p + f_1^{'} u_1 + f_2^{'} u_2 + f_3^{'} u_3 \\ &+ f_4^{'} u_4 + f_5^{'} u_5 + f_6^{'} u_6 \end{aligned} \tag{4.27}$$

4.3.2 Model Linearization

Let $\theta_r(t)$ and $\bar{u}_r(t)$ define a set of plasma states and corresponding control inputs satisfying the reduced-order model (4.20), i.e.,

$$\dot{\theta}_r = g(\theta_r, \bar{u}_r). \tag{4.28}$$

To obtain a model suitable for control design, we define the following perturbation values

$$\Delta\theta(t) = \theta(t) - \theta_r(t), \tag{4.29}$$

$$\Delta\bar{u}(t) = \bar{u}(t) - \bar{u}_r(t), \tag{4.30}$$

where $\Delta\theta(t)$ is the deviation from $\theta_r(t)$, and $\Delta\bar{u}(t)$ is the to-be-designed feedback control. A first-order Taylor series expansion of equation (4.20) can be written around θ_r and $\bar{u}_r$ as

$$\dot{\theta} = g(\theta_r, \bar{u}_r) + \left.\frac{\partial g}{\partial \theta}\right|_{\theta_r, \bar{u}_r} (\theta - \theta_r) + \left.\frac{\partial g}{\partial \bar{u}}\right|_{\theta_r, \bar{u}_r} (\bar{u} - \bar{u}_r). \tag{4.31}$$

By substituting (4.29) and (4.30) into (4.31),

$$\Delta\dot{\theta} + \dot{\theta}_r = g(\theta_r, \bar{u}_r) + \left.\frac{\partial g}{\partial \theta}\right|_{\theta_r, \bar{u}_r} \Delta\theta \; + \left.\frac{\partial g}{\partial \bar{u}}\right|_{\theta_r, \bar{u}_r} \Delta\bar{u}, \tag{4.32}$$

and using (4.28), it is possible to obtain a Linear, Time-Variant (LTV), state-space model for the perturbation dynamics as

$$\Delta\dot{\theta}(t) = A(t)\Delta\theta(t) + B(t)\Delta\bar{u}(t) \; , \tag{4.33}$$

where the system jacobians are expressed compactly as

$$A(t) = \left.\frac{\partial g}{\partial \theta}\right|_{\theta_r(t),\bar{u}_r(t)} \in \mathbb{R}^{(l-2)\times(l-2)} \tag{4.34}$$

$$B(t) = \left.\frac{\partial g}{\partial \bar{u}}\right|_{\theta_r(t),\bar{u}_r(t)} \in \mathbb{R}^{(l-2)\times 9} \tag{4.35}$$

In control point of view, $A(t)$ is called the "*state matrix*" and $B(t)$ is called the "*input matrix*". The elements of the system matrices $A(t)$ and $B(t)$ for the leftmost node $i = 2$ then become

$$\begin{aligned}
A_{1,1}(t) =& \left.\frac{\partial g_1}{\partial \theta_2}\right|_{\theta_r(t),\bar{u}_r(t)} \\
=& \left(-\frac{2h_0}{(\Delta\rho)^2} + h_2\right) u_{\eta_r}(t) - f_{bs}^{'} u_{bs_r}(t) \frac{1}{\theta_{2_r}^2(t)} + \frac{f_{bs} u_{bs_r}(t)\theta_{3_r}(t)}{\theta_{2_r}^3(t)(\Delta\rho)} && (4.36) \\
A_{1,2}(t) =& \left.\frac{\partial g_1}{\partial \theta_3}\right|_{\theta_r(t),\bar{u}_r(t)} \\
=& \frac{h_0 u_{\eta_r}(t)}{(\Delta\rho)^2} + \frac{h_1 u_{\eta_r}(t)}{2\Delta\rho} - \frac{f_{bs} u_{bs_r}(t)}{2\theta_{2_r}^2(t)(\Delta\rho)} && (4.37) \\
B_{1,1}(t) =& \left.\frac{\partial g_1}{\partial u_\eta}\right|_{\theta_r(t),\bar{u}_r(t)} \\
=& \left(\frac{-2h_0}{(\Delta\rho)^2} + h_2\right) \theta_{2_r}(t) + \left(\frac{h_0}{(\Delta\rho)^2} + \frac{h_1}{2\Delta\rho}\right) \theta_{3_r}(t) && (4.38) \\
B_{1,2}(t) =& \left.\frac{\partial g_1}{\partial u_1}\right|_{\theta_r(t),\bar{u}_r(t)} \\
=& f_1^{'} \qquad \text{similarly,} && (4.39) \\
B_{1,3}(t) =& f_2^{'}, \quad B_{1,4}(t) = f_3^{'}, \quad B_{1,5}(t) = f_4^{'}, \quad B_{1,6}(t) = f_5^{'}, \quad B_{1,7}(t) = f_6^{'}, && (4.40) \\
B_{1,8}(t) =& \left.\frac{\partial g_1}{\partial u_{bs}}\right|_{\theta_r(t),\bar{u}_r(t)} \\
=& f_{bs}^{'} \frac{1}{\theta_{2_r}(t)} - \frac{f_{bs}\theta_{3_r}(t)}{2\theta_{2_r}^2(t)\Delta\rho} && (4.41) \\
B_{1,9}(t) =& \left.\frac{\partial g_1}{\partial I_p}\right|_{\theta_r(t),\bar{u}_r(t)} = 0 && (4.42)
\end{aligned}$$

Similarly, the elements of the system matrices for the interior region $3 \leq i \leq l-2$ are given by

$$
\begin{aligned}
A_{i-1,i-2}(t) =& \left.\frac{\partial g_{i-1}}{\partial \theta_{i-1}}\right|_{\theta_r(t),\bar{u}_r(t)} \\
=& \left(\frac{h_0}{(\Delta\rho)^2} - \frac{h_1}{2(\Delta\rho)}\right) u_{\eta_r}(t) + \frac{f_{bs} u_{bs_r}(t)}{2\theta_{i_r}^2(t)\Delta\rho} \qquad (4.43) \\
A_{i-1,i-1}(t) =& \left.\frac{\partial g_{i-1}}{\partial \theta_i}\right|_{\theta_r(t),\bar{u}_r(t)} \\
=& -\frac{f_{bs} u_{bs_r}(t)}{\theta_{i_r}^3(t)\Delta\rho}\theta_{i-1,r}(t) + \left(\frac{-2h_0}{(\Delta\rho)^2} + h_2\right) u_{\eta_r}(t) \\
&+ \frac{f_{bs} u_{bs_r}(t)}{\theta_{i_r}^3(t)\Delta\rho}\theta_{i+1,r}(t) - f_{bs}^{'} u_{bs_r}(t)\frac{1}{\theta_{i_r}^2(t)} \qquad (4.44) \\
A_{i-1,i}(t) =& \left.\frac{\partial g_{i-1}}{\partial \theta_{i+1}}\right|_{\theta_r(t),\bar{u}_r(t)} \\
=& \left(\frac{h_0}{(\Delta\rho)^2} + \frac{h_1}{2(\Delta\rho)}\right) u_{\eta_r}(t) - \frac{f_{bs} u_{bs_r}(t)}{2\theta_{i_r}^2(t)\Delta\rho} \\
B_{i-1,1}(t) =& \left.\frac{\partial g_{i-1}}{\partial u_\eta}\right|_{\theta_r(t),\bar{u}_r(t)} \\
=& \left(\frac{h_0}{(\Delta\rho)^2} - \frac{h_1}{2(\Delta\rho)}\right)\theta_{i-1,r}(t) + \left(\frac{-2h_0}{(\Delta\rho)^2} + h_2\right)\theta_{i_r}(t) \\
&+ \left(\frac{h_0}{(\Delta\rho)^2} + \frac{h_1}{2(\Delta\rho)}\right)\theta_{i+1,r}(t) \qquad (4.45) \\
B_{i-1,2}(t) =& \left.\frac{\partial g_{i-1}}{\partial u_1}\right|_{\theta_r(t),\bar{u}_r(t)} \\
=& f_1^{'} \qquad \text{similarly,} \qquad (4.46) \\
B_{i-1,3}(t) =& f_2^{'}, \quad B_{i-1,4}(t) = f_3^{'}, \quad B_{i-1,5}(t) = f_4^{'}, \quad B_{i-1,6}(t) = f_5^{'}, \\
B_{i-1,7}(t) =& f_6^{'}, \qquad (4.47) \\
B_{i-1,8}(t) =& \left.\frac{\partial g_{i-1}}{\partial u_{bs}}\right|_{\theta_r(t),\bar{u}_r(t)} \\
=& \frac{f_{bs}}{2\theta_{i_r}^2(t)\Delta\rho}\left(\theta_{i-1,r}(t) - \theta_{i+1,r}(t)\right) + f_{bs}^{'}\frac{1}{\theta_{i_r}(t)} \qquad (4.48) \\
B_{i-1,9}(t) =& \left.\frac{\partial g_{i-1}}{\partial I_p}\right|_{\theta_r(t),\bar{u}_r(t)} = 0 \qquad (4.49)
\end{aligned}
$$

Finally, the elements of the system matrices for the rightmost node $i = l - 1$ are

$$
\begin{aligned}
A_{l-2,l-3}(t) =& \left.\frac{\partial g_{l-2}}{\partial \theta_{l-2}}\right|_{\theta_r(t),\bar{u}_r(t)} \\
=& \left(\frac{h_0}{(\Delta\rho)^2} - \frac{h_1}{2(\Delta\rho)}\right) u_{\eta_r}(t) + \frac{f_{bs}}{2(\Delta\rho)\theta_{l-1,r}^2(t)} u_{bs_r}(t) \qquad (4.50) \\
A_{l-2,l-2}(t) =& \left.\frac{\partial g_{l-2}}{\partial \theta_{l-1}}\right|_{\theta_r(t),\bar{u}_r(t)} \\
=& \left(\frac{-2h_0}{(\Delta\rho)^2} + h_2\right) u_{\eta_r}(t) - f_{bs}^{'} \frac{u_{bs_r}(t)}{\theta_{l-1,r}^2(t)} - \frac{f_{bs} u_{bs_r}(t)\theta_{l-2,r}(t)}{\theta_{l-1,r}^3(t)(\Delta\rho)} \\
& - \frac{f_{bs} u_{bs_r}(t) f_b I_{p_r}(t)}{(\Delta\rho)\theta_{l-1,r}^3(t)} \qquad (4.51) \\
B_{l-2,1}(t) =& \left.\frac{\partial g_{l-2}}{\partial u_\eta}\right|_{\theta_r(t),\bar{u}_r(t)} \\
=& \left(\frac{-2h_0}{(\Delta\rho)^2} + h_2\right) \theta_{l-1,r}(t) + \left(\frac{h_0}{(\Delta\rho)^2} - \frac{h_1}{2(\Delta\rho)}\right) \theta_{l-2,r}(t) \\
& + \left(\frac{-h_0}{(\Delta\rho)^2} - \frac{h_1}{2(\Delta\rho)}\right) f_b I_{p_r}(t) \qquad (4.52) \\
B_{l-2,2}(t) =& \left.\frac{\partial g_{l-2}}{\partial u_1}\right|_{\theta_r(t),\bar{u}_r(t)} \\
=& f_1^{'} \qquad \text{similarly,} \qquad (4.53) \\
B_{l-2,3}(t) =& f_2^{'}, \quad B_{l-2,4}(t) = f_3^{'}, \quad B_{l-2,5}(t) = f_4^{'}, \quad B_{l-2,6}(t) = f_5^{'}, \quad B_{l-2,7}(t) = f_6^{'} \\
B_{l-2,8}(t) =& \left.\frac{\partial g_{l-2}}{\partial u_{bs}}\right|_{\theta_r(t),\bar{u}_r(t)} \\
=& f_{bs}^{'} \frac{1}{\theta_{l-1,r}(t)} + \frac{f_{bs}\theta_{l-2,r}(t)}{2(\Delta\rho)\theta_{l-1,r}^2(t)} + \frac{f_{bs} f_b I_{p_r}(t)}{2(\Delta\rho)\theta_{l-1,r}^2(t)} \qquad (4.54) \\
B_{l-2,9}(t) =& \left.\frac{\partial g_{l-2}}{\partial I_p}\right|_{\theta_r(t),\bar{u}_r(t)} \\
=& \left(\frac{-h_0 u_{\eta_r}(t)}{(\Delta\rho)^2} - \frac{h_1 u_{\eta_r}(t)}{2(\Delta\rho)} + \frac{f_{bs} u_{bs_r}(t)}{2(\Delta\rho)\theta_{l-1,r}^2(t)}\right) f_b \qquad (4.55)
\end{aligned}
$$

Note that all unspecified elements of $A(t)$ and $B(t)$ matrices are zeros, and the small subscript "r" denotes the reference trajectories for the states and inputs.

4.4 Optimal Tracking Control Design

In this section, a multi-input-multi-output (MIMO) feedback controller is designed based on the state-space, reduced-order, control-oriented model in its time-variant (LTV) form (4.33). The control goal is to regulate the evolution of the poloidal magnetic flux gradient profile, and thus the current profile or the safety factor profile, in NSTX-U. The proposed controller is then tested in numerical simulations in MATLAB based on the full magnetic diffusion equation (2.5)-(2.6).

4.4.1 Optimal Tracking Control Problem Statement

In addition to the state equation (4.33), an output equation can be defined to provide a linear combination of the states. The overall plant is then characterized by the following LTV, MIMO system

$$\Delta\dot{\theta}(t) = A(t)\Delta\theta(t) + B(t)\Delta\bar{u}(t), \tag{4.56}$$

$$y(t) = C\Delta\theta(t), \tag{4.57}$$

where $C \in \mathbb{R}^{m\times n}$ is the output matrix and $y(t) \in \mathbb{R}^{m\times 1}$ is the output vector with $m = 9$ (number of control outputs chosen equal to the number of control inputs). The role of the matrix C is to select those states, that is, those radial points of the q-profile, where the profile control must be achieved. Hence, each row of C has only one nonzero element, which is equal to one and is located at the column associated with the state to be controlled.

Let $\theta_r(t)$ represent a target magnetic flux gradient profile corresponding to a target q-profile. The tracking problem for $\theta(t)$ then becomes a regulation problem for $\Delta\theta(t)$, since $\Delta\theta(t) = \theta(t) - \theta_r(t)$. Therefore, the control objective is to regulate the output

$y(t)$ around zero *as closely as possible* during the time interval $[t_0, t_f]$ with *minimum control effort.* This defines a standard Linear-Quadratic-Regulator (LQR) optimal control problem, the solution of which is in state-feedback form utilizing the time-varying Kalman Gain [75]. To improve the performance of the closed-loop system and reject the effect of possible disturbances, integral action should be added to the optimal control law.

4.4.2 Linear-Quadratic-Integral (LQI) Optimal Controller

The LQI optimal control problem is considered here since it adds the desired integral action to the LQR problem. To obtain the LQI controller, a new state variable, $e(t)$ is introduced to be the integral of the output $y(t)$

$$e(t) = \int_{t_0}^{t} y(\tau)\, d\tau = C \int_{t_0}^{t} \Delta\theta(\tau)\, d\tau. \tag{4.58}$$

The derivative of the integral error (4.58) then becomes

$$\dot{e}(t) = C\Delta\theta(t). \tag{4.59}$$

A new, enlarged state variable, $\widetilde{x}(t)$ can be introduced by augmenting the integral error (4.58) with the actual state, $\Delta\theta(t)$

$$\widetilde{x}(t) = \begin{bmatrix} e(t) \\ \hdashline \Delta\theta(t) \end{bmatrix}. \tag{4.60}$$

Taking the derivative of the enlarged state variable (4.60), and substituting (4.56) and (4.59), the state equation for the enlarged system can be obtained as

$$\begin{bmatrix} \dot{e}(t) \\ \Delta\dot{\theta}(t) \end{bmatrix} = \begin{bmatrix} 0 & C \\ 0 & A(t) \end{bmatrix} \begin{bmatrix} e(t) \\ \Delta\theta(t) \end{bmatrix} + \begin{bmatrix} 0 \\ B(t) \end{bmatrix} \Delta\bar{u}(t). \tag{4.61}$$

Note that (4.61) can be rewritten compactly as

$$\dot{\widetilde{x}}(t) = \widetilde{A}(t)\widetilde{x}(t) + \widetilde{B}(t)\Delta\bar{u}(t). \tag{4.62}$$

To minimize a weighted combination of the tracking error and control energy, one can consider the following standard, quadratic performance index expressed in terms of the enlarged system (4.62)

$$\begin{aligned} \min_{\Delta u(t)} J =& \frac{1}{2}\widetilde{x}^T(t_f)P(t_f)\widetilde{x}(t_f) \\ &+ \frac{1}{2}\int_{t_0}^{t_f}\left[\widetilde{x}^T(t)Q\widetilde{x}(t)+\Delta\bar{u}^T(t)R\Delta\bar{u}(t)\right]dt, \end{aligned} \tag{4.63}$$

where $P(t_f) \in \mathbb{R}^{(m+n)\times(m+n)}$, $Q \in \mathbb{R}^{(m+n)\times(m+n)}$, and $R \in \mathbb{R}^{m\times m}$ are symmetric, positive definite weight matrices. Note that the solution of the optimal control problem defined by the linear-time-variant plant, (4.62), and the quadratic performance index, (4.63), yields a time-variant state-feedback of the form

$$\Delta\bar{u}(t) = -K(t)\widetilde{x}(t), \tag{4.64}$$

where $K(t) \in \mathbb{R}^{m\times(m+n)}$ is the *Kalman Gain* given by

$$K(t) = R^{-1}\widetilde{B}^T(t)P(t), \tag{4.65}$$

and $P(t)$ is the solution of the matrix Riccatti Differential Equation (RDE)

$$\begin{aligned}\dot{P}(t) = &- \widetilde{A}^T(t)P(t) - P(t)\widetilde{A}(t) \\ &+ P(t)\widetilde{B}(t)R^{-1}\widetilde{B}^T(t)P(t) - Q,\end{aligned} \tag{4.66}$$

subject to the final condition $P(t_f)$ [75]. The optimal feedback control law $\Delta\bar{u}(t)$ for the enlarged system (4.62) then becomes

$$\begin{aligned}\Delta\bar{u}(t) = -K(t)\widetilde{x}(t) &= -[K_I(t)\ K_P(t)] \begin{bmatrix} e(t) \\ \Delta\theta(t) \end{bmatrix} \\ &= -K_I(t)e(t) - K_P(t)\Delta\theta(t).\end{aligned} \tag{4.67}$$

Finally, substituting the integral error (4.58) back into (4.67), the optimal control law can be written as

$$\begin{aligned}\Delta\bar{u}(t) = &- K_I(t)\int_{t_0}^{t} C\left[\theta(\tau) - \theta_r(\tau)\right]d\tau \\ &- K_P(t)\left[\theta(t) - \theta_r(t)\right].\end{aligned} \tag{4.68}$$

Note that the optimal solution (4.68) yields a PI (Proportional plus Integral) control law.

4.4.3 Control Signal Transformation

During the plasma control experiments in NSTX-U and numerical simulations, the control inputs $\bar{u} = [u_\eta, u_1, u_2, u_3, u_4, u_5, u_6, u_{bs}, I_p(t)]^T \in \mathbb{R}^9$ need to be converted to the physical actuators, $u = [u_n, P_1, P_2, P_3, P_4, P_5, P_6, I_p]^T \in \mathbb{R}^8$. Inversion of the non-linear transformations (4.5)-(4.8) produce the following expressions for the physical

actuators

$$\hat{P}_{tot} = \left(\frac{u_{bs}}{u_\eta I_p} \right), \tag{4.69}$$

$$\hat{u}_n = u_{bs} u_\eta^{-1/3}, \tag{4.70}$$

$$\hat{P}_i = u_i I_p \sqrt{\hat{P}_{tot}}, \quad i = 1, 2, \ldots, 6. \tag{4.71}$$

$$\hat{I}_p = I_p. \tag{4.72}$$

Note however that the inverse transformations (4.69)-(4.72) along with the constraint $\hat{P}_{tot} = \hat{P}_1 + \hat{P}_2 + \hat{P}_3 + \hat{P}_4 + \hat{P}_5 + \hat{P}_6$ form a set of over-constrained equations, all of which cannot be satisfied simultaneously. To determine the beam power requests, one needs to solve the best approximation to the over-determined system governed by

$$X_{LS} \underbrace{[P_1\, P_2\, P_3\, P_4\, P_5\, P_6]^T}_{P_{\rm req}} = \underbrace{\left[\hat{P}_1\, \hat{P}_2\, \hat{P}_3\, \hat{P}_4\, \hat{P}_5\, \hat{P}_6\, \hat{P}_{\rm tot}\right]^T}_{\hat{P}} \tag{4.73}$$

where P_{req} represents the actuator power requests to be determined. The 7 by 6 matrix X_{LS} is defined as $X_{LS}^T = [I_6\ \mathbf{1}]$ where I_6 denotes a 6 by 6 identity matrix and $\mathbf{1}$ represents an additional column of ones. The solution of (4.73) requires solving the minimization problem

$$P_{\rm req} = \arg\min_{P_{\rm req}} \left(\hat{P} - X_{LS} P_{\rm req} \right)^T Q_{LS} \left(\hat{P} - X_{LS} P_{\rm req} \right), \tag{4.74}$$

where Q_{LS} is a diagonal weighting matrix. The solution of (4.74) can be written as $P_{req} = (Q_{LS} X_{LS})^+ Q_{LS} \hat{P}$, where the superscript $(^+)$ denotes the pseudoinverse.

The block diagram in Fig. 4.1 summarizes the closed-loop LQI control scheme for NSTX-U. T refers to the nonlinear input transformations (4.5)-(4.8). The block

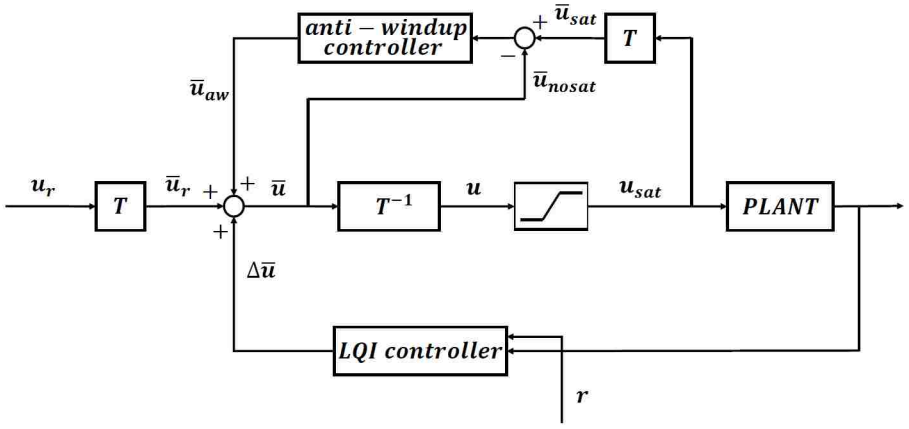

Figure 4.1: Closed-loop LQI control scheme showing the nonlinear control signal transformation.

T^{-1} refers to the the nonlinearity inversion (4.69)-(4.74) carried out to determine the actuator power requests. The saturation block and the anti-windup controller are also depicted in Fig. 4.1.

4.5 Performance Assessment of the LQI Optimal Controller via Closed-Loop Control-oriented Nonlinear Simulations

In this section, results of closed-loop q-profile tracking control simulations are provided to illustrate the performance of the proposed control algorithm. The controller is designed based on the LTV, state-space model (4.33) tailored for NSTX-U. Although NSTX-U has been operating since the second half of 2015, there is still not enough experimental data accumulated yet to tailor a reliable model for control design. Therefore, the model reference profiles and constants are adopted based on numerical predictions by TRANSP. In this work, NSTX-U TRANSP run 121123R42 [17] has been

selected for model tailoring since it is a TRANSP run with the NSTX-U shape and actuators, but using scaled profiles from NSTX. The designed controller is then tested in closed-loop simulations carried out by simulating the nonlinear MDE (2.5)-(2.6).

Two different closed-loop control simulations are carried out in this section to analyze the initial condition perturbation rejection and disturbance rejection capabilities of the proposed controller. For each case, the target state trajectories, $\theta_r(\hat{\rho}, t)$ are generated by simulating the MDE (2.5)-(2.6) with the physical inputs set to arbitrary constants. Both for control design and closed-loop simulation, the non-dimensional spatial domain ($\hat{\rho} \in [0\ 1]$) is divided into $l = 21$ radial nodes, hence, the radial grid size is $\Delta\hat{\rho} = 0.05$. Control simulations are then carried out for $t \in [t_0\ t_f] = [0.1\ 5]$ s., which is a typical discharge duration expected for NSTX-U. The controller sampling time is set to $T_s = 0.05$ s.

The tuning of the proposed LQI optimal controller (4.68) is important for the closed-loop control performance. The tuning problem involves the selection of the weight matrices Q and R, which are the two free parameters of the control design. Since the inputs are normalized and the states have the same order of magnitude, both Q and R are selected as diagonal matrices, each having identical diagonal entries. The ratio between Q and R defines how the trade-off between speed of response and consumption of control energy is weighted. For the two simulation cases in this section, the terminal cost matrix, $P(t_f)$ in (4.63) is set to identity to ensure the tracking error at the final time t_f is equally weighted for all states.

In the first closed-loop control simulation study, the initial condition perturbation rejection capability is tested by setting $\theta(t_0) = \theta_r(t_0) + \delta\theta$. The controller is tuned by setting the ratio between Q and R to 1000. This value has been found to be effective in minimizing the tracking error at the expense of a larger control effort within tolerable saturation margins. The simulation results for this case are summarized in Fig. 4.2

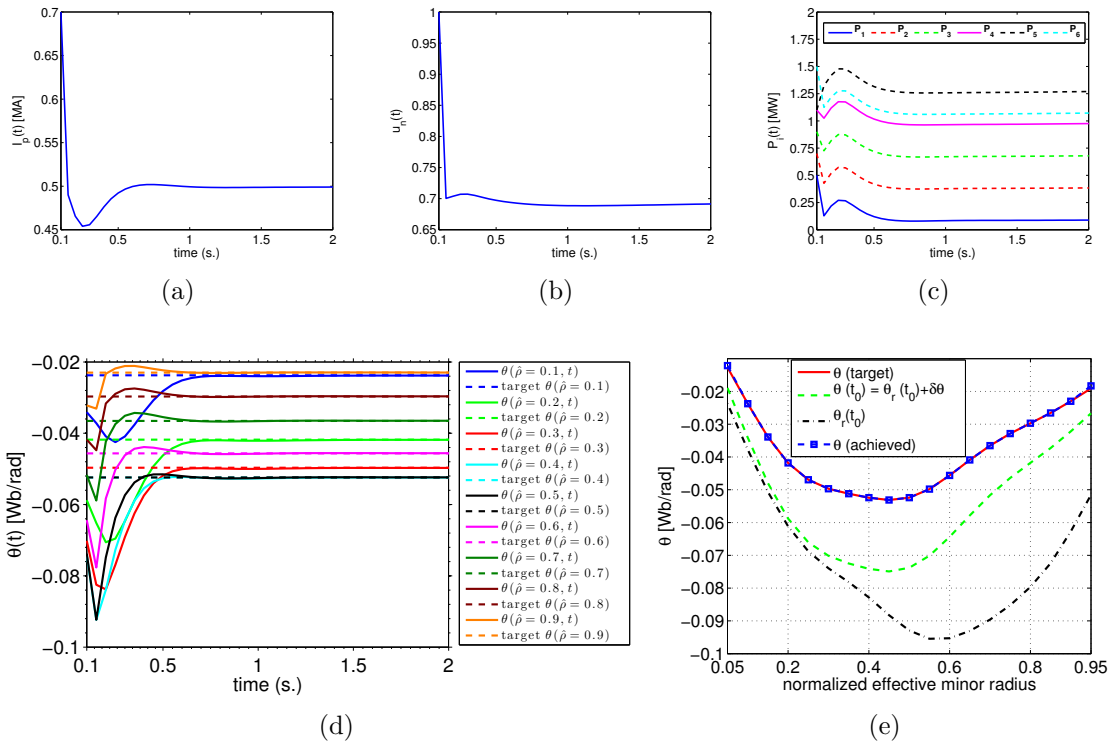

Figure 4.2: Tracking simulation results for the first case: (a)-(c) Time evolution of the optimal plasma current, electron density regulation and neutral beam injection (NBI) powers; (d) Time evolution of the optimal outputs (solid) with their respective targets (dashed); (e) Comparison of the initial and desired $\theta(\hat{\rho})$ profiles along with the profile achieved by feedback control at $t = 2$ s.

for the first 2 s. of the discharge. The time evolution of the optimal physical inputs, namely, the total plasma current, electron density and neutral beam injection powers are illustrated in Figs. 4.2(a)-(c), respectively. The corresponding time evolution of the optimal outputs ($\theta(t)$ values at various plasma radial locations) are depicted in Fig. 4.2(d) along with their respective targets. As can be seen from Fig. 4.2(d), the outputs are regulated around their desired values within the first 2 seconds of the discharge. Fig. 4.2(e) compares the $\theta(\hat{\rho})$ profile achieved at $t = 2$ s. with the desired target profile along with the actual (unperturbed) initial profile, $\theta_r(t_0)$, and the perturbed initial profile, $\theta(t_0)$. Fig. 4.2(e) shows that the desired target profile is achieved at $t = 2$ s., but it is possible to note from Fig. 4.2(d) that an excellent

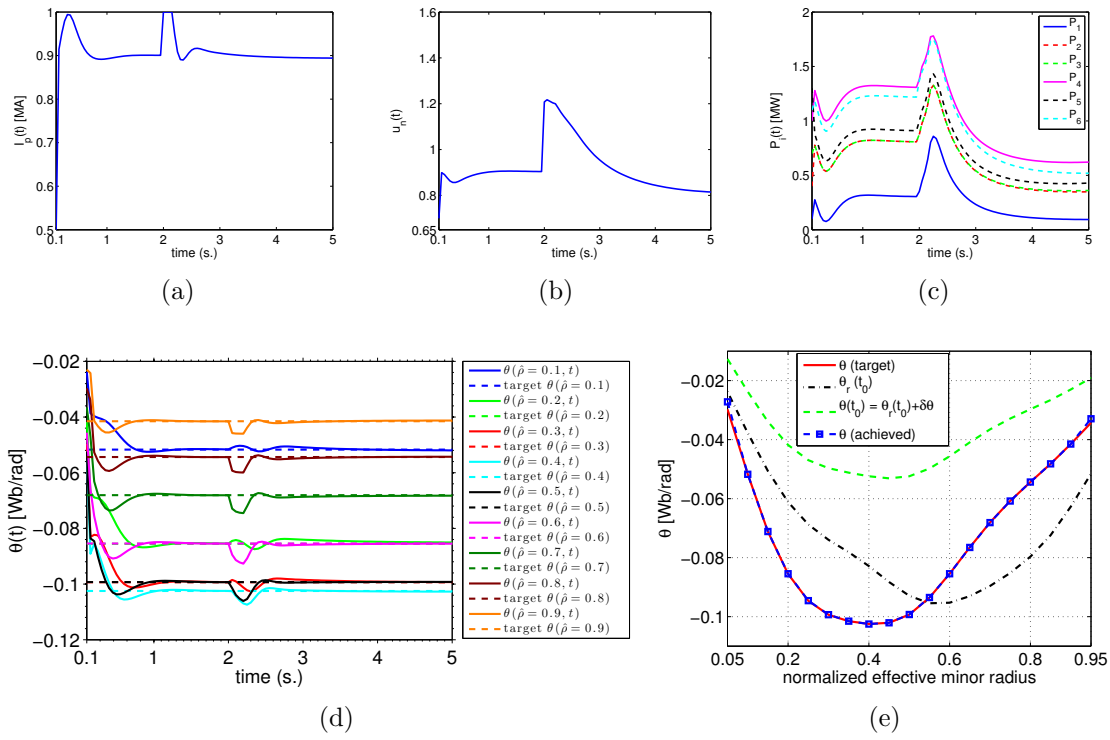

Figure 4.3: Tracking simulation results for the second case: (a)-(c) Time evolution of the optimal plasma current, electron density regulation and NBI powers; (d) Time evolution of the optimal outputs (solid) with their respective targets (dashed); (e) Comparison of the initial and desired $\theta(\hat{\rho})$ profiles along with the profile achieved at t=5 s.

profile matching is already achieved well before $t = 2$ s.

In the second closed-loop control simulation study, the disturbance rejection capability is tested. A different target profile is tracked and in addition to an initial condition perturbation, step disturbances are also added in each input channel starting from $t = 2$ s. i.e.,

$$u(t) = \begin{cases} \Delta u(t) + u_r(t), & t \leq 2\,\text{s}. \\ \Delta u(t) + u_r(t) + u_d, & t > 2\,\text{s}. \end{cases} \tag{4.75}$$

where u_d stands for the constant disturbance inputs (0.25 MA for the plasma current, 0.1 MW for each neutral beam injection power and 0.3 for the electron density regulation). The controller is tuned by setting the ratio between Q and R to 10000, seeking in this way a faster response. The results of the second closed-loop simulation

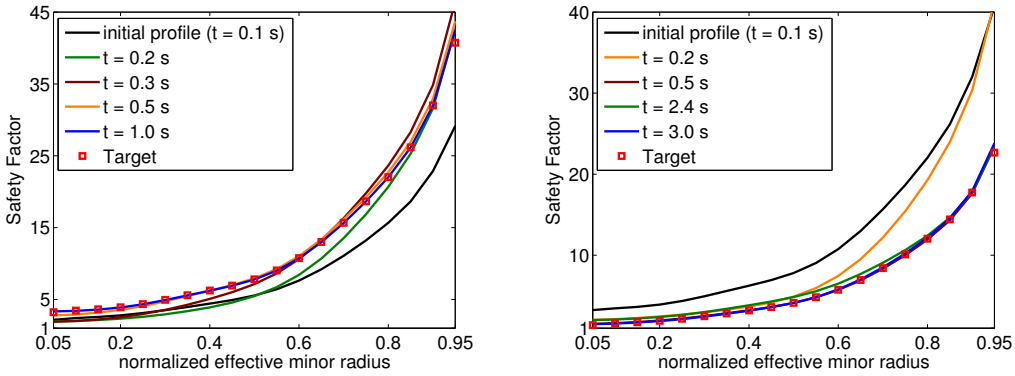

(a) First case (b) Second case

Figure 4.4: Time evolutions of the safety factor (q-profiles) corresponding to (a) first case (i.e., Fig. 4.2) and (b) second case (i.e., Fig. 4.3).

case are summarized in Fig. 4.3. The time evolution of the optimal physical inputs are illustrated in Figs. 4.3(a)-(c). The corresponding time evolution of the optimal outputs are depicted in Fig. 4.3(d) along with their respective targets. Note from Fig. 4.3(d) that the states jump again at $t = 2$ s., which is the effect of the step disturbance inputs added at that instant. Fig. 4.3(e) compares the $\theta(\hat{\rho})$ profile achieved at $t = 5$ s. with the desired target profile along with the actual (unperturbed) initial profile, $\theta_r(t_0)$, and the perturbed initial profile, $\theta(t_0)$. While Fig. 4.3(e) shows that the desired target profile is achieved at $t = 5$ s., an excellent profile matching is already achieved well before $t = 5$ s. as can be seen from Fig. 4.3(d).

Finally, time evolutions of the corresponding safety factor (q-profiles) are compared for both cases in Fig. 4.4 along with their respective initial and target profiles. Fig. 4.4(a) corresponds to the first case (i.e., Fig. 4.2), for which the initial q-profile (black solid line) is below the target q-profile (red squared line). On the other hand, Fig. 4.4(b) corresponds to the second case (i.e., Fig. 4.3), for which the initial q-profile (black solid line) is above the target q-profile (red squared line). Based on this simulation analysis, the proposed controller is shown to be effective in regulating the q-profile around a predefined target profile in NSTX-U.

4.6 Performance Assessment of the LQI Optimal Controller via Closed-Loop TRANSP Predictive Simulations

After successfully testing the performance of the LQI controller in closed-loop numerical simulations based on the nonlinear control-oriented MDE solver, it is important to further evaluate the capability of the designed controller to deal with unmodeled dynamics. Therefore, assessment of the performance of the proposed controller in closed-loop numerical simulations based on more advanced physics codes, such as TRANSP [46], is a critical step before testing it experimentally in NSTX-U. In this section, a newly created capability of TRANSP, the so-called Expert routine [2], is used to assess the closed-loop tracking performance of the proposed LQI optimal controller.

4.6.1 Overview of TRANSP Expert Routine for Feedback Control Simulations [2]

4.6.1.1 TRANSP Computational Approach

The closed-loop predictive TRANSP simulations follow the approach outlined in [17], where the TRANSP code is used to compute in open loop the solution to the magnetic diffusion equation based on calculations of the bootstrap current, neutral beam current drive (NBCD), and free-boundary equilibrium in response to specified time-evolving inputs (plasma boundary shape, total plasma current, electron temperature profile, electron density profile, and power/voltage/geometry of the neutral beam injection system). The free boundary equilibrium is obtained by using the ISOLVER

equilibrium code within TRANSP [76, 77]. Because the ion heat transport is reasonably well described by neoclassical theory, the Chang-Hinton model is used to model the dynamics of the ion temperature. However, due to the lack of well validated models, electron temperature and density profiles are not modeled by first principles calculations in these TRANSP simulations. Instead, the electron density profile is adopted from experimental measurements in NSTX and scaled to achieve a particular Greenwald fraction [78, 79]

$$f_{\mathrm{GW}} = \frac{\bar{n}_e \pi a^2}{I_p}, \tag{4.76}$$

where a is the plasma minor radius and I_p is the total plasma current. The ion density profile is calculated by assuming a flat $Z_{eff} = 2$ profile with carbon as the only impurity. The electron temperature profile is also adopted from experimental measurements and scaled to achieve a particular global confinement level. The NBCD is computed via the NUBEAM code [80] and the bootstrap current is calculated by using the Sauter model [68].

4.6.1.2 Modifications for Closed-Loop Simulations

The TRANSP computational approach followed in [17] and described in the previous section must be modified to enable closed-loop simulations within the TRANSP source code. First, instead of scanning density and temperature profiles to achieve particular Greenwald fractions and confinement levels, closed-loop simulations must be constrained to follow a specific confinement level and a prescribed Greenwald fraction (or particle inventory) at all time, even when parameters like the plasma current, plasma density and beam powers are varied, either by feedforward or feedback controllers. This requires that the temperature and density profiles used in TRANSP ad-

just appropriately when the actuator (plasma current, plasma density, beam powers) waveforms are modified based on requests by the feedforward or feedback controllers. Secondly, unlike the open-loop version of TRANSP, where the actuator waveforms must be specified before initiating the simulation, closed-loop TRANSP simulations require that the actuator requests be updated online based on the changing plasma parameters and the computations by the feedback control algorithm. Therefore, the feedback control module must communicate with TRANSP to calculate the new input data based on the "real-time measurements" of the plasma state.

4.6.1.3 Description of the Expert Routine

The necessary modifications to enable feedback control simulations in TRANSP have been implemented through the so-called Expert routine. The Expert routine provides a framework for the user to enter the designed controller as well as reference inputs and state trajectories into the TRANSP environment. It interrupts the standard (open-loop) operation of the TRANSP code at each time step to recalculate the actuator requests according to the implemented feedback control law and the current plasma state. The basic communication flow between TRANSP and the Expert routine is shown in Fig. 4.5. At the beginning of each TRANSP transport time step, the Expert routine is called and it performs the following modifications through its four main modules:

- The *electron density module* supplies an electron density profile to the TRANSP source code at the beginning of each transport time step according to [2]

$$n_e(\hat{\rho}, t) = n_{e,0}(t) n_e^{ref}(\hat{\rho}), \tag{4.77}$$

  where, $n_e^{ref}(\hat{\rho})$ is a user-supplied reference electron density shape, extracted

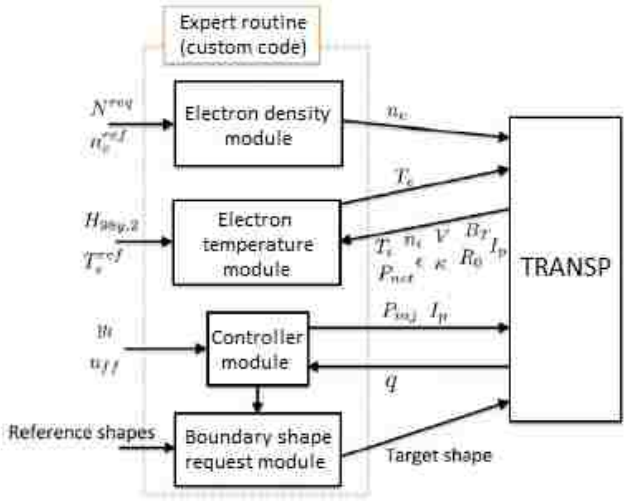

Figure 4.5: Operational flow of the Expert routine [2].

from experiments in a way similar to that explained in Section 2.3.1. The time-dependent term $n_{e,0}(t)$ in (4.77) scales the shape of the reference profile to ensure that the particle inventory, N, follows a conservation equation. The desired particle inventory, $N^{req}(t)$, can be simply a function of time or can be calculated to achieve a predefined line-averaged density, $\bar{n}_e(t)$, or Greenwald fraction waveform f_{GW}. At the start of each TRANSP transport time step (covering the time interval (t_a, t_b)), the desired inventory N^{req} is calculated and the applied particle inventory is evolved according to

$$N_b = N_a + (t_b - t_a)(N^{req} - N_a)/\tau_N, \tag{4.78}$$

where $\tau_N = 0.1$ s. is an approximate density confinement time (a few multiples of the energy confinement time, approximately). Finally, the scale factor $n_{e,0}$ at time t_b is calculated as

$$n_{e,0} = \frac{N_b}{\int_0^1 n_e^{ref} \frac{\partial V}{\partial \hat{\rho}} d\hat{\rho}}. \tag{4.79}$$

- The *electron temperature module* works similarly to the electron density module and supplies an electron temperature profile to the TRANSP source code at the beginning of each transport time step according to the formula

$$T_e(\hat{\rho}, t) = T_{e,0}(t) T_e^{ref}(\hat{\rho}), \tag{4.80}$$

where $T_e^{ref}(\hat{\rho})$ is a reference electron temperature shape obtained from NSTX experiments. The time-dependent term $T_{e,0}(t)$ in (4.80) is a scaling factor used to achieve a certain electron temperature that can maintain the stored plasma energy predicted by a zero-dimensional energy balance. At each time step, $T_{e,0}$ is computed as

$$T_{e,0} = \frac{\frac{3}{2}\langle E_{\rm th}\rangle - \langle n_i T_i\rangle}{\langle n_e T_e^{ref}\rangle}, \tag{4.81}$$

where n_i and T_i (ion density and ion temperature) together with n_e (electron density) are obtained from TRANSP (Fig. 4.5). The volume-averaged stored energy, $\langle E_{\rm th}\rangle = \frac{W_{th}}{V} = \frac{3}{2}\big[T_{e,0}\langle n_e T_e^{ref}\rangle + \langle n_i T_i\rangle\big]$, is obtained at each transport time step (covering the time interval (t_a, t_b)) from the discretized power balance

$$W_{th,b} = W_{th,a} + (t_b - t_a)\big(-\frac{W_{th,a}}{\tau_E} + P_{net}\big) \tag{4.82}$$

where τ_E is the confinement time and P_{net} is the net heating source. The energy confinement time τ_E is computed based on one of two different scalings. The first is the $H_{98y,2}$ scaling [81], given by

$$\tau_{98y,2} = H_{98y,2}\, 0.0562\, I_p^{0.93} B_T^{0.15} \bar{n}_e^{0.41} P_{\rm Loss,th}^{-0.69} R_0^{1.97} \epsilon^{0.58} \kappa^{0.78}. \tag{4.83}$$

The second is a ST scaling [82] given by

$$\tau_{ST} = H_{ST}\, 0.1178\, I_p^{0.57}\, B_T^{1.08}\, \bar{n}_e^{0.44}\, P_{\mathrm{Loss,th}}^{-0.73}. \tag{4.84}$$

In both scalings, the toroidal magnetic field (B_T), line-averaged electron density ($\bar{n}_e$), thermal loss power ($P_{\mathrm{Loss,th}}$), plasma major radius (R_0), inverse aspect ratio (ϵ), and plasma elongation (κ) are obtained from TRANSP (see Fig. 4.5), while the confinement factors $H_{98y,2}$ or H_{ST} are interpolated from a user-supplied waveform.

- The *controller module* computes the input data at each transport time step based on the safety factor (q-profile) or rotational transform (ι-profile) extracted from TRANSP, the user-supplied control law, the target states (y_t, which corresponds to θ_r in this work), and the feedforward actuator trajectory (u_{ff}, which corresponds to u_r in this work). The computed actuator requests (input data) for the next transport time calculation are sent to TRANSP as shown in Fig. 4.5.

- The *boundary shape request module* utilizes the free boundary equilibrium code ISOLVER [76, 77] in 'least-squares mode' so far. In this mode, the coil currents are calculated at each time step to best fit a prescribed plasma boundary [2]. At the beginning of each magnetic geometry calculation step, just after the inputs to ISOLVER are set up, the boundary shape request module is called and the existing plasma boundary reference and total plasma current value are replaced with the values requested by the control algorithm (Fig. 4.5).

4.6.2 LQI Control Redesign based on a Full Linear Model of the Rotational Transform Profile Dynamics

To simplify the implementation of the developed controller in the Expert routine, the nonlinear control signal inversions (4.69)-(4.74) can be avoided when conducting closed-loop control simulations in TRANSP. This is achieved by further linearizing the reduced-order model (4.20) around the reference physical actuators, u_r. Hence, starting from the reduced-order model

$$\dot{\theta} = g\left(\theta, \bar{u}\right), \tag{4.85}$$

where $\bar{u} = p(u)$, a first-order Taylor series expansion of (4.85) can be written around θ_r and u_r as

$$\dot{\theta} = g\left(\theta_r, p(u_r)\right) + \left.\frac{\partial g}{\partial \theta}\right|_{\theta_r, u_r} (\theta - \theta_r) + \left.\frac{\partial g}{\partial p}\frac{\partial p}{\partial u}\right|_{\theta_r, u_r} (u - u_r). \tag{4.86}$$

By substituting the perturbation values $\Delta\theta = \theta - \theta_r$ and $\Delta u = u - u_r$ into (4.86) we can write

$$\Delta\dot{\theta} + \dot{\theta}_r = g\left(\theta_r, p(u_r)\right) + \left.\frac{\partial g}{\partial \theta}\right|_{\theta_r, u_r} \Delta\theta + \left.\frac{\partial g}{\partial p}\frac{\partial p}{\partial u}\right|_{\theta_r, u_r} \Delta u, \tag{4.87}$$

and using the fact that $\dot{\theta}_r = g\left(\theta_r, p(u_r)\right)$, it is possible to obtain a Linear, Time-Variant (LTV), state-space model for the deviation dynamics as

$$\Delta\dot{\theta}(t) = \widehat{A}(t)\Delta\theta(t) + \widehat{B}(t)\Delta u(t)\ , \tag{4.88}$$

where the system Jacobians are expressed compactly as

$$\widehat{A}(t) = \left.\frac{\partial g}{\partial \theta}\right|_{\theta_r(t), u_r(t)}, \qquad \widehat{B}(t) = \left.\frac{\partial g}{\partial p}\frac{\partial p}{\partial u}\right|_{\theta_r(t), u_r(t)}. \tag{4.89}$$

After the initial ramp-up phase of the plasma discharge, u_r and θ_r remain approximately constant. Therefore, the system dynamics (4.88) can be further approximated by the linear-time-invariant (LTI) model

$$\Delta\dot{\theta}(t) = A\Delta\theta(t) + B\Delta u(t) \ , \tag{4.90}$$

where $A = \widehat{A}(t_s)$, $B = \widehat{B}(t_s)$, and t_s is some time during the flat-top phase of the discharge. Note that the rotational transform (ι-profile) and the poloidal flux gradient profile $\theta(\hat{\rho}, t) = \partial\psi/\partial\hat{\rho}$ are related through (2.4). Hence, the LTI model (4.90) for $\Delta\theta$ can be converted into an LTI model for $\Delta\iota$ as

$$\Delta i(t) = \overline{A}\Delta\iota(t) + \overline{B}\Delta u(t) \ , \tag{4.91}$$

where $\overline{A} = T^{-1}AT$, $\overline{B} = T^{-1}B$, and the transformation matrix is defined as

$$T = -\text{diag}(B_0\rho_b^2\hat{\rho}_i) \ , \quad i = 1, 2, ..., n \tag{4.92}$$

where $\hat{\rho}_i = i(\Delta\hat{\rho})$. In addition to the state equation (4.91), an output equation can be defined to provide a linear combination of the states. The fully linearized ι-profile response model then becomes

$$\Delta i(t) = \overline{A}\Delta\iota(t) + \overline{B}\Delta u(t), \tag{4.93}$$

$$y(t) = \overline{C}\Delta\iota(t), \tag{4.94}$$

where $\overline{C} \in \mathbb{R}^{8\times n}$ is the same output matrix C as in (4.57).

The LQI optimal controller for the ι-model (4.93)-(4.94) is designed in the same way as in Section 4.4.2. In this case, the optimal feedback control law, $\Delta u(t)$, could

be written in terms of a PI-controller with time-invariant (constant) gains, i.e.,

$$\Delta u(t) = -K_I \int_{t_0}^{t} C\Delta\iota(\tau)d\tau - K_P\Delta\iota(t), \tag{4.95}$$

where $K = [K_I \;\; K_P] = R^{-1}\widetilde{B}^T P_+$, with P_+ being the unique positive definite solution to the Algebraic Ricatti Equation (ARE) [75]

$$0 = -\widetilde{A}^T P_+ - P_+\widetilde{A} + P_+\widetilde{B}R^{-1}\widetilde{B}^T P_+ - Q, \tag{4.96}$$

where the constant enlarged matrices are

$$\widetilde{A} = \begin{bmatrix} 0 & \overline{C} \\ 0 & \overline{A} \end{bmatrix}, \quad \widetilde{B} = \begin{bmatrix} 0 \\ \overline{B} \end{bmatrix}. \tag{4.97}$$

4.6.3 Closed-loop TRANSP Simulation Results

The LQI controller is designed based on the fully-linear, time-invariant, state-space model (4.93)-(4.94) following the procedure outlined in Section 4.6.2. The target (or reference) state trajectory $\iota_r(\hat{\rho}, t)$ is generated through the open-loop TRANSP run 142301W12, with the physical inputs set to the following arbitrary constants

$$\begin{aligned} u_r(t) = u_r &= [\bar{n}_e \quad P_1 \quad P_2 \quad P_3 \quad P_4 \quad P_5 \quad P_6 \quad I_p]^T \\ &= \left[5\times 10^{19} \;\; 0.2 \;\; 0.4 \;\; 0.6 \;\; 0.8 \;\; 1.0 \;\; 1.2 \;\; 0.7\right]^T, \end{aligned} \tag{4.98}$$

where the line-averaged density $\bar{n}_e$ is in m^{-3}, the beam powers $P_1, \ldots, P_6$ are in MW, and the plasma current I_p is in MA. The initial condition ($\iota_r(\hat{\rho}, 0)$) is shown in Figs. 4.6(i)-(j), Figs. 4.7(k)-(l), and Fig 4.11(a)-(b). The designed LQI controller is then tested in closed-loop simulations in TRANSP, through the Expert Routine. Both for control design and closed-loop simulation, the non-dimensional spatial domain

($\hat{\rho} \in [0\ 1]$) is divided into $l = 21$ radial nodes, hence, the radial grid size is $\Delta\hat{\rho} = 0.05$. Control simulations are carried out for $t \in [t_0\ t_f] \triangleq [0\ 4]$ s. The sampling time is set to $T_s = 0.01$ s. Both the initial condition perturbation and input disturbance rejection capabilities are tested by setting

$$u(t) = \begin{cases} u_r + u_d, & t < 1\,\text{s}. \\ \Delta u(t) + u_r + u_d, & t \geq 1\,\text{s}. \end{cases} \tag{4.99}$$

where u_d stands for the constant disturbance inputs (15% of the reference for the plasma current, 10% of the reference for the beam powers). Feedback controller is turned on at $t = 1$ s. and is tuned by setting the ratio between Q and R to 10000, seeking in this way a faster response.

4.6.3.1 Plasma-current and Neutral-beam Actuation

For the two simulations provided in Fig. 4.6 (in the right and left columns, respectively), the total plasma current and the six neutral beam injectors are used as actuators. The plasma line-averaged density is not actuated in this simulation study and is fixed at the reference value. The plots in the left column correspond to the simulation study without current rate limit. Hence, a sudden drop is observed in the time evolution of the optimal plasma current in Fig. 4.6(a), which makes it difficult to implement in the real NSTX-U machine. The plots in the right column correspond to the same simulation case but with a current rate limit ($|dI_p/dt| = 0.75$ MA/s) to avoid the unrealistic sudden drop in I_p. Figs. 4.6(a)-(b) show the time evolution of the optimal plasma current. Figs. 4.6(c)-(d) show the time evolution of the optimal beam powers. The corresponding evolutions of the optimal outputs (i.e., the time evolution of the ι at various plasma radii) are shown in Fig 4.6(e)-(h). Finally, Figs. 4.6(i)-(j) compare actual and reference $\iota(\hat{\rho})$ profiles achieved at different instants in time.

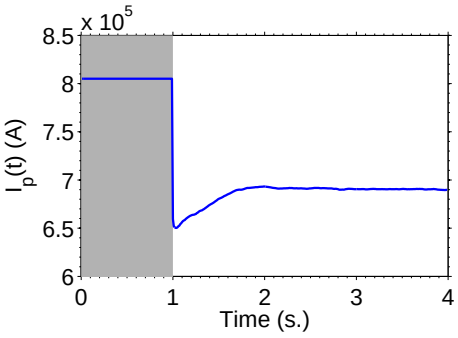
x 10^5
I_p(t) (A)
Time (s.)

(a)

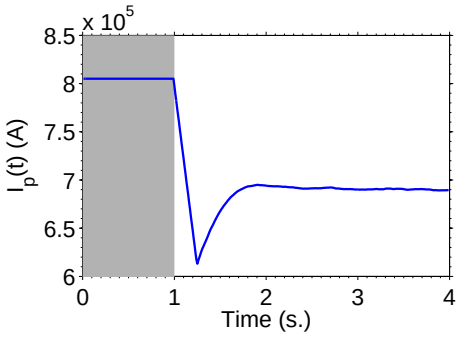
x 10^5
I_p(t) (A)
Time (s.)

(b)

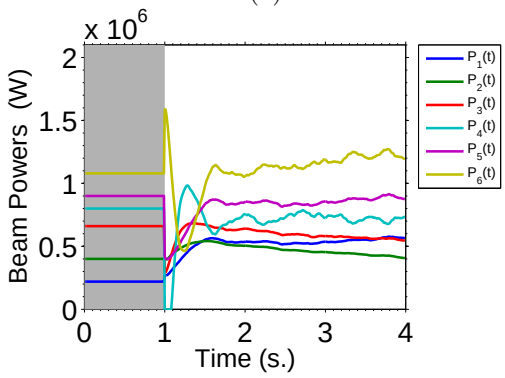
x 10^6
Beam Powers (W)
Time (s.)
P_1(t)
P_2(t)
P_3(t)
P_4(t)
P_5(t)
P_6(t)

(c)

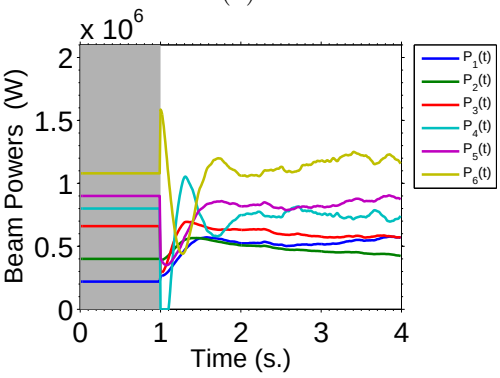
x 10^6
Beam Powers (W)
Time (s.)
P_1(t)
P_2(t)
P_3(t)
P_4(t)
P_5(t)
P_6(t)

(d)

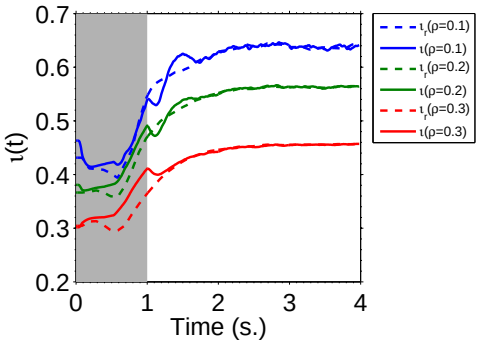
ι(t)
Time (s.)
ι_r(ρ=0.1)
ι(ρ=0.1)
ι_r(ρ=0.2)
ι(ρ=0.2)
ι_r(ρ=0.3)
ι(ρ=0.3)

(e)

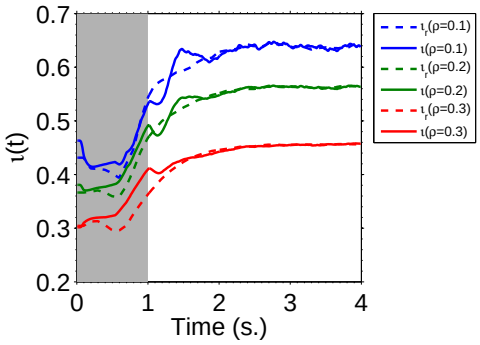
ι(t)
Time (s.)
ι_r(ρ=0.1)
ι(ρ=0.1)
ι_r(ρ=0.2)
ι(ρ=0.2)
ι_r(ρ=0.3)
ι(ρ=0.3)

(f)

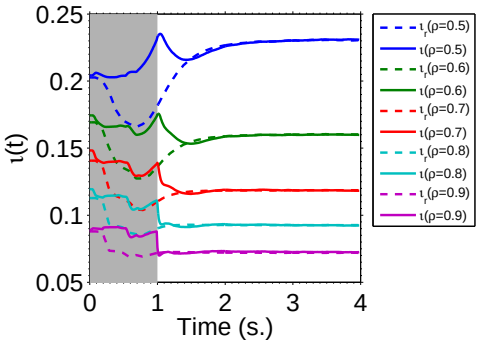
ι(t)
Time (s.)
ι_r(ρ=0.5)
ι(ρ=0.5)
ι_r(ρ=0.6)
ι(ρ=0.6)
ι_r(ρ=0.7)
ι(ρ=0.7)
ι_r(ρ=0.8)
ι(ρ=0.8)
ι_r(ρ=0.9)
ι(ρ=0.9)

(g)

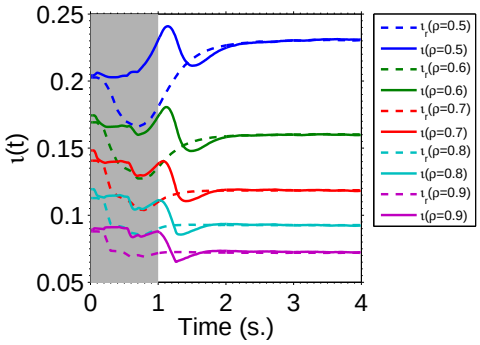
ι(t)
Time (s.)
ι_r(ρ=0.5)
ι(ρ=0.5)
ι_r(ρ=0.6)
ι(ρ=0.6)
ι_r(ρ=0.7)
ι(ρ=0.7)
ι_r(ρ=0.8)
ι(ρ=0.8)
ι_r(ρ=0.9)
ι(ρ=0.9)

(h)

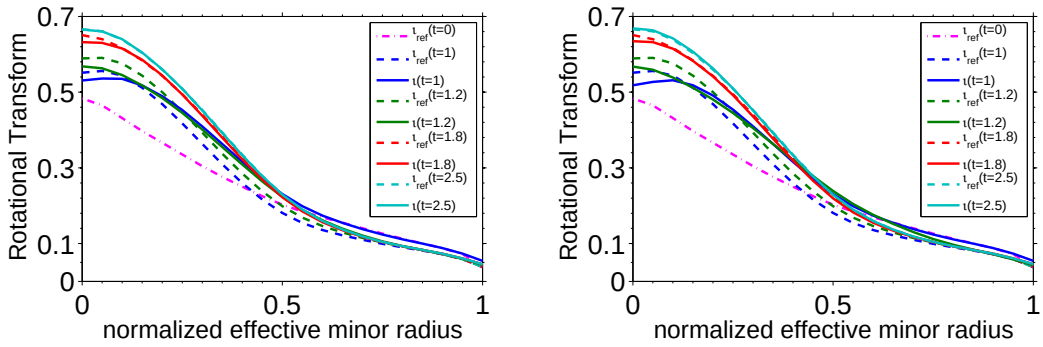

(i) (j)

Figure 4.6: Feedback control simulation results from TRANSP with (right column) and without (left column) the I_p rate saturation: (a)-(b) Time evolution of the optimal plasma current, (c)-(d) time evolution of the optimal beam powers, (e)-(h): time evolution of the optimal outputs (solid) with their respective targets (dashed). (i)-(j): time evolution of the rotational transform (ι-profile). Note that controller is off in the grey region.

Fig. 4.6(a) shows a sudden drop in the plasma current when the controller is turned on. However, this is difficult to implement in the real NSTX-U machine since the rate of change of the actuators are always limited. The sharp drop in I_p is eliminated in Fig. 4.6(b) by imposing a rate limit at the the expense of a slower transient response in Figs. 4.6(f)-(h) when compared to Figs. 4.6(e)-(g). Figs. 4.6(i)-(j) compare reference (unperturbed) and actual (perturbed) profiles at $t = 1$ s. The difference between $\iota_{\text{ref}}(t = 1)$ and $\iota(t = 1)$ is the consequence of introducing input perturbations for $t \in [0, 1]$ without feedback control. This difference can also be appreciated in Figs. 4.6(e)-(h). Despite this difference, the feedback controller is able to start tracking the reference profile after it is turned on at $t = 1$ s., showing almost perfect tracking one second later (after $t = 2$ s.).

4.6.3.2 Density, Plasma-current and Neutral-beam Actuation

For the two simulations provided in Fig. 4.7, in addition to the total plasma current and the six neutral-beam powers, the line-averaged electron density is also used as an

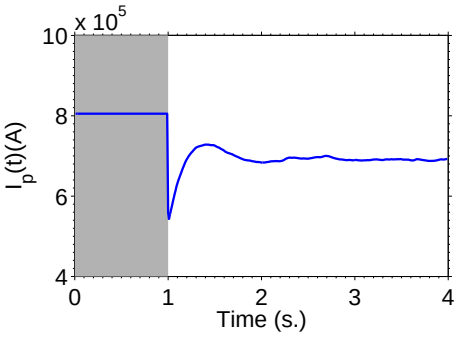
x 10^5
I_p(t)(A)
Time (s.)

(a)

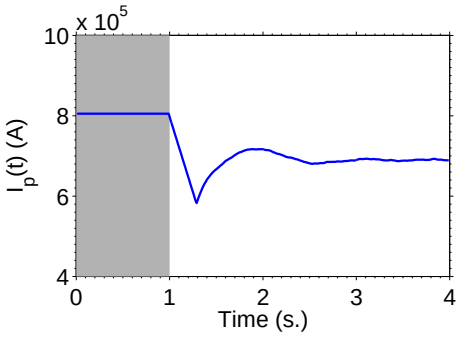
x 10^5
I_p(t) (A)
Time (s.)

(b)

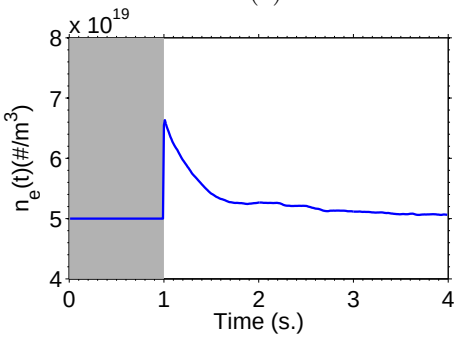
x 10^19
n_e(t)(#/m^3)
Time (s.)

(c)

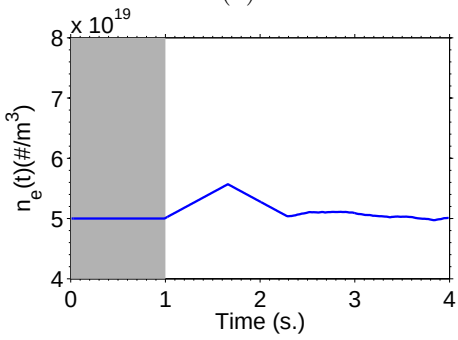
x 10^19
n_e(t)(#/m^3)
Time (s.)

(d)

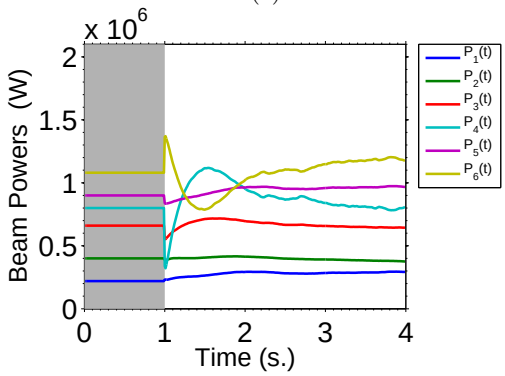
x 10^6
Beam Powers (W)
Time (s.)
P_1(t)
P_2(t)
P_3(t)
P_4(t)
P_5(t)
P_6(t)

(e)

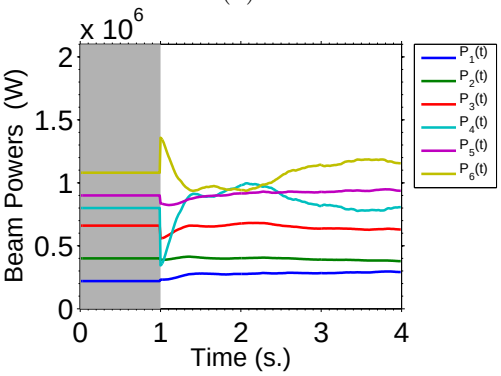
x 10^6
Beam Powers (W)
Time (s.)
P_1(t)
P_2(t)
P_3(t)
P_4(t)
P_5(t)
P_6(t)

(f)

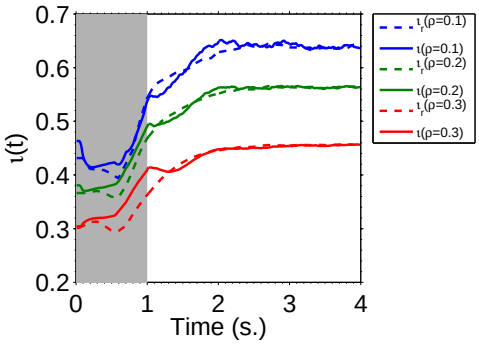
ι(t)
Time (s.)
ι_r(ρ=0.1)
ι(ρ=0.1)
ι_r(ρ=0.2)
ι(ρ=0.2)
ι_r(ρ=0.3)
ι(ρ=0.3)

(g)

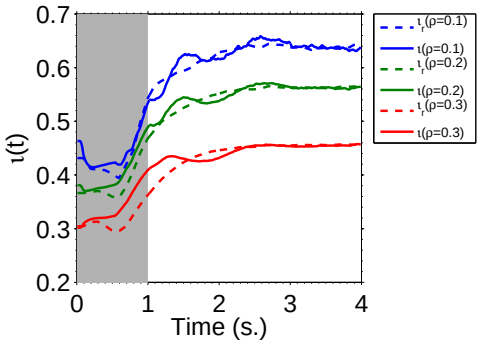
ι(t)
Time (s.)
ι_r(ρ=0.1)
ι(ρ=0.1)
ι_r(ρ=0.2)
ι(ρ=0.2)
ι_r(ρ=0.3)
ι(ρ=0.3)

(h)

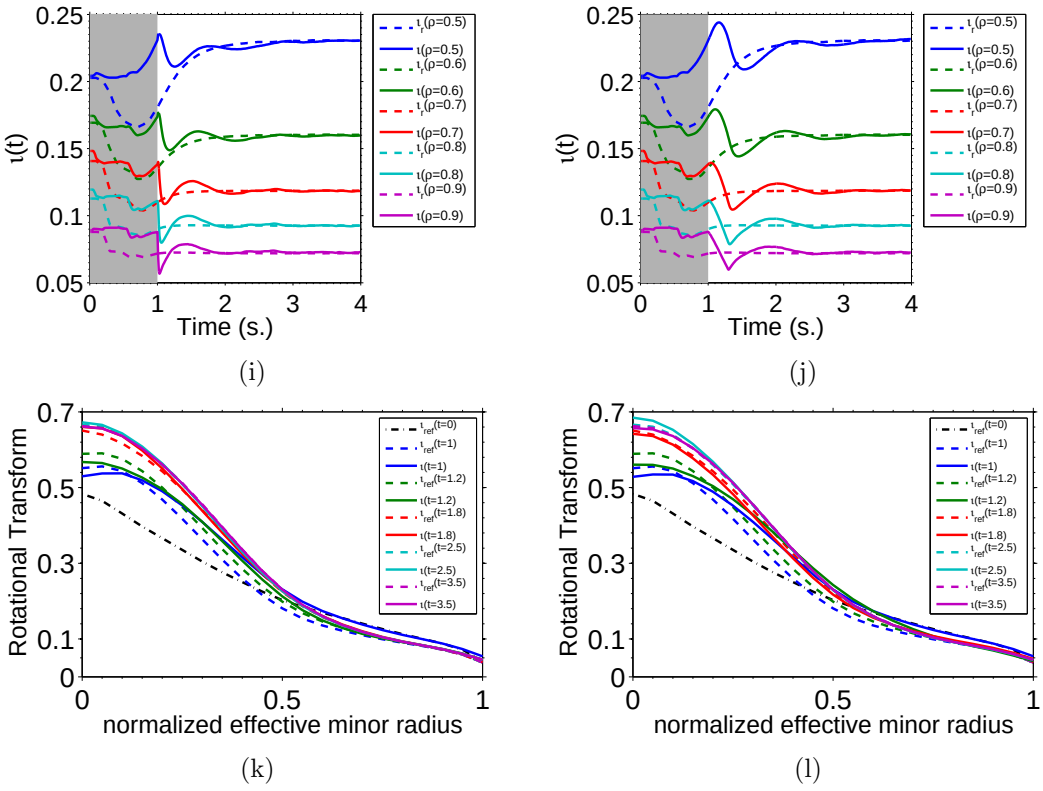

Figure 4.7: Feedback control simulation results from TRANSP with (right column) and without (left column) the I_p and n_e rate saturation: (a)-(b) Time evolution of the optimal plasma current, (c)-(d) time evolution of the optimal line-averaged density, (e)-(f) time evolution of the optimal beam powers, (g)-(j): time evolution of the optimal outputs (solid) with their respective targets (dashed). (k)-(l): time evolution of the rotational transform (ι-profile). Note that controller is off in the grey region.

actuator. The figures in the left column correspond to the simulation study without current and density rate limits. Hence, a sudden drop is observed in the time evolution of the optimal plasma current in Fig. 4.7(a), whereas a sudden increase in electron density is observed in Fig. 4.7(c). The figures in the right column correspond to the same simulation case but with rate limits given by $|dI_p/dt| = 0.75$ MA/s and $|d\bar{n}_e/dt| = 0.85 \times 10^{19}$ m^{-3}s^{-1}. Figs. 4.7(a)-(b) show the time evolution of the optimal plasma current, Figs. 4.7(c)-(d) show the time evolution of the optimal line-averaged electron density, Figs. 4.7(e)-(f) show the time evolution of the optimal beam powers. The corresponding evolutions of the optimal outputs are shown in Fig 4.7(g)-(j).

Finally, Figs. 4.7(k)-(l) compare actual and reference $\iota(\hat{\rho})$ profiles at different instants of time. As in the previous simulation case, the controller is able to achieve almost perfect tracking of the reference profile shortly after it is turned on at $t = 1$ s. This simulation study shows that the proposed controller is capable of utilizing all physical actuators, including plasma density, to effectively regulate the ι-profile around a target profile in NSTX-U.

4.6.3.3 Rejection of Confinement Changes

In these predictive TRANSP simulations, the n_e and T_e profile evolutions are not modeled by first-principles calculations. Instead, a reference n_e profile is specified based on an NSTX experimental profile and then eventually scaled to achieve a particular Greenwald fraction f_{GW} [2]. Similarly, a reference T_e profile is also taken from an experiment and scaled to achieve a particular global confinement time [82]

$$\tau_{ST} = H_{ST}\, 0.1178\, I_p^{0.57}\, B_T^{1.08}\, n_e^{0.44}\, P_{\mathrm{Loss,th}}^{-0.73}, \tag{4.100}$$

where H_{ST} is the confinement factor, I_p is the plasma current in MA, B_T is the toroidal magnetic field in T, n_e is the line-averaged electron density in $\#/m^3 \times 10^{19}$ and $P_{\mathrm{Loss,th}}$ is the loss power in MW [2].

When performing closed-loop simulations in TRANSP, the simulation must be constrained to follow a specific confinement level all the time although the actuators are varied based on the calculations of the feedback controller. This is achieved by manipulating the confinement factor H_{ST} through a user-defined waveform [2]. However, the H_{ST} factor can deviate from the user-supplied waveform, which creates an additional source of disturbance.

In this section, two closed-loop TRANSP simulations are carried out to assess the

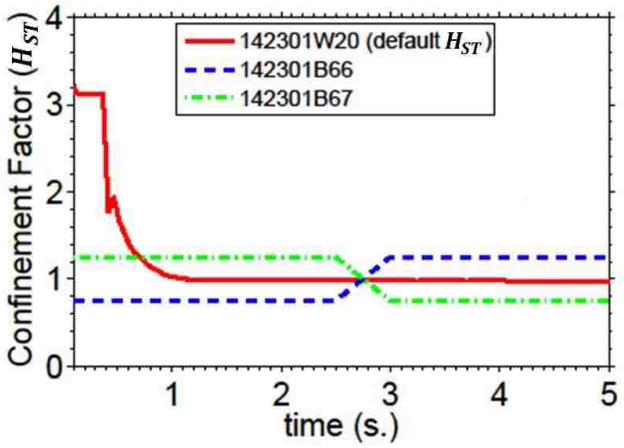

Figure 4.8: Time evolution of the confinement factor, H_{ST} for the two closed-loop TRANSP runs for testing the disturbance rejection capability.

disturbance rejection capability of the controller against changes in the confinement factor (Fig. 4.8):

1. Run 142301B66 has a step increase in the H_{ST} from 0.75 to 1.25.

2. Run 142301B67 has a step decrease in the H_{ST} from 1.25 to 0.75.

Note that in addition to the variations in the H_{ST} factor, the same constant input disturbances as in sections 4.6.3.1 and 4.6.3.2 are also acting throughout the whole simulation for both cases. The artificial variations in the H_{ST} factor represent the possible confinement variations in NSTX-U experiments. Both runs utilize the proposed LQI optimal controller, and only plasma current and neutral-beam powers are used as actuators without considering rate limits. The line-averaged density remains at its reference value during the simulations. Note that the target ι-profile corresponds to the open-loop run 142301W20, which has an almost constant confinement factor during the period of time the controller is on ($H_{ST} \approx 1$ for $t \in [1\ 5]$ s.).

Simulation results are summarized in Fig. 4.9 for the run 142301B66 (increasing H_{ST} factor), and in Fig. 4.10 for the run 142301B67 (decreasing H_{ST} factor). Note

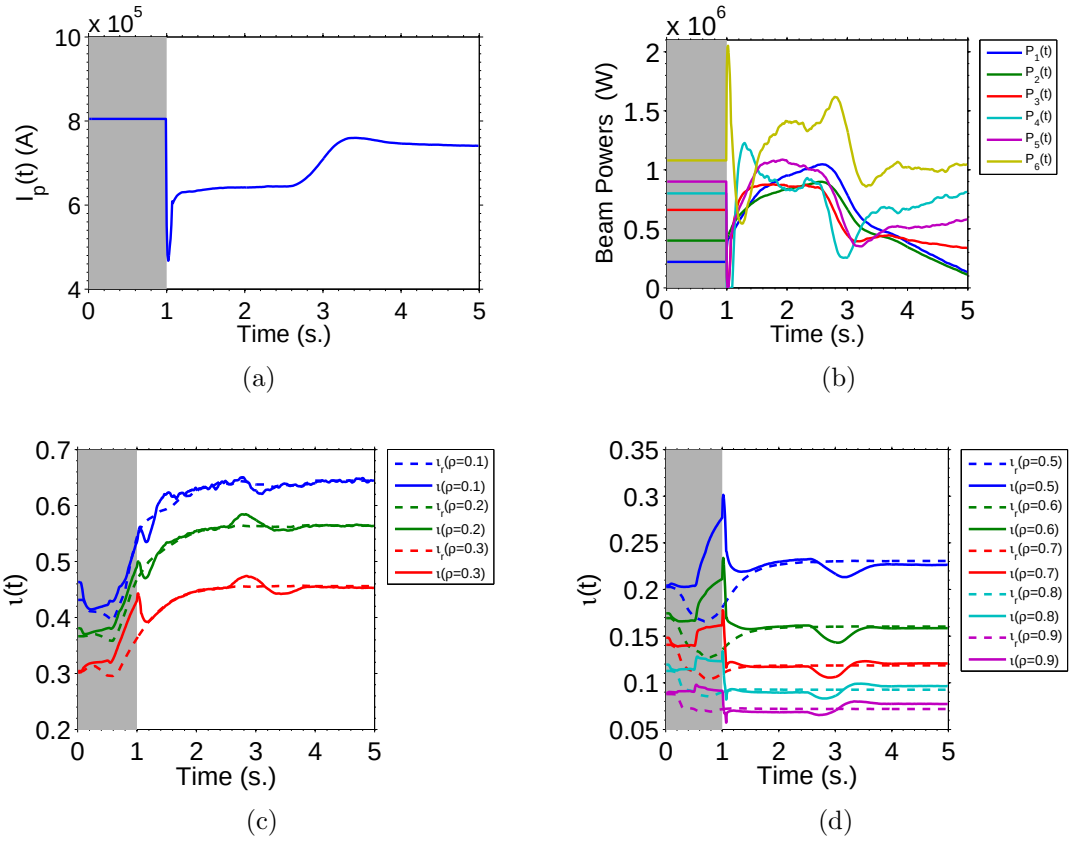

Figure 4.9: Closed-loop TRANSP simulation results against increasing H_{ST} factor (run 142301B66): Time evolution of the (a) total plasma current, (b) individual NBI powers, and (c)-(d) optimal outputs along with their respective targets. Note that controller is off in the grey region.

from the comparison of Fig. 4.9(c)-(d) and Fig. 4.10(c)-(d) that the controller is capable of rejecting the disturbances introduced by the changing confinement factor in both simulations cases. From Fig. 4.9(b) and Fig. 4.10(b), it can be noted that the NBI powers are quite sensitive to the changes in the confinement factor as they are not settling around constant values as is the case for the total plasma current evolution (Fig. 4.9(a) and Fig. 4.10(a), respectively). Finally, the time evolution of the rotational transform is depicted in Fig 4.11(a) for the 142301B66 case run (increasing H_{ST}), and in Fig. 4.11(b) for the 142301B67 case run (decreasing H_{ST}).

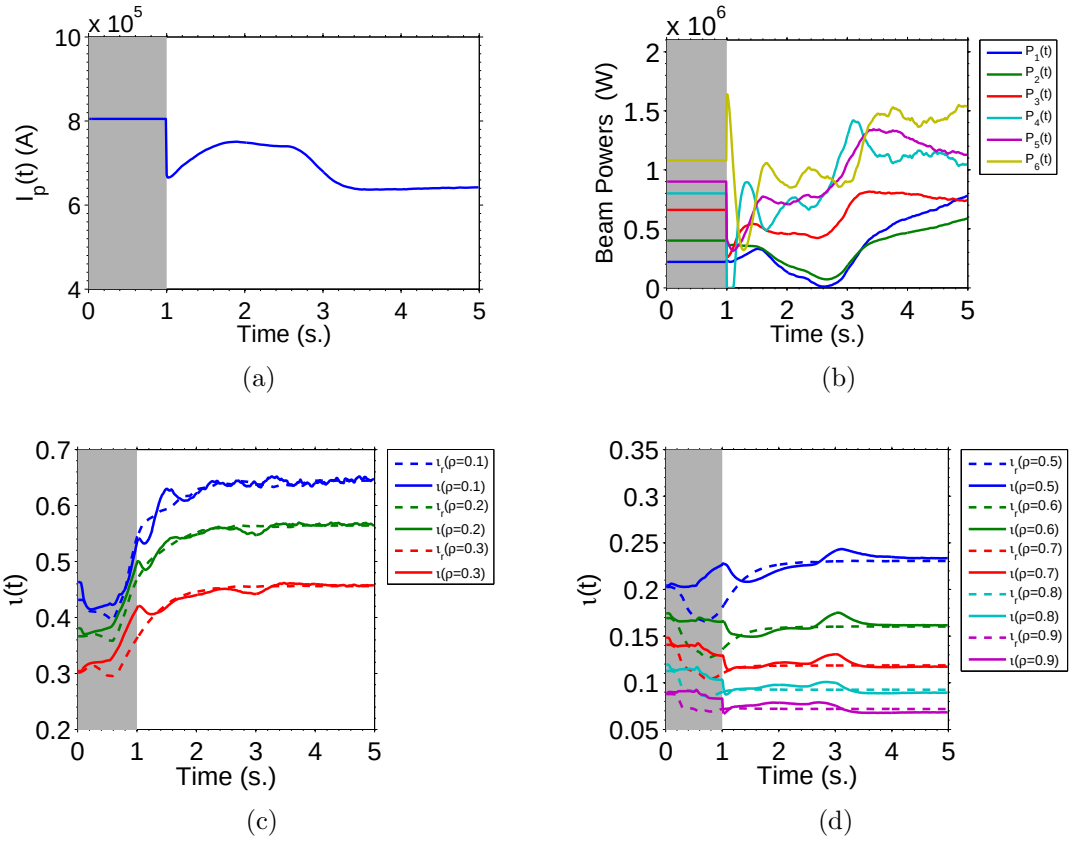

Figure 4.10: Closed-loop TRANSP simulation results against decreasing H_{ST} factor (run 142301B67): Time evolution of the (a) total plasma current, (b) individual NBI powers, and (c)-(d) optimal outputs along with their respective targets. Note that controller is off in the grey region.

4.7 Conclusion

In this chapter, an NSTX-U-tailored plasma response model is first put into a control-oriented form. The resulting infinite dimensional, nonlinear PDE is then reduced through spatial discretization by a truncated Taylor series expansion. The nonlinear, finite-dimensional model is finally linearized around the target state and input trajectories. In this way, a state-space LTV model is obtained describing the perturbation dynamics around the target trajectories. An LQI feedback controller is designed based on this proposed control-oriented, state-space LTV model to regulate

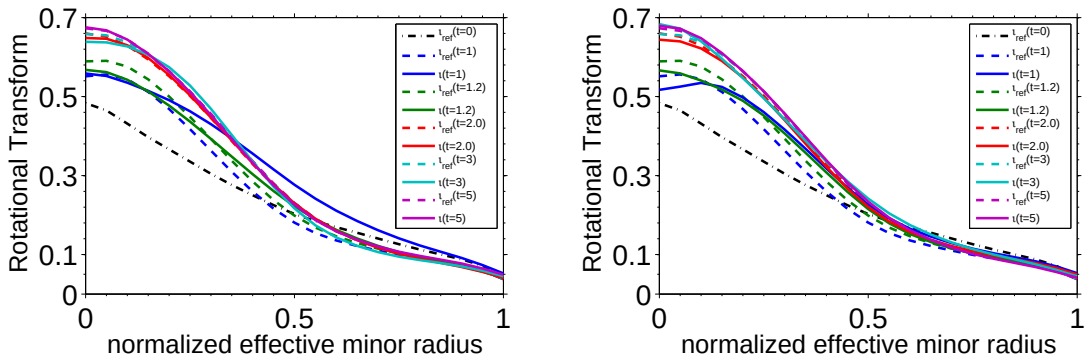

Figure 4.11: Time evolution of the ι-profiles in (a) closed-loop TRANSP run with the increasing H_{ST} factor (142301B66), and (b) closed-loop TRANSP run with the decreasing H_{ST} factor (142301B67).

the poloidal flux gradient profile, and hence the current profile or the safety factor profile, around a desired target profile. The effectiveness of the proposed controller in shaping the poloidal flux gradient profile is first tested in closed-loop numerical simulations based on the control-oriented MDE solver. The proposed LQI control strategy is tested later in closed-loop predictive simulations in TRANSP through the recently developed Expert routine. To simplify the implementation of the controller in the Expert routine a time-invariant control law is sought. Therefore, the proposed LQI controller is redesigned based on a linear time-invariant (LTI) state space model of the rotational transform profile evolution in NSTX-U, which is obtained by evaluating the state matrices of the LTV model at a given time during the flattop phase. The closed-loop TRANSP simulations show that the proposed LQI optimal controller is effective in regulating the rotational transform profile around a desired profile in NSTX-U while rejecting disturbances due to modeling uncertainties and confinement-factor changes. This promising ι-profile tracking performance motivates the implementation of the proposed optimal control strategy in the actual NSTX-U device once critical diagnostics are commissioned and plasma operation starts.

Chapter 5

Model Predictive Control of the Current Density Profile Evolution in NSTX-U

5.1 Introduction

The main focus of this chapter is to develop for the first time a Model Predictive Control (MPC) strategy to regulate the rotational transform profile around a desired target profile in NSTX-U. The nonlinear, control-oriented, physics-based model describing the temporal evolution of the rotational transform profile in NSTX-U is first put into a constrained MPC formulation. An integrator is embedded into the MPC formulation to provide offset-free tracking in the presence of modeling uncertainties and external disturbances. The neutral beam powers, electron density, and total plasma current are used as control actuators to manipulate the profile shape. The effectiveness of the proposed controller in shaping the ι-profile is shown in closed-loop simulations based on the nonlinear control-oriented MDE solver.

This chapter is organized as follows. A brief overview of the standard MPC strategy is provided in Section 5.2. A constrained MPC problem with integral action is formulated for rotational transform profile tracking in NSTX-U in Section 5.3. The performance of the proposed integral MPC strategy is evaluated via closed-loop nonlinear simulations in Section 5.4. Finally, conclusions are provided in Section 5.5.

5.2 Overview of MPC[1]

Model Predictive Control (MPC) is an optimal control strategy based on numerical optimization. Future control inputs and future plant responses are predicted using a system model and optimized at regular intervals with respect to a performance index. Computation of the MPC control law requires the following 3 steps:

1. Prediction
2. Optimization
3. Receding horizon implementation.

A brief description is provided below for the each step.

5.2.1 Prediction

For a discrete-time, linear system

$$x(k+1) = Ax(k) + Bu(k), \tag{5.1}$$

and a predicted input sequence, $\mathbf{u}(k)$, the corresponding sequence of state predictions, $\mathbf{x}(k)$, can be obtained by simulating the model (5.1) forward over a prediction horizon

[1] Based on the lecture notes for the C21 course on Model Predictive Control by Mark Cannon. Course page: http://www.eng.ox.ac.uk/∼conmrc/mpc

of, for instance, N sampling intervals. The stacked input and state vectors $\mathbf{u}$, $\mathbf{x}$ are defined as

$$\mathbf{u}(k) = \begin{bmatrix} u(k|k) \\ u(k+1|k) \\ \vdots \\ u(k+N-1|k) \end{bmatrix}, \quad \mathbf{x}(k) = \begin{bmatrix} x(k+1|k) \\ x(k+2|k) \\ \vdots \\ x(k+N|k) \end{bmatrix}, \tag{5.2}$$

where $u(k+i|k)$ and $x(k+i|k)$ denote input and state vectors at time $k+i$ that are predicted at time k, and $x(k+i|k)$ evolves according to the prediction model (5.1), with the initial condition at the beginning of the prediction horizon defined as

$$x(k|k) = x(k). \tag{5.3}$$

5.2.2 Optimization

The predictive control law is computed by minimizing a standard quadratic performance index defined in terms of the predicted sequences $\mathbf{x}$ and $\mathbf{u}$, i.e.

$$J(k) = \sum_{i=0}^{N-1} \left[x^T(k+i|k) Q x(k+i|k) + u^T(k+i|k) R u(k+i|k) \right] \tag{5.4}$$

$$+ x^T(k+N|k) \overline{Q} x(k+N|k), \tag{5.5}$$

where Q, R are positive definite weight matrices, and $\overline{Q}$ is the weight matrix for the terminal predicted state. Since $J(k)$ is a function of $\mathbf{u}(k)$ via the state equation (5.1), the optimal input sequence is given by

$$\mathbf{u}^*(k) = \arg\min_{\mathbf{u}} J(k). \tag{5.6}$$

5.2.3 Receding Horizon Implementation

Only the first element of the optimal predicted input sequence $\mathbf{u}^*(k)$ is passed to the plant, i.e.,

$$u(k) = u^*(k|k). \tag{5.7}$$

The process of computing $\mathbf{u}^*(k)$ by minimizing (5.5), and implementing the first element of $\mathbf{u}^*$, is then repeated at each sampling instant k. Therefore, unlike LQ control, the optimization defining $\mathbf{u}^*$ is indeed an **online** optimization. The prediction horizon remains the same length despite the repetition of the optimization at future time instants. Therefore, the approach is known as a **receding horizon** strategy.

MPC originated in the late seventies and has developed considerably over the last few years within both the research control community and industry [83]. The main advantage of MPC over PID and LQ-optimal control techniques is the explicit handling of actuator and state constraints [83]. MPC is proactive [84] as it recalculates the optimal input sequence online at each time step by considering both input and state constraints. Therefore, it eliminates the need for anti-windup augmentation and high level of skill and experience required for the tuning of the controllers [85].

5.3 MPC Implementation for the NSTX-U

5.3.1 MPC Formulation with Integral Action

Using the superscript tilde notation ($\tilde{}$) to represent the deviations from reference input and state trajectories, the discrete-time version of the LTI ι-profile evolution

model (4.93)-(4.94) takes the form

$$\tilde{\iota}(k+1) = \overline{A}_d\,\tilde{\iota}(k) + \overline{B}_d\,\tilde{u}(k), \tag{5.8}$$

$$y(k) = \overline{C}_d\,\tilde{\iota}(k), \tag{5.9}$$

where $\overline{A}_d$, $\overline{B}_d$, $\overline{C}_d$ are the discrete versions of $\overline{A}$, $\overline{B}$, and $\overline{C}$ in the continuous time model (4.93)-(4.94), $\tilde{u}(k) \in \mathbb{R}^{m\times 1}$ and $\tilde{\iota}(k) \in \mathbb{R}^{n\times 1}$ define the deviations from a reference input $u_r(k)$, and reference state trajectory, $\iota_r(k)$, respectively, i.e.,

$$\tilde{u}(k) = u(k) - u_r(k) \tag{5.10}$$

$$\tilde{\iota}(k) = \iota(k) - \iota_r(k). \tag{5.11}$$

Standard MPC algorithms do not achieve integral action [86]. However, an integral action is required in the controller to achieve offset-free tracking against modeling uncertainties and various external disturbances. A method for incorporating an integrator within the MPC framework is to modify the plant model so that the input is the control increment $\Delta\tilde{u}(k)$, rather than control $\tilde{u}(k)$ [85], [87], [88]. This is achieved by taking the difference of both sides of (5.8) to form

$$\Delta\tilde{\iota}(k+1) = \overline{A}_d\Delta\tilde{\iota}(k) + \overline{B}_d\Delta\tilde{u}(k), \tag{5.12}$$

where

$$\Delta\tilde{\iota}(k) = \tilde{\iota}(k) - \tilde{\iota}(k-1) \tag{5.13}$$

$$\Delta\tilde{u}(k) = \tilde{u}(k) - \tilde{u}(k-1) \tag{5.14}$$

Next, from the output equation (5.9) one can obtain the output increment as

$$\begin{aligned}\Delta y(k+1) &= y(k+1) - y(k) \\ &= \overline{C}_d \left(\tilde{\iota}(k+1) - \tilde{\iota}(k)\right) \\ &= \overline{C}_d \overline{A}_d \Delta\tilde{\iota}(k) + \overline{C}_d \overline{B}_d \Delta\tilde{u}(k) \end{aligned} \tag{5.15}$$

Finally, defining a new state vector as

$$x = \begin{bmatrix} \Delta\tilde{\iota}(k) \\ y(k) \end{bmatrix} \tag{5.16}$$

Equations (5.12) and (5.15) are combined to form the enlarged plant

$$x(k+1) = \widetilde{A}x(k) + \widetilde{B}\Delta\tilde{u}(k), \tag{5.17}$$

$$y(k) = \widetilde{C}x(k), \tag{5.18}$$

where

$$\widetilde{A} = \begin{bmatrix} \overline{A}_d & 0_{n\times m} \\ \overline{C}_d\overline{A}_d & I_{m\times m} \end{bmatrix},\ \widetilde{B} = \begin{bmatrix} \overline{B}_d \\ \overline{C}_d\overline{B}_d \end{bmatrix},\ \widetilde{C} = \begin{bmatrix} 0_{n\times m} \\ I_{m\times m} \end{bmatrix}^T \tag{5.19}$$

Note that the state-space equations (5.17)-(5.18) may be used to define a Prediction Model (PM) [86] of the form

$$y_{k+1|N} = O_N\widetilde{A}x(k) + F_N\Delta\tilde{u}_{k|N}\ , \tag{5.20}$$

where the extended vectors $y_{k+1|N}$, $\Delta\tilde{u}_{k|N}$ are

$$y_{k+1|N}=\begin{bmatrix} y(k+1) \\ y(k+2) \\ \vdots \\ y(k+N) \end{bmatrix}, \quad \Delta\tilde{u}_{k|N}=\begin{bmatrix} \Delta\tilde{u}(k) \\ \Delta\tilde{u}(k+1) \\ \vdots \\ \Delta\tilde{u}(k+N-1) \end{bmatrix} \tag{5.21}$$

and

$$O_N = \begin{bmatrix} \widetilde{C} & \widetilde{C}\widetilde{A} & \widetilde{C}\widetilde{A}^2 & \dots & \widetilde{C}\widetilde{A}^{N-1} \end{bmatrix}^T, \tag{5.22}$$

$$F_N=\begin{bmatrix} \widetilde{C}\widetilde{B} & 0 & 0 & 0 & \cdots & 0 \\ \widetilde{C}\widetilde{A}\widetilde{B} & \widetilde{C}\widetilde{B} & 0 & 0 & \cdots & 0 \\ \widetilde{C}\widetilde{A}^2\widetilde{B} & \widetilde{C}\widetilde{A}\widetilde{B} & \widetilde{C}\widetilde{B} & 0 & \cdots & 0 \\ \vdots & \vdots & \vdots & \ddots & & 0 \\ \vdots & \vdots & \vdots & & \ddots & 0 \\ \widetilde{C}\widetilde{A}^{N-1}\widetilde{B} & \widetilde{C}\widetilde{A}^{N-2}\widetilde{B} & \cdots & \cdots & \widetilde{C}\widetilde{A}\widetilde{B} & \widetilde{C}\widetilde{B} \end{bmatrix}. \tag{5.23}$$

Note that the control objective is to track the reference profile, $\iota_r(k)$ with minimum control effort. Therefore, the performance index of the MPC formulation needs to penalize both the predicted tracking error and the predicted changes to the control input [85], taking the form [84]

$$J(k) = \sum_{i=1}^{N} \Big[y(k+i)^T Q y(k+i) + \Delta\tilde{u}(k+i-1)^T R \Delta\tilde{u}(k+i-1) \Big], \tag{5.24}$$

where $y \in \mathbb{R}^{m\times 1}$ is the predicted output, $\Delta\tilde{u} \in \mathbb{R}^{m\times 1}$ is the future change in the feedback control input (i.e., future feedback control increment), and N is the length of the prediction horizon. Using the PM (5.20), the general quadratic cost (5.24) can

be rewritten compactly as

$$J(k) = \Delta\tilde{u}_{k|N}^T H \Delta\tilde{u}_{k|N} + 2x^T(k) f^T \Delta\tilde{u}_{k|N} + J_0, \tag{5.25}$$

where

$$H = F_N^T \widetilde{Q} F_N + \widetilde{R}, \tag{5.26}$$

$$f = F_N^T \widetilde{Q} O_N \widetilde{A}, \tag{5.27}$$

with enlarged cost weight matrices

$$\widetilde{Q} = \begin{bmatrix} Q & 0 & \cdots & 0 \\ 0 & \ddots & & \vdots \\ \vdots & & Q & 0 \\ 0 & \cdots & 0 & Q \end{bmatrix}, \; \widetilde{R} = \begin{bmatrix} R & 0 & \cdots & 0 \\ 0 & \ddots & & \vdots \\ \vdots & & R & 0 \\ 0 & \cdots & 0 & R \end{bmatrix}. \tag{5.28}$$

Note that the term J_0 on the RHS of (5.25) is a scalar depending on the initial condition, $y(k)$, not on the unknown $\Delta\tilde{u}_{k|N}$. Therefore, it is not a part of the optimization problem, and is omitted in this derivation.

5.3.2 Incorporating Constraints

Let $u_{\max} \in \mathbb{R}^{m\times 1}$ and $u_{\min} \in \mathbb{R}^{m\times 1}$ define the input limits for the actual (physical) actuators of NSTX-U. Hence, for the predicted input sequence, $u_{k|N}$, it is possible to write

$$u_{\min|N} \leq u_{k|N} \leq u_{\max|N}, \tag{5.29}$$

where

$$u_{\min|N} = [u_{\min} \;\; u_{\min} \;\; \dots \;\; u_{\min}]^T \in \mathbb{R}^{Nm\times 1} \tag{5.30}$$

$$u_{\max|N} = [u_{\max} \;\; u_{\max} \;\; \dots \;\; u_{\max}]^T \in \mathbb{R}^{Nm\times 1} \tag{5.31}$$

Note that $\tilde{u}_{k|N} = u_{k|N} - u_{r_{k|N}}$, where

$$u_{r_{k|N}} = [u_r(k) \;\; u_r(k+1) \;\; \dots \;\; u_r(k+N-1)]^T \tag{5.32}$$

is the reference input sequence corresponding to the future input sequence, $u_{k|N}$. Therefore, the upper and lower limits for the feedback control sequence, $\tilde{u}_{k|N}$, can be obtained by subtracting (5.32), from all terms of (5.29) as

$$\underbrace{u_{\min|N} - u_{r_{k|N}}}_{\tilde{u}_{\min_{k|N}}} \leq \tilde{u}_{k|N} \leq \underbrace{u_{\max|N} - u_{r_{k|N}}}_{\tilde{u}_{\max_{k|N}}} \tag{5.33}$$

Using the control increment (5.14) recursively, it is possible to obtain the following matrix equation

$$\tilde{u}_{k|N} = S\Delta\tilde{u}_{k|N} + c\tilde{u}(k-1) \tag{5.34}$$

where $S \in \mathbb{R}^{Nm\times Nm}$ and $c \in \mathbb{R}^{Nm\times m}$ are given by

$$S = \begin{bmatrix} I_m & 0_m & \dots & 0_m \\ I_m & I_m & \dots & 0_m \\ \vdots & \vdots & \ddots & \vdots \\ I_m & I_m & \dots & I_m \end{bmatrix}, \quad c = \begin{bmatrix} I_m \\ I_m \\ \vdots \\ I_m \end{bmatrix}, \tag{5.35}$$

where I_m is $m \times m$ identity matrix and 0_m is the $m \times m$ matrix of zeros. Substituting (5.34) into (5.33), the inequality for the future feedback control increment, $\Delta\tilde{u}_{k|N}$

becomes

$$\tilde{u}_{\min_{k|N}} - c\tilde{u}(k-1) \leq S\Delta\tilde{u}_{k|N} \leq \tilde{u}_{\max_{k|N}} - c\tilde{u}(k-1) \tag{5.36}$$

The constraints (5.36) are equivalent to

$$S\Delta\tilde{u}_{k|N} \leq \tilde{u}_{\max_{k|N}} - c\tilde{u}(k-1) \tag{5.37}$$

$$-S\Delta\tilde{u}_{k|N} \leq -\tilde{u}_{\min_{k|N}} + c\tilde{u}(k-1) \tag{5.38}$$

Finally, it is convenient to rewrite the constraints (5.37)-(5.38) compactly in the following linear matrix inequality

$$\mathcal{A}\Delta\tilde{u}_{k|N} \leq b_k, \tag{5.39}$$

where

$$\mathcal{A} = \begin{bmatrix} S \\ -S \end{bmatrix}, \quad b_k = \begin{bmatrix} \tilde{u}_{\max_{k|N}} - c\tilde{u}(k-1) \\ -\tilde{u}_{\min_{k|N}} + c\tilde{u}(k-1) \end{bmatrix}. \tag{5.40}$$

5.3.3 Quadratic Programming

To solve the integral MPC formulation, the performance index (5.25) with the plant model (5.8)-(5.9) should be minimized with respect to the unknown future feedback control increments, while satisfying the input constraints given by the inequality (5.39), i.e.,

$$\Delta\tilde{u}^*_{k|N} = \arg\min_{\Delta\tilde{u}_{k|N}} \left\{\Delta\tilde{u}^T_{k|N} H \Delta\tilde{u}_{k|N} + 2x^T(k) f^T \Delta\tilde{u}_{k|N}\right\} \tag{5.41}$$

$$\text{subject to } \mathcal{A}\Delta\tilde{u}_{k|N} \leq b_k \tag{5.42}$$

This defines a standard Quadratic Programming (QP) problem in terms of the unknown future feedback control increments, $\Delta\tilde{u}_{k|N}$. A receding horizon strategy is used and only the first control increment $\Delta\tilde{u}^*(k)$ in the calculated $\Delta\tilde{u}^*_{k|N}$ is used for control. The optimal feedback control action to the plant (5.8)-(5.9) then becomes

$$\tilde{u}(k) = \Delta\tilde{u}^*(k) + \tilde{u}(k-1). \tag{5.43}$$

5.4 Performance Assessment of the Integral MPC Design via Closed-Loop Simulations

Both for modeling and control design, a reference state trajectory $\iota_r(\hat{\rho}, t)$ is generated through the open-loop TRANSP run 142301W12, which is based on NSTX-U shape and actuators, and for which the actuator requests are set to the following arbitrary constants

$$\begin{aligned} u_r(k) = u_r &= [u_n \quad P_1 \quad P_2 \quad P_3 \quad P_4 \quad P_5 \quad P_6 \quad I_p]^T \\ &= [1.0 \;\; 0.2 \;\; 0.4 \;\; 0.6 \;\; 0.8 \;\; 1.0 \;\; 1.2 \;\; 0.7]^T \end{aligned} \tag{5.44}$$

Both for control design and closed-loop simulation, the non-dimensional spatial domain ($\hat{\rho} \in [0\ 1]$) is equally divided into $l = 21$ radial nodes, hence, the radial grid size is $\Delta\hat{\rho} = 0.05$. Control simulations are then carried out for $t \in [t_0\ t_f] = [1.0\ 4.0]$ s. The control sampling time is set to $T_s = 0.01$ s. Note that MPC may not guarantee closed-loop stability for arbitrary values of the prediction horizon, N. In general, the chance of getting closed-loop instability decreases with an increasing N, at the expense of an increase in computational time since the length of the unknown vector $\Delta\tilde{u}_{k|N}$ in (5.41)-(5.42) also increases with an increasing N [84]. In this case, some

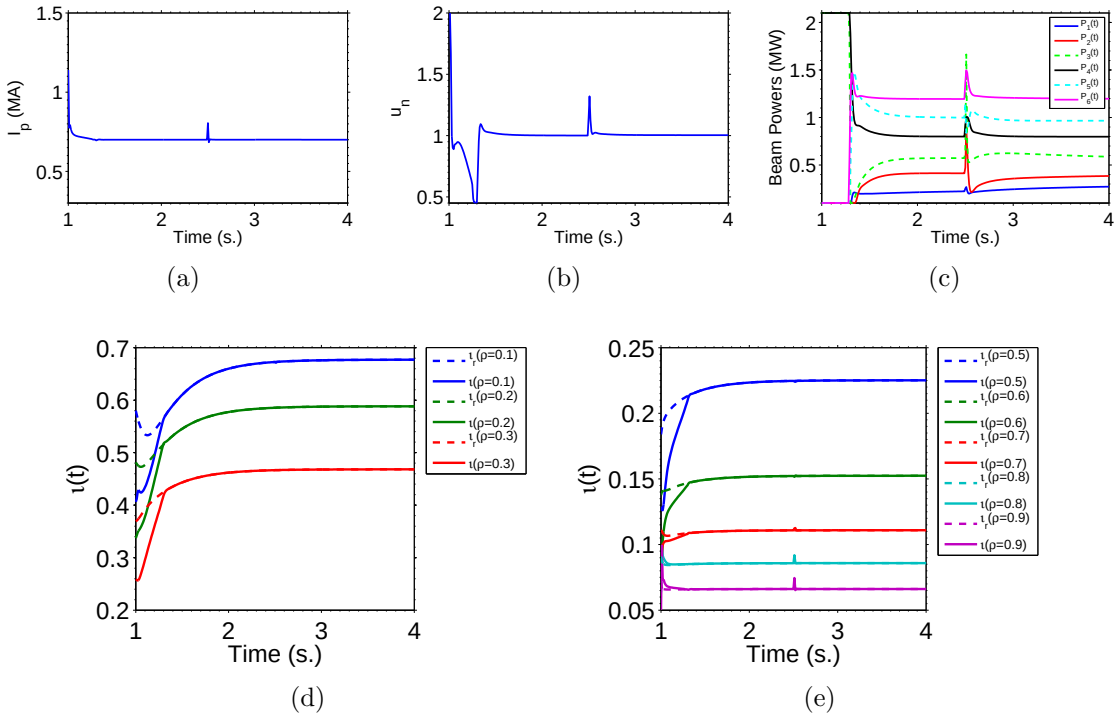

Figure 5.1: Tracking simulation results: (a)-(c) Time evolution of the optimal plasma current, electron density regulation and neutral beam injection powers; (d)-(e) Time evolution of the actual outputs (solid) with their respective targets (dashed).

of the closed-loop poles of the unconstrained MPC (i.e., the eigenvalues of $\widetilde{A} + \widetilde{B}K$, where $K = -H^{-1}f$) start to cross the unit circle for $N \leq 4$. Therefore, $N = 5$ is picked to guarantee closed-loop stability without increasing the computational effort considerably.

In this closed-loop control simulation study, the initial condition perturbation rejection capability is tested during the first 1.5 seconds of the discharge by setting $\iota(t_0) = \iota_r(t_0) + 0.3\iota_r(t_0)$. In addition to an initial condition perturbation, step disturbances are also added in each input channel starting at $t = 2.5$ s., i.e.,

$$\tilde{u}(k) = \begin{cases} \Delta\tilde{u}^*(k) + \tilde{u}(k-1), & t < 2.5\,\text{s}. \\ \Delta\tilde{u}^*(k) + \tilde{u}(k-1) + u_d, & t \geq 2.5\,\text{s}. \end{cases} \tag{5.45}$$

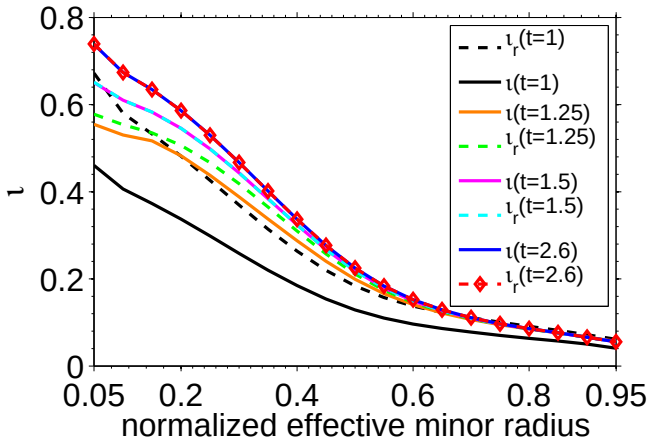

Figure 5.2: Time evolution of the rotational transform (ι-profile).

where $u_d = 0.15u_r$. To seek a faster response, the cost weight matrices are set to $Q = 1000\, I_{8\times 8}$ and $R = \text{diag}(0.01, 0.005, 0.001, 0.0001, 0.01, 0.001, 0.01, 0.01)$.

At the beginning of each simulation step, k, the QP problem (5.41)-(5.42) is solved in MATLAB to obtain the future feedback control increment, $\Delta\tilde{u}_{k|N}$. Receding control strategy is used to update the feedback control according to (5.43). The nonlinear MDE (2.5)-(2.6) is then simulated in MATLAB with the updated control input, and the prediction horizon is shifted for the next time step.

The results of the closed-loop control simulation is provided in Fig. 5.1. The time evolution of the optimal physical inputs are illustrated in Figs. 5.1(a)-(c). The corresponding time evolution of the optimal outputs are depicted in Figs. 5.1(d)-(e) along with their respective targets. Note from Figs. 5.1(d)-(e) that in the absence of the input disturbances, the outputs are regulated around their desired values within the first 0.5 s. of the simulation. This is also reflected in Fig. 5.2, through the comparison of the ι-profile achieved at $t = 1.5$ s. with the desired target profile, $\iota_r(t = 1.5)$, along with the unperturbed initial profile, $\iota_r(t = 1)$, and the perturbed initial profile, $\iota(t = 1)$. Note from Fig. 5.1(e) that the outer states jump again at $t = 2.5$ s., which is the effect of the step disturbance inputs added at that instant.

The integral MPC strategy instantly cancels the effect of these input disturbances, providing almost excellent profile matching at $t = 2.6$ s. in Fig. 5.2. Based on this simulation analysis, the proposed controller is shown to be effective in regulating the ι-profile around a target profile in NSTX-U.

5.5 Conclusion

In this chapter, a constrained MPC algorithm has been formulated for tracking a desired rotational transform profile, and hence a desired current density profile, in NSTX-U. The neutral beam powers, electron density, and total plasma current are used as actuators. An integrator is added to the standard MPC formulation to achieve offset-free tracking against various modeling uncertainties and external disturbances. The effectiveness of the proposed MPC control scheme is demonstrated via closed-loop numerical simulations based on the control-oriented MDE solver.

Chapter 6

Conclusion and Future Work

In this dissertation, first-principles-driven model-based feedforward and feedback control algorithms have been developed for the geometry and the actuators of NSTX-U. In this final chapter, contributions of this research work are summarized and directions for possible future research work are provided.

6.1 Contributions of this Dissertation

The contributions of this dissertation can be summarized as follows.

1. Following the general first-principles-driven (FPD) modeling approach developed by the Lehigh University Plasma Control Group, a control-oriented model for the current density profile evolution has been developed for the first time for NSTX-U. The model has been tailored to the geometry and actuators of NSTX-U by using predictions provided by the physics-oriented transport code TRANSP. This control-oriented model predicts the spatial-temporal evolution of the current density profile by combining the nonlinear Magnetic Diffusion Equation (MDE) with physics-based correlations obtained from NSTX-U for the electron density, electron temperature, and non-inductive current drives (neu-

tral beams). The modeling approach has been extended in this work through the use of time-varying geometric factors. However, simulations results show that the accuracy improvement is marginal for the analyzed scenarios.

2. Using the control-oriented model tailored to NSTX-U, a model-based optimal feedforward control algorithm has been designed for the first time for NSTX-U. Given a desired operating state, the optimizer produces actuator trajectories that can steer the plasma to such state. Nonlinear numerical optimization techniques developed by the Lehigh University Plasma Control Group [1] have been extended in this work to NSTX-U. The effectiveness of the nonlinear actuator trajectory optimizer is shown through nonlinear simulations based on the developed control-oriented MDE solver. The optimal feedforward control algorithm provides a systematic approach for advanced scenario planning in NSTX-U.

3. Using once again the control-oriented model tailored to NSTX-U, a model-based optimal feedback control algorithm has been designed for the first time for NSTX-U. The feedback control algorithm complements the feedforward control solution by improving tracking while adding robustness against model uncertainties and external disturbances to the overall current profile control scheme. The control-oriented plasma response model (an infinite dimensional PDE) is reduced through spatial discretization and then linearized around the target state and input trajectories to provide a linear time variant (LTV) model. A linear quadratic integral (LQI) optimal feedback controller is designed based on the resulting LTV model to regulate the poloidal flux gradient profile, and hence the current density profile, around a desired target profile. The effectiveness of the proposed optimal feedback controller is tested in numerical simulations based on the developed control-oriented MDE solver.

4. The proposed LQI optimal current-profile controller has been tested in numerical simulations based on the physics-oriented transport code TRANSP by utilizing the Expert routine [2]. In this way, a current density profile controller has been implemented in TRANSP for the first time for NSTX-U. The line-averaged electron density, the neutral-beam powers, and the total plasma current are used as actuators in the TRANSP simulations. Current and density rate limits are introduced into the standard Expert routine. Robustness against varying confinement conditions is also tested in TRANSP for the first time using the proposed LQI controller. The promising closed-loop TRANSP simulation results motivate the implementation of the proposed optimal control algorithm in NSTX-U once critical diagnostics (MSE) are commissioned and relevant plasma scenarios are achieved.

5. A feedback controller based on a model predictive control (MPC) strategy is designed for the first time to regulate the rotational transform profile around a desired target profile in NSTX-U. The neutral beam powers, the electron density, and the total plasma current are used as actuators. An integrator is embedded into the standard MPC formulation to account for various modeling uncertainties and external disturbances. The proposed MPC strategy incorporates various state and actuator constraints directly into the control design process by solving a constrained optimization problem in real-time to determine the optimal actuator requests. Therefore, it eliminates the need for a separate anti-windup controller design and the manual tuning of the controller's gains. The effectiveness of the proposed MPC strategy in regulating the current density profile in NSTX-U is demonstrated in closed-loop simulations based on the developed control-oriented MDE solver.

6.2 Future Work

The biggest challenge associated with this dissertation work has been the lack of experimental data from NSTX-U since the upgrade did not start operations until the second half of 2015. Moreover, plasma scenarios relevant to this dissertation work have not been achieved yet. Therefore, all modeling and control design work has been done by using TRANSP predictions for NSTX-U's shape and actuator configuration based on scaled profiles obtained from NSTX experiments. As a consequence, experimental testing of the combined feedforward and feedback controllers are not included in this dissertation. However, this dissertation work already sets the foundation that is necessary to make active current profile control in NSTX-U a reality in the near future. Once the motional Stark effect (MSE) magnetic-field-pitch-angle diagnostics start operating, and relevant plasma scenarios are achieved, the developed feedforward+feedback controllers can be tested in the actual NSTX-U device after some model refinement and control re-design work is carried out as detailed below.

- Refinement of the FPD control-oriented model using actual experimental data once NSTX-U achieves relevant plasma scenarios. Use of NSTX-U's experimental data to augment the developed MDE-based control-oriented model with either a one-dimensional model for electron temperature prediction or a zero-dimensional model for plasma stored energy prediction.

- Redesign of optimal feedforward actuator trajectories based on refined FPD control-oriented model. Alternatively, design of optimal feedforward actuator trajectories based on TRANSP by wrapping the transport code by the developed numerical optimizer. Experimental testing of proposed optimal feedforward control algorithms.

- Redesign of LQI-based optimal feedback control algorithm based on refined FPD control-oriented model. Numerical testing in both control-oriented and TRANSP closed-loop simulations. Experimental testing.

- Redesign of MPC-based optimal feedback control algorithm based on refined FPD control-oriented model. Implementation of MPC algorithm in TRANSP's Expert routine. Numerical testing in both control-oriented and TRANSP closed-loop simulations. Experimental testing.

Bibliography

[1] J. Barton, M. Boyer, W. Shi, W. Wehner, E. Schuster *et al.*, "Physics-model-based nonlinear actuator trajectory optimization and safety factor profile feedback control for advanced scenario development in DIII-D," *Nuclear Fusion*, vol. 55, no. 9, p. 093005, 2015.

[2] M. D. Boyer, R. Andre, D. A. Gates, S. Gerhardt, I. R. Goumiri, and J. Menard, "Central safety factor and β_N control on NSTX-U via beam power and plasma boundary shape modification, using TRANSP for closed loop simulations," *Nuclear Fusion*, vol. 55, no. 5, p. 053033, 2015.

[3] PPPL. (2016) NSTX Upgrade five year plan. [Online]. Available: http://nstx.pppl.gov

[4] U.S. Energy Information Administration. (2016) International energy outlook 2016. [Online]. Available: http://www.eia.gov

[5] Energy without Carbon. (2016) Nuclear fusion. [Online]. Available: http://www.energy-without-carbon.org

[6] ITER and Fusion Energy. (2016) Magnetic confinement fusion. [Online]. Available: http://iter.rma.ac.be

[7] EUROfusion. (2016) Tokamak principle. [Online]. Available: http://www.euro-fusion.org

[8] A. Pironti and M. Walker, "Fusion, Tokamaks, and Plasma Control," *IEEE Control Systems Magazine*, vol. 25, no. 5, pp. 30–43, 2005.

[9] B. L. Tan and G. L. Huang, "Neoclassical bootstrap current in solar plasma loops," *Astronomy and Astrophysics*, vol. 453, no. 1, pp. 321–327, 2006.

[10] J. Friedberg, *Ideal Magnetohydrodynamics*. Plenum Press, New York, 1987.

[11] M. Ariola and A. Pironti, *Magnetic Control of Tokamak Plasmas*. Springer, 2008.

[12] A. Pironti and M. Walker, "Control of Tokamak Plasmas," *IEEE Control Systems Magazine*, vol. 25, no. 5, pp. 24–29, 2005.

[13] EUROfusion. (2016) Research for tomorrow's energy supply. [Online]. Available: http://www.euro-fusion.org

[14] Visions 2200 - A Perspective on the Future. (2016) Cheap energy? [Online]. Available: http://www.visions2200.com

[15] J. Sheffield, "The physics of magnetic fusion reactors," *Reviews of Modern Physics*, vol. 66, pp. 1015–1103, 1994.

[16] J. Wesson, *Tokamaks*. Clarendon Press, Oxford, UK, 1984.

[17] S. P. Gerhardt, R. Andre, and J. E. Menard, "Exploration of the equilibrium operating space for NSTX-Upgrade," *Nuclear Fusion*, vol. 52, no. 8, p. 083020, 2012.

[18] EUROfusion. (2016) The plasma edge. [Online]. Available: http://www.eurofusion.org

[19] G. Hammett. (2009) Heat transport in tokamaks (I): The bad-curvature ITG instability. [Online]. Available: http://w3.pppl.gov/∼hammett/refs/2009/ITG-Lecture09.pdf

[20] A. Heller. (2016) Experiment mimics nature's way with plasmas. [Online]. Available: http://str.llnl.gov/str/Hill.html

[21] PPPL. (2015) Construction completed, PPPL is set to resume world-class fusion research. [Online]. Available: http://www.pppl.gov/news

[22] M. Ono, J. Chrzanowski *et al.*, "Progress toward commissioning and plasma operation in NSTX-U," *Nuclear Fusion*, vol. 55, no. 7, p. 073007, 2015.

[23] ITER. (2016) What is ITER? [Online]. Available: http://www.iter.org

[24] Fusion For Energy. (2016) Demonstrating power plants (DEMO). [Online]. Available: http://fusionforenergy.europa.eu

[25] T. Suzuki *et al.*, "Recent RF Experiments and Application of RF Waves to Real-Time Control of Safety Factor Profile in JT-60U," in *AIP Conference Proceedings (Park City, UT, USA)*, 2005, pp. 279–286.

[26] T. Suzuki, S. Ide, T. Oikawa, T. Fujita, M. Ishikawa, M. Seki *et al.*, "Off-axis Current Drive and Real-time Control of Current Profile in JT-60U," *Nuclear Fusion*, vol. 48, no. 4, p. 045002, 2008.

[27] JT-60SA. (2016) What is JT-60SA? [Online]. Available: http://www.jt60sa.org

[28] T. Wijnands *et al.*, "Feedback Control of the Current Profile on Tore Supra," *Nuclear Fusion*, vol. 37, no. 6, pp. 777–791, 1997.

[29] O. Barana *et al.*, "Feedback Control of the Lower Hybrid Power Deposition Profile on Tore Supra," *Plasma Physics and Controlled Fusion*, vol. 49, no. 7, pp. 947–967, 2007.

[30] EURATOM-CEA. (2006) Tore Supra. [Online]. Available: http://www-fusion-magnetique.cea.fr/gb/accueil/index.htm

[31] L. Laborde *et al.*, "A Model-based Technique for Integrated Real-time Profile Control in the JET Tokamak," *Plasma Physics and Controlled Fusion*, vol. 47, no. 1, pp. 155–183, 2005.

[32] D. Moreau, F. Crisanti, X. Litaudon, D. Mazon, P. D. Vries, R. Felton, E. Joffrin, L. Laborde, M. Lennholm, A. Murari, V. Pericoli-Ridolfini, M. Riva, T. Tala, G. Tresset, L. Zabeo, K. Zastrow, and contributors to the EFDA-JET Workprogramme, "Real-time control of the q -profile in JET for steady state advanced tokamak operation," *Nuclear Fusion*, vol. 43, no. 9, p. 870, 2003.

[33] D. Moreau, D. Mazon, M. Ariola, G. D. Tommasi, L. Laborde, F. Piccolo, F. Sartori, T. Tala, L. Zabeo, A. Boboc, E. Bouvier, M. Brix, J. Brzozowski, C. Challis, V. Cocilovo, V. Cordoliani, F. Crisanti, E. D. L. Luna, R. Felton, N. Hawkes, R. King, X. Litaudon, T. Loarer, J. Mailloux, M. Mayoral, I. Nunes, E. Surrey, O. Zimmerman, and J. E. Contributors, "A two-time-scale dynamic-model approach for magnetic and kinetic profile control in advanced tokamak scenarios on JET," *Nuclear Fusion*, vol. 48, no. 10, p. 106001, 2008.

[34] EUROfusion. (2016) JET. [Online]. Available: http://www.euro-fusion.org/jet

[35] J. Ferron, P. Gohil, C. Greenfield, J. Lohr, T. Luce, M. Makowski, D. Mazon, M. Murakami, C. Petty, P. Politzer, and M. Wade, "Feedback control of the safety factor profile evolution during formation of an advanced tokamak discharge," *Nuclear Fusion*, vol. 46, no. 10, p. L13, 2006.

[36] D. Moreau, D. Mazon, M. Walker, J. Ferron, K. Burrell, S. Flanagan, P. Gohil, R. Groebner, A. Hyatt, R. L. Haye, J. Lohr, F. Turco, E. Schuster, Y. Ou, C. Xu, Y. Takase, Y. Sakamoto, S. Ide, T. Suzuki, I.-I. group members, and experts, "Plasma models for real-time control of advanced tokamak scenarios," *Nuclear Fusion*, vol. 51, no. 6, p. 063009, 2011.

[37] J. Barton, Y. Ou, C. Xu, E. Schuster, and M. Walker, "Simserver simulation of a model-based current profile controller in the DIII-D Plasma Control System," *Fusion Engineering and Design*, vol. 86, no. 6-8, pp. 1116–1119, 2011.

[38] J. E. Barton, M. D. Boyer, W. Shi, E. Schuster, T. C. Luce, J. R. Ferron, M. L. Walker, D. A. Humphreys, B. G. Penaflor, and R. D. Johnson, "Toroidal current profile control during low confinement mode plasma discharges in DIII-D via first-principles-driven model-based robust control synthesis," *Nuclear Fusion*, vol. 52, no. 12, p. 123018, 2012.

[39] W. Shi, W. Wehner, J. Barton, M. D. Boyer, E. Schuster *et al.*, "Multivariable Robust Control of the Plasma Rotational Transform Profile for Advanced Tokamak Scenarios in DIII-D," in *2012 American Control Conference (Montreal, QC, Canada)*, 2012, pp. 5037–5042.

[40] W. Wehner, W. Shi, E. Schuster *et al.*, "Optimal Feedback Control of the Poloidal Magnetic Flux Profile in the DIII-D Tokamak Based on Identified Plasma Re-

sponse Models," in *2012 American Control Conference (Montreal, QC, Canada)*, 2012, pp. 5049–5054.

[41] M. D. Boyer, J. Barton, E. Schuster, T. C. Luce, J. R. Ferron, M. L. Walker, D. A. Humphreys, B. G. Penaflor, and R. D. Johnson, "First-principles-driven model-based current profile control for the DIII-D tokamak via LQI optimal control," *Plasma Physics and Controlled Fusion*, vol. 55, no. 10, p. 105007, 2013.

[42] M. D. Boyer, J. Barton, E. Schuster, M. L. Walker, T. C. Luce, J. R. Ferron, B. G. Penaflor, R. D. Johnson, and D. A. Humphreys, "Backstepping Control of the Toroidal Plasma Current Profile in the DIII-D Tokamak," *IEEE Transactions on Control Systems Technology*, vol. 22, no. 5, pp. 1725–1739, 2014.

[43] J. Barton, M. Boyer, W. Shi, W. Wehner, E. Schuster, J. Ferron, M. Walker, D. Humphreys, T. Luce, F. Turco, B. Penaflor, and R. Johnson, "Physics-model-based nonlinear actuator trajectory optimization and safety factor profile feedback control for advanced scenario development in DIII-D," *Nuclear Fusion*, vol. 55, no. 9, p. 093005, 2015.

[44] General Atomics. (2016) DIII-D. [Online]. Available: http://fusion.gat.com

[45] I. Goumiri, C. Rowley, S. Sabbagh *et al.*, "Modeling and control of plasma rotation for NSTX using neoclassical toroidal viscosity and neutral beam injection," *Nuclear Fusion*, vol. 56, no. 3, p. 036023, 2016.

[46] TRANSP Homepage. (2016). [Online]. Available: http://w3.pppl.gov/transp

[47] F. M. Levinton and H. Yuh, "The motional Stark effect diagnostic on NSTX," *Review of Scientific Instruments*, vol. 79, no. 10, p. 10F522, 2008.

[48] F. Hinton and R. Hazeltine, "Theory of Plasma Transport in Toroidal Confinement Systems," *Rev. Mod. Phys.*, vol. 48, pp. 239–308, 1976.

[49] Y. Ou *et al.*, "Towards model-based current profile control at DIII-D," *Fusion Engineering and Design*, vol. 82, pp. 1153–1160, 2007.

[50] E. Witrant *et al.*, "A control-oriented model of the current profile in tokamak plasma," *Plasma Physics and Controlled Fusion*, vol. 49, no. 7, pp. 1075–1105, 2007.

[51] Y. Ou and E. Schuster, "On Stability of Receding Horizon Control of Bilinear Parabolic PDE Systems," in *49th IEEE Conference on Decision and Control (Atlanta, GA, USA)*, 2010.

[52] Y. Ou, C. Xu, and E. Schuster, "Robust Control Design for the Poloidal Magnetic Flux Profile Evolution in the Presence of Model Uncertainties," *IEEE Transactions on Plasma Science*, vol. 38, no. 3, pp. 375–382, 2010.

[53] F. Felici *et al.*, "Real-time physics-model-based simulation of the current density profile in tokamak plasmas," *Nuclear Fusion*, vol. 51, no. 8, p. 083052, 2011.

[54] Y. Ou, C. Xu, E. Schuster, T. C. Luce, J. R. Ferron, M. L. Walker, and D. A. Humphreys, "Receding-Horizon Optimal Control of the Current Profile Evolution During the Ramp-Up Phase of a Tokamak Discharge," *Control Engineering Practice*, vol. 19, no. 1, pp. 22–31, 2011.

[55] ——, "Optimal Tracking Control of Current Profile in Tokamaks," *IEEE Transactions on Control Systems Technology*, vol. 19, no. 2, pp. 432–441, 2011.

[56] C. Xu, Y. Ou, and E. Schuster, "Receding Horizon Control of the Magnetic Flux Bilinear PDE based on Sequential Linear Quadratic Control," in *7th Interna-*

tional Congress on Industrial and Applied Mathematics (Vancouver, Canada), 2011.

[57] ——, "Sequential Linear Quadratic Control of Bilinear Parabolic PDEs based on POD Model Reduction," *IEEE Transactions on Control Systems Technology*, vol. 47, no. 2, pp. 418–426, 2011.

[58] O. Gaye, E. Moulay, S. Bremond, L. Autrique, R. Nouailletas, and Y. Orlov, "Sliding Mode Stabilization of the Current Profile in Tokamak Plasmas," in *50th IEEE Conference on Decision and Control (Orlando, FL, USA)*, 2011, pp. 2638–2643.

[59] A. Gahlawat, E. Witrant, M. M. Peet, and M. Alamir, "Bootstrap Current Optimization in Tokamaks using Sum-of-Squares Polynomials," in *51st IEEE Conference on Decision and Control (Maui, HI, USA)*, 2012, pp. 4359–4365.

[60] N. M. T. Vu, R. Nouailletas, L. Lefevre, and S. Bremond, "An IDA-PBC Approach for the Control of 1D Plasma Profile in Tokamaks," in *52nd IEEE Conference on Decision and Control (Florence, Italy)*, 2013, pp. 4176–4181.

[61] F. B. Argomedo, E. Witrant, C. Prieur, S. Brmond, R. Nouailletas, and J.-F. Artaud, "Lyapunov-based distributed control of the safety-factor profile in a tokamak plasma," *Nuclear Fusion*, vol. 53, no. 3, p. 033005, 2013.

[62] J. E. Barton *et al.*, "Physics-based control-oriented modeling of the safety factor profile dynamics in high performance tokamak plasmas," in *52nd IEEE Conference on Decision and Control*, 2013, pp. 4182–4187.

[63] S. H. Kim *et al.*, "Full tokamak discharge simulation of ITER by combining DINA-CH and CRONOS," *Plasma Physics and Controlled Fusion*, vol. 51, no. 10, p. 105007, 2009.

[64] ITER Physics Basis, "Chapter1: Overview and summary," *Nuclear Fusion*, vol. 39, no. 12, p. 2137, 1999.

[65] A. G. Peeters, "The Bootstrap Current and Its Consequences," *Plasma Phys. and Control. Fusion*, vol. 42, pp. B231–B242, 2000.

[66] P. A. Politzer and G. D. Porter, "Power Threshold for Neutral Beam Current Drive," *Nucl. Fusion*, vol. 30, no. 8, p. 1605, 1990.

[67] M. L. Walker *et al.*, "Emerging Applications in Tokamak Plasma Control," *IEEE Control Systems Magazine*, vol. 26, no. 2, p. 35, 2006.

[68] O. Sauter *et al.*, "Neoclassical Conductivity and Bootstrap Current Formulas for General Axisymmetric Equilibria and Arbitrary Collisionality Regime," *Physics of Plasmas*, vol. 6, no. 7, p. 2834, 1999.

[69] Nova Photonics. (2012) The Motional Stark Effect (MSE) Diagnostic. [Online]. Available: http://www.novaphotonics.com/

[70] Y. Ou, C. Xu, E. Schuster *et al.*, "Design and simulation of extremum-seeking open-loop optimal control of current profile in the DIII-D tokamak," *Plasma Physics and Controlled Fusion*, vol. 50, no. 11, p. 115001, 2008.

[71] C. Xu, Y. Ou, J. Dalessio, E. Schuster *et al.*, "Ramp-up phase current profile control of tokamak plasmas via nonlinear programming," *IEEE Transactions on Plasma Science*, vol. 38, no. 2, pp. 163–173, 2010.

[72] F. Felici *et al.*, "Non-linear model-based optimization of actuator trajectories for tokamak plasma profile control," *Plasma Physics and Controlled Fusion*, vol. 54, no. 2, p. 025002, 2012.

[73] Swiss Plasma Center SPC. (2016) TCV Tokamak. [Online]. Available: http://spc.epfl.ch/research_TCV_Tokamak

[74] J. Nocedal and S. J. Wright, *Numerical optimization*. Springer, New York, 2006.

[75] D. S. Naidu, *Optimal Control Systems*. CRC Press, 2002.

[76] J. Huang and J. Menard, "Development of an auto-convergent free-boundary axisymmetric equilibrium solver," 47th Annual DPP Meeting (Denver, CO, 2005). [Online]. Available: http://www.osti.gov/scitech/biblio/1051805

[77] R. Andre, "TRANSP/PTRANSP isolver free boundary equilibrium solver," 54th Annual DPP Meeting (Providence, RI, 2012). [Online]. Available: http://meetings.aps.org/Meeting/DPP12/Session/JP8.123

[78] M. Greenwald, J. Terry, S. Wolfe, S. Ejima, M. Bell, S. Kaye, and G. Neilson, "A new look at density limits in tokamaks," *Nuclear Fusion*, vol. 28, no. 12, p. 2199, 1988.

[79] M. Greenwald, "Density limits in toroidal plasmas," *Plasma Physics and Controlled Fusion*, vol. 44, no. 8, p. R27, 2002.

[80] A. Pankin, D. McCune, R. Andre, G. Bateman, and A. Kritz, "The tokamak monte carlo fast ion module NUBEAM in the national transport code collaboration library," *Computer Physics Communications*, vol. 159, no. 3, pp. 157–184, 2004.

[81] ITER Physics Expert Group on Confinement and Transport and ITER Physics Expert Group on Confinement Modelling and Database and ITER Physics Basis Editors, "Chapter2: Plasma confinement and transport," *Nuclear Fusion*, vol. 39, no. 12, p. 2175, 1999.

[82] S. Kaye, M. Bell, R. Bell, E. Fredrickson, B. LeBlanc, K. Lee, S. Lynch, and S. Sabbagh, "Energy confinement scaling in the low aspect ratio national spherical torus experiment (NSTX)," *Nuclear Fusion*, vol. 46, no. 10, p. 848, 2006.

[83] E. F. Camacho and C. Bordons, *Model Predictive Control*. Springer-Verlag, London, UK, 1999.

[84] J. M. Maciejowski, *Predictive Control With Constraints*. Prentice-Hall, Harlow, UK, 2002.

[85] M. A. Stephens, C. Manzie, and M. C. Good, "Model predictive control for reference tracking on an industrial machine tool servo drive," *IEEE Transactions on Industrial Informatics*, vol. 9, no. 2, pp. 808–816, 2013.

[86] D. D. Ruscio, "Model predictive control with integral action: a simple MPC algorithm," *Modeling, Identification and Control*, vol. 34, no. 3, pp. 119–129, 2013.

[87] D. M. Prett and C. E. Garcia, *Fundamental Process Control*. H. Brenner Ed. Butterworth, Stoneham, MA, 1988.

[88] L. Wang, *Model Predictive Control System Design and Implementation Using MATLAB*. Springer-Verlog, London, UK, 2009.

Vita

The author was born in Ankara, Turkey on October 19, 1987, to Filiz and Cengiz Ilhan. He obtained the Bachelor of Science Degree in Mechanical Engineering from Middle East Technical University, Ankara, Turkey, in 2010. He began his Ph.D. program in May 2011, working with Prof. Eugenio Schuster in the Laboratory for Control of Complex Physical Systems in Lehigh University, Bethlehem, PA, USA. He has hold the positions of Teaching and Research Assistant, and he is a P.C. Rossin Doctoral Fellow in Mechanical Engineering at Lehigh University.

Journal Publications

1. **Zeki Okan Ilhan**, Qiaoqiao Wang, Jason Barry, David Huxley-Cohen, Hexiang Wang, Eugenio Schuster, Shuangwei Xie, Mark Gilmore and Andrew Ware, "Extremum-seeking-based fluctuation mitigation and azimuthal velocity profile regulation by E×B actuation in HELCAT", *IEEE Transactions on Plasma Science*, vol. 42, no. 3, pp. 458-468, 2014.

2. **Zeki Okan Ilhan**, David Huxley-Cohen, Hexiang Wang, Eugenio Schuster, Mark Gilmore and Andrew Ware, "Optimal control of the plasma azimuthal velocity profile by feedback E×B actuation in HELCAT", *IEEE Transactions on Plasma Science*, vol. 42, no. 3, pp. 469-476, 2014.

Refereed Conference Proceedings

1. **Zeki O. Ilhan**, William P. Wehner and Eugenio Schuster, "Model Predictive Control with Integral Action for the Rotational Transform Profile Tracking in NSTX-U", *IEEE Multi-Conference on Systems and Control (Buenos Aires, Argentina)*, September 19-22, 2016.

2. **Zeki Okan Ilhan**, William Wehner, Justin Barton, Eugenio Schuster, David Gates, Stefan Gerhardt and Jonathan Menard, "First-Principles-Driven Model-Based Optimal Control of the Current Profile in NSTX-U", *IEEE Multi-Conference on Systems and Control (Sydney, Australia)*, 2015, pp. 1303-1308.

Conference Proceedings

1. **Zeki Okan Ilhan**, Hexiang Wang, David Huxley-Cohen, Eugenio Schuster, Mark Gilmore and Andrew Ware, "Optimal Closed-Loop Control of the Azimuthal Velocity Profile by ExB Actuation in HELCAT", *25th Symposium on Fusion Engineering (San Francisco, CA, USA)*, June 10-14, 2013.

2. **Zeki Okan Ilhan**, Jason Barry, Hexiang Wang, Eugenio Schuster, Mark Gilmore and Andrew Ware, "Fluctuation Mitigation and Azimuthal Velocity Profile Regulation by Extremum Seeking in HELCAT", *25th Symposium on Fusion Engineering (San Francisco, CA, USA)*, June 10-14, 2013.

Conference Abstracts

1. **Zeki Ilhan**, W.P. Wehner, E. Schuster and M.D. Boyer, "Model Predictive Control with Integral Action for Current Density Profile Tracking in NSTX-U", *58th Division of Plasma Physics (DPP) Annual Meeting of the American*

Physical Society (APS), San Jose, California, USA, October 31-November 4, 2016.

2. **Zeki Ilhan**, J.E. Barton, E. Schuster, D.A. Gates, S.P. Gerhardt and J.E. Menard, "Physics-based control-oriented modeling of the current density profile evolution in NSTX-Upgrade", *29th Symposium on Fusion Technology (SOFT)*, Prague, Czech Republic, September 5-9, 2016.

3. **Zeki Ilhan**, William P. Wehner, Eugenio Schuster, Mark D. Boyer, David A. Gates, Stefan Gerhardt and Jonathan Menard "Performance Assessment of Model-Based Optimal Feedforward and Feedback Current Profile Control in NSTX-U using the TRANSP Code", *57th Division of Plasma Physics (DPP) Annual Meeting of the American Physical Society (APS)*, Savannah, Georgia, USA, November 16-20, 2015.

4. **Zeki Okan Ilhan**, Justin Barton, William Wehner, Eugenio Schuster, David Gates, Stefan Gerhardt, Egemen Kolemen and Jonathan Menard, "First-Principles-Driven Model-Based Optimal Control of the Current Profile in NSTX-U", *56th Division of Plasma Physics (DPP) Annual Meeting of the American Physical Society (APS)*, New Orleans, Lousiana, USA, October 27-31, 2014.

5. **Zeki Okan Ilhan**, Justin Barton, Wenyu Shi, Eugenio Schuster, David Gates, Stefan Gerhardt, Egemen Kolemen and Jonathan Menard, "Physics-based Control-oriented Modeling of the Current Profile Evolution in NSTX-Upgrade", *55th Division of Plasma Physics (DPP) Annual Meeting of the American Physical Society (APS)*, Denver, Colorado, USA, November 11-15, 2013.

6. **Zeki Okan Ilhan**, David Huxley-Cohen, Jason Barry, Eugenio Schuster, Mark Gilmore and Andrew Ware, "Optimal Closed-Loop Control of the Azimuthal Ve-

locity Profile in HELCAT by ExB Actuation", *54th Division of Plasma Physics (DPP) Annual Meeting of the American Physical Society (APS)*, Providence, Rhode Island, USA, October 29 - November 2, 2012.

7. **Zeki Okan Ilhan**, Eugenio Schuster, Shuangwei Xie, Mark Gilmore and Andrew Ware, "Optimal Azimuthal Velocity Profile Control by ExB Actuation in HELCAT", *53rd Division of Plasma Physics (DPP) Annual Meeting of the American Physical Society (APS)*, Salt Lake City, Utah, USA, November 14-18, 2011.